Aspects of the DELPHI Vertex Detector and future silicon trackers at LHC

Richard Brenner

SEFT
Research Institute for High Energy Physics
University of Helsinki
Helsinki, Finland

Academic dissertation

To be presented, with the permission of the Faculty of Science of the University of Helsinki, for public criticism in the Main Auditorium of the Department of Physics (Siltavuorenpenger 20D) on December 20, 1996, at 10 o´clock in the morning.

Helsinki 1996

Contents

Foreword

This thesis is based on the work carried out, as a member of the DELPHI collaboration, working on the Vertex Detector and in the RD20 group developing sensors and electronics for LHC. During five years I have been working for Åbo Akademi, the University of Helsinki, and as a Fellow, at CERN. During this time there has been rapid development of particle physics and its instrumentation. The top-quark was discovered at Fermilab with the mass in good agreement with the precision measurements carried out at LEP. The development of instrumentation has facilitated the fulfilment of tight requirements associated with tracking.

The collaboration in which I have been working is large and future collaborations will grow even larger. The work in a collaboration is, in the end, performed by subgroups consisting of a few persons working closely together. The final output from the experiment is a combination of the contributions of these subgroups. It is a challenge to follow the general development of the experiment and at the same time give input to one's own part of the project. Thus the multipurpose nature of the experiment should be reflected in the individual staff capabilities. One participates in central activities such as shifts and team work which not only connect to one's specialty but to the whole experiment.

The most pleasant part of working in a collaboration is the contact with the persons with whom you work closely together. Valuable information is shared at numerous coffee breaks where mini colloquia are presented with graphs drawn on serviettes. I want to mention a few persons who have especially influenced my work; Doc Risto Orava who always has supported me in the work and encouraged me to continue, and Peter Weilhammer, my group leader in the SSD group at CERN, always pushing for new limits and giving the chance to test new concepts. I want especially to thank the persons from the DELPHI VD group, Vincent Chaubaud, Hans Dijkstra, Yves Dufour, Magnus Karlson and Mike Tyndel for the fruitful work together and everyone for being patient with me. Finally, I want to thank Camilla and Shaun Roe for the help they gave me by reading through and giving comments to this thesis.

Introduction

The first part of this thesis will give an overview of the environment of an experimental physicist in a big collaboration. The first chapter describes the environment of LEP and the DELPHI apparatus, followed by an overview of physics models for leptons and hadrons in the second chapter. The third chapter describes the mechanism of b-quarks from their production by a Z^0 boson to the detection of the decay.

The next section explains the design consideration for silicon vertex detectors. These aspects are valid for any non-continuous tracker. Sensors and electronics are the parts which have undergone the fastest development in recent years. Chapter 5 discusses the status of the development of the DELPHI vertex detector. The last chapter summarises the challenge for silicon trackers at the future LHC machine.

The publications included in the thesis are:

1. I. Hietanen et al., Ion-implanted detectors processed on a 100 mm wafer, Nucl. Instr. and Meth. A301 (1991) 116-120.

2. R. Brenner et al., Double-Sided capacitively coupled silicon strip detectors on a 100 mm wafer, Nucl. Instr. and Meth. A315 (1992) 502-506.

3. R. Brenner et al., Measurement of the spatial resolution of double-sided double-metal AC-coupled silicon microstrips detectors, Nucl. Instr. and Meth. A326 (1993) 189-197.

4. N. Bingefors et al., The DELPHI Microvertex detector, Nucl. Instr. and Meth. A328 (1993) 447-471.

5. R. Brenner et al., Design and performance of an analog delay and buffer chip for use with silicon strip detectors at LHC, Nucl. Instr. and Meth. A339 (1994) 564-569.

6. R. Brenner et al., Performance of a LHC front-end running at 67 MHz, Nucl. Instr. and Meth. A339 (1994) 477-484.

Publication 1 describes the work done on developing single-sided directly coupled silicon sensors of a typical DELPHI VD design. The sensors were parametrised by static measurements of C-V characteristics, interstrip capacitance and leakage current. The dynamic performance of the sensors was tested with a ^{90}Sr source.

Publication 2 covers the development of double-sided double-metal silicon sensors. In addition to the static measurements done in publication 1 the characteristics of the separation on the n-side were investigated. The dynamic measurements were done by laser spot and ^{90}Sr source.

In publication 3 two designs of double-sided double-metal silicon strip sensors were tested in a testbeam. The main difference between the designs was the insulator between the two metal layers. Results on the spatial resolution for both the p-side and the n-side were obtained.

Publication 4 describes the performance of the DELPHI VD after the first upgrade. The paper is detailed in describing the work involved in an upgrade and the performance in terms of stability and resolution which has been achieved.

Publications 5 and 6 cover the work done for developing front-end electronics for a future LHC silicon tracker. The publications are done in parallel. The first describes measurements of the analogue pipeline and buffer which is one of the most important parts in the design. The second describes a full test, both in the laboratory and in a testbeam, of a full front-end electronics chain consisting of three separate prototype circuits chained together.

Abbreviations

ALEPH	= Apparatus for LEP Physics
ATLAS	= A Toroidal LHC Apparatus
BSP	= Boosted Sphericity Product
CERN	= Conseil Européenne pour la Recherche Nucléaire
CMOS	= Complementary MOS
CMS	= Compact Muon Solenoid
DAS	= Data Acquisition System
DELPHI	= Detector with Lepton, Photon and Hadron Identification
GUT	= Grand Unification Theory
L3	= The third experiment at LEP
LEP	= Large Electron Positron Collider
LHC	= Large Hadron Collider
MOS	= Metal Oxide Semiconductor
MSM	= Minimal representation of the Standard Model
OPAL	= Omni Purpose Apparatus for LEP
QCD	= Quantum Chromodynamics
QED	= Quantum Electrodynamics
RD20	= The 20^{th} Research and Development project for LHC
SCT	= Semiconductor Tracker
SM	= Standard Model
SPS	= Super Proton Synchrotron
SSD	= Solid State Development group
SUSY	= Super Symmetry
VD	= Vertex Detector

1. CERN and the LEP Collider

The European Organisation for Nuclear Research (CERN), one of the leading research centres for high energy physics in the world, was founded in 1954. The laboratory has gone through several development steps from the first synchro-cyclotron to the invention of the Nobel prize winning proton-antiproton collider SPS. The latest upgrade, the LEP collider (figure 1.1), which is the biggest accelerator-storage ring in the world, was finished in 1988. The machine with a circumference of 27 km was added to the old CERN accelerator park and some of the already existing accelerators are used as injectors to the new machine. The beamline is situated about 100 m below ground in a tunnel crossing the Franco-Swiss border several times. All four interaction regions, equipped with the experiments ALEPH, DELPHI, L3 and OPAL, are however built in French territory. The LEP collider operates at an energy around the Z^0 peak, $\sqrt{s}$ = 91 GeV/c, with a total luminosity of 1-2 × 10^{31} $cm^{-2}s^{-1}$[1] providing around 2 pb^{-1} per week and per experiment. The first physics run with the LEP collider was performed in autumn 1989.

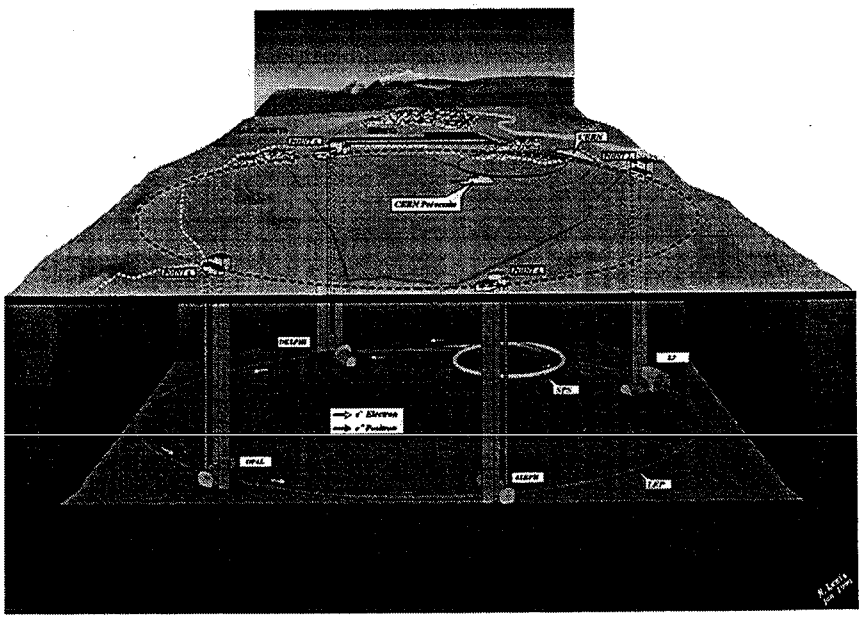

Figure 1.1. A cross-section of the LEP accelerator showing the surface installations and the underground areas.

The major physics parameters measured at LEP are the mass, m_Z, and the width, Γ_Z, *of the* Z^0 boson resonance and the electroweak parameters of the standard model. At present the statistical error of the measurements of m_Z and Γ_Z combining the measurements from the four experiments and the error of the LEP beam energy calibration are of the same size. With more statistics the accuracy of the m_Z and the Γ_Z measurements improves and the error will mainly depend on the beam energy calibration. The error of the beam energy calibration can be halved if sufficient transverse polarisation of the beam is obtained during physics data taking conditions. Studies done at machine development runs have shown that a transverse polarisation of 10% to 20% is obtainable with resonant depolarisation[2] which is sufficient for improving the present energy calibration .

The LEP collider with parameters given in table 1, was designed for an absolute upper energy limit of around 100 GeV/beam determined both by the maximum field in the bending dipole magnets and by the power that can be supplied to CERN for the accelerating cavities. An energy upgrade will take place in 1996 to 1998 increasing the energy in the machine first to the W^-W^+ threshold of $\sqrt{s}$ = 164 GeV/c and later to 192 GeV.

At the end of this century a proton-proton collider will be installed in the same tunnel as the LEP collider. The plan to build a Large Hadron Collider[3] (LHC) was already considered when designing the LEP collider by leaving enough space above the LEP machine in the tunnel. The plan was however not practical and instead the LEP machine will be replaced by the LHC. Protons will be collided in the LHC at a centre-of-mass energy of $\sqrt{s}$ = 14 Tea with a luminosity of 1.7×10^{34} $cm^{-2}s^{-1}$. The LHC machine can also be used for heavy ion collisions producing extremely high energy densities of 4 to 8 GeV/fm^3. The centre-of-mass energy per nucleon will be about 6.3 Tea and the foreseen luminosity 1.8×10^{27} $cm^{-2}s^{-1}$. There have also been plans to operate the LHC- and LEP-colliders at the same time colliding electrons and protons, which will require the LEP machine to be reassembled above the LHC in the tunnel but low priority is put to this scheme.

Maximum energy	55 GeV (96 GeV)
Maximum luminosity	11×10^{30} $cm^{-2}s^{-1}$
Time between collisions	22 μs
Average fill lifetime	12 h
Beam size at interaction points	$\sigma_y \approx 10$ μm, $\sigma_x \approx 150$ μm
RF cavity units in the ring	140 modules
Dipoles in the ring	1104 modules
Quadrupoles in the ring	864 modules
Power consumption, approx.[4]	200 MW

Table 1 Parameters of the LEP machine in original configuration. The parameters for the upgraded machine is in closes.

1.1 The DELPHI experiment

The **DE**tector with **L**epton **P**hoton and **H**adron **I**dentification[5][6] (DELPHI), shown in figure 1.2, is a multipurpose detector consisting of several subdetectors. DELPHI is divided into a barrel part and two end-caps. It is almost hermetic over the full space angle. The regions not fully covered are the cracks between the endcaps and the barrel which are filled with cables, and a very small solid angle around the beampipe. The 'blind' regions in the cracks have been equipped with triggers tagging events with tracks in the nonsensitive regions. The division of subdetectors is similar both in the end-caps and the barrel. The basic elements in DELPHI are the luminosity monitors, the trackers, the particle identification detectors and the calorimeters.

1.1.1 Luminosity monitors

The luminosity monitoring is done by two devices measuring the bhabha scattered electrons. The main luminosity measurement is done by the Small Angle Tagger (SAT). In addition, in the very forward region there is the Very Small Angle Tagger (VSAT) giving a fast monitor of the luminosity and the beam conditions.

The SAT consists of a tracker part which is in front of a calorimeter. The polar coverage is from 43 mrad to 135 mrad. The tracker is built of silicon strip sensors. The calorimeter is a laminate of lead sheets and scintillating fibres aligned along the beam-axis. The estimated error on the luminosity determination is

around 0.35%. With the help of the SAT tracker the knowledge of the acceptance of the SAT calorimeter can be improved reducing the error of the luminosity measurement locally to 0.05%[7]. In 1994 the SAT was replaced by the Small angle TIle Calorimeter (STIC) improving the error on the luminosity measurement to better than 2‰[8].

The VSAT is constructed of alternating tungsten plates and silicon sensors in a stack. The device is down- and up-stream from DELPHI covering polar angles between 5 and 7 mrad around the beam-axis. Some of the planes in the device are position sensitive which helps to eliminate particle showers at the edge of the detector.

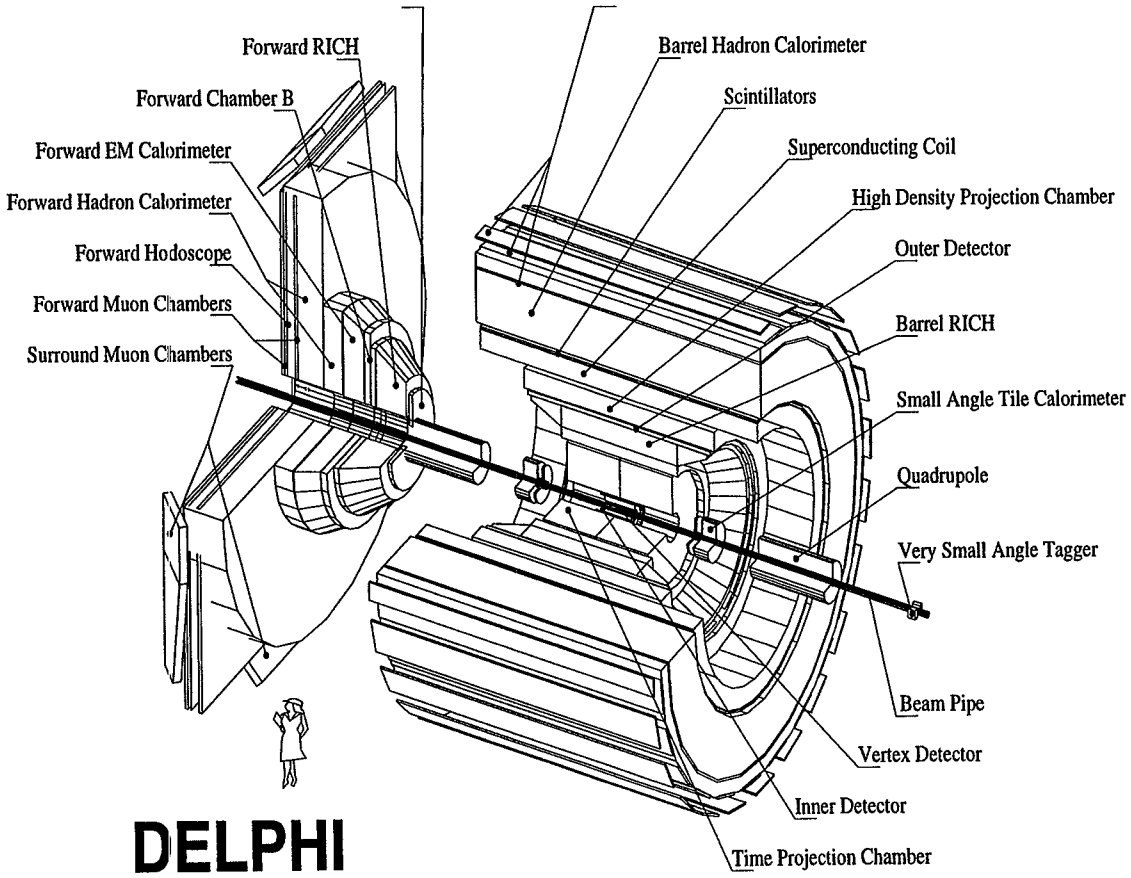

Figure 1.2. An exploded view of the DELPHI experiment.

1.1.2 Trackers

The tracking in DELPHI is done by many subdetectors. In the barrel section the Time Projection Chamber (TPC), the Inner Detector (ID), the Outer Detector (OD) and the Vertex Detector (VD) are give high precision track points. The tracking is embedded inside a superconducting solenoid with a 1.2 T homogenous magnetic field which is important for the momentum measurements. In the end-caps the Forward Chamber A (FCA) and the Forward Chamber B (FCB) are supplying the tracking information. Some other subdetectors in DELPHI such as the hadron calorimeters and the electromagnetic calorimeters are also position sensing which is one of the strengths of DELPHI.

The main tracking device is the TPC[9] giving three dimensional imaging essential for the pattern recognition. The detector is relatively small because of the limited space inside DELPHI, but longitudinally it partly overlaps with the end-cap tracking. The detector provides track points from 192 sense wires and 16 pads. The TPC gives optimal track reconstruction with all the wires included, between the polar angles 39° to 141°, and track information with degraded resolution between 21° and 159°. The reported position resolution is $\sigma_{R\phi}$=180-280 μm, depending on ϕ, and σ_{Rz}<0.9 mm.

The ID consists of a drift chamber giving 24 ϕ- points per track and five layers of Multi Wire Proportional Chambers (MWPC) giving *Rz*-points as well as fast trigger information. The ID covers polar angles from 17° to 163° which gives a good overlap with the tracking in the end-caps. The intrinsic resolution is $\sigma_{R\phi}$=90 μm and σ_{Rz}=600 μm. The material thickness for θ=90° given in units of radiation length is 3.75%.

The OD is the tracking detector furthest away from the interaction point (*R*≈2 m) giving a good measurement of high momentum tracks passing through the particle identifying Cherenkov radiation detector. A particle traversing the OD is measured by 5 drift tubes providing a fast trigger and *Rφ*- and *Rz*-information is given between the polar angles 40° and 140°. The position resolution of the detector is $\sigma_{R\phi}$=110 μm and σ_{Rz}=4.4 cm.

The VD consists of three concentric layers of silicon microstrip sensors mounted close to the beampipe. The VD covers a polar angle between 45° and 135° degrees giving three hits/track with a point resolution in the *Rφ*-direction around 7 μm. The detector was upgraded in 1994 with two layers of double-sided silicon sensors which will give the *Rz*-coordinate with a resolution between 10 and 20 μm depending on the track angle. The material thickness for θ=90° given in

radiation length is around 1.5%.

The FCA and FCB provide tracking and triggers for polar angles of $11°<\theta<33°$ and $147°<\theta<169°$. The FCA consists of three wire chambers providing 2×3 coordinates which give a space resolution of σ=300 μm per plane. The FCB has in total 12 planes providing 4×3 coordinates. The position resolution obtained with the combined planes is, for both x and y, σ=120 μm.

Combining information from the tracking detectors in DELPHI is a complicated task. A big effort has been put into aligning the devices. The obtained momentum resolution for 45.6 Gev/c muon pairs in the barrel region is $dp/p = 7\%$. The corresponding value in the end-caps is $dp/p = 17\%$ which includes information from the overlaps of the ID and the TPC in the barrel. For low momentum tracks the resolution is naturally worse because of the multiple scattering. The measured error for the μμ miss distance, defined as the distance between the extrapolated tracks at vertex for the two myons created in a Z^0 decay, measured by the OD and the VD is about 30 μm indicating a impact parameter resolution of 21 μm[10].

1.1.3 Detectors for particle identification

The particle identification is one specialty of the DELPHI experiment. In the barrel part both the TPC and the Barrel Ring Image CHerenkov (BRICH) detector are supplying *dE/dx* information. In the forward regions the information is supplied by the Forward Ring Image CHerenkov (FRICH) detector[11]. The muons are identified by the Muon Barrel (MUB) and the MUon Forward (MUF) chambers which are tagging minimum ionizing muons not absorbed in the iron of the Hadron Calorimeter.

The TPC, despite the small size, gives some *dE/dx* information which improves the e-π separation below 8 GeV in particular. The resolution of the *dE/dx* measurement for minimum ionizing π and e is 6.2% and 5.7% respectively[9]. The information is collected from the wires using the mean signal of the lowest 80% of the amplitudes associated with a track.

The MUB has two layers, one inserted in the return yoke of the magnet and one mounted outside the yoke. Each layer is composed of overlapping planks consisting of two staggered planes of drift chambers operating in proportional mode. The muon detection efficiency of one drift chamber is about 95%. Each track gives four hits which results in an excellent total efficiency of the detector.

The MUF is built with the same technology as the MUB but implemented in the end-caps. The efficiency, which has been measured by using the muon halo around the LEP beam, gives a total muon detection efficiency of the detector of 89%. The value includes around 8% inefficiency coming from structural dead space in the design.

The RICH detectors in the barrel and the end-caps follow the same concept. Different geometries and requirements make them nevertheless completely different. A particle entering the RICH first traverses a 1 cm thick liquid radiator and later 40 cm of gas radiator (FRICH). The gas radiator path in the FRICH is slightly longer than in the BRICH. The Cherenkov photons emitted in the liquid are passing through a UV transparent quartz window and are directly collected by counters filled with photon to electron converting vapour. The photons emitted in the gas are focused and reflected back on the counters by parabolic mirrors. The concept of using two different media in the Cherenkov radiation detectors is preferred due to better tagging of low momentum particles with the liquid and high momentum particles with the gas. A 4.2 σ separation has been achieved in the barrel part for π/K up to 18 GeV/c and p/K up to 33 GeV/c. In the forward part the corresponding values are 30 GeV/c and 50 GeV/c, respectively[12][13].

1.1.4 Calorimeters

In addition to calorimetry done by the luminosity monitors DELPHI is equipped with electromagnetic calorimeters and hadron calorimeters. The High density Projection Chamber (HPC) and the Forward Electro Magnetic Calorimeter (FEMC) perform the electromagnetic calorimetry and the Hadron CALorimeter (HCAL), both in the barrel and the end-caps, performs the hadron calorimetry.

The HPC is able to reconstruct three-dimensional charge distributions induced by electromagnetic showers. The detector uses the time projection principle. Lead is used as a converter and at the same time it forms the wall of the chamber. The charges created by the shower are read-out by a proportional wire plane at the end of each module. The HPC covers polar angles between 43° and 137° in the barrel. For fast triggering a layer of scintillator is placed inside the detector. The energy resolution is $(23/E^{1/2} + 1.1)$ % and the angular resolution is $(36/E^{1/2} + 2.5)$ mrad in ϕ and $(97/E^{1/2} + 10)$ mrad in θ [6].

The FEMC consists of 9064 lead-glass bricks in total mounted in one disk in each end-cap. The bricks are pyramid shaped pointing towards the interaction point. The polar angle coverage is from 10° to 36.5° and from 143.5° to 170°. The lead-glass is read by vacuum phototriodes. The energy resolution is $\delta_E/E=[(0.35+5/E^{1/2})^2 + (6/E)^2]^{1/2}\%$ where E is given in GeV [6].

The HCAL is a sandwich of 5 cm thick iron plates and 2 cm thick sampling gas detectors working in limited streamer mode. The barrel and the endcap parts consist of 19 and 12 layers, respectively. The iron plates in the HCAL are simultaneously the return yoke for the superconducting solenoid. The barrel and the end-caps of the HCAL have nearly a 6° overlap. The calorimeter is structured in towers consisting of 5 layers in the barrel part and 4 layers in the end-caps. The towers are pointing toward the interaction point. For triggering 4 × 4 towers are grouped into supertowers which are again in clusters of 4 arranged in hypertowers forming a spatial cone in depth. The energy resolution is $120/E^{1/2}\%$[6].

1.1.5 Triggers

The aim of the trigger is to filter signals from background. The final trigger rate for the data recorded is a few Hz during physics data-taking. The trigger system is staged in three levels. The two first levels are hardwired combinations of trigger signals from the subdetectors and the third level trigger is a pure software trigger with some event reconstruction. In the design phase the assumption was that the tree triggers would not reduce the data rate sufficiently. Therefore an additional fourth level trigger was developed with capability of fully reconstructing the event. This trigger was never needed.

In addition to the detectors mentioned previously there are some detectors in DELPHI specialized on triggering. The major for triggering specialized detectors are the Time-Of-Flight (TOF) and the forward hodoscope (HOF). In addition there are triggers put in regions not covered by the subdetectors in DELPHI in order to avoid efficiency losses. The specialized trigger detectors are typically scintillators giving fast trigger signals.

The first and second level triggers which are the fast triggers are running synchronously with the beam cross over (BCO) occurring every 22 μs. The third level trigger is running asyncronously with the BCO. The first level trigger decision delay is 3 μs and the second level trigger delay is 40 μs. The typical time

it takes for the third level trigger to decide is 30 ms. The trigger is split into components such as "track", "muon", "electromagnetic energy", "hadron energy", "bhabha" and "cosmic". At present 16 decision functions exist combining the triggers from the subdetectors. Almost all the subdetectors are contributing to the fast trigger.

1.1.6 Data acquisition system

The front-end Data Acquisition System (DAS) in the DELPHI experiment is implemented in the FASTBUS standard. The DAS is built in a tree-like structure with the central DAS on the top and the subdetector front-end as branches. The DAS can be split into 6 levels; the front-end, the board processing, the crates, the partitions, the central partition and the data logging[14].

The front-end units are running synchronously with the BCO converting the analogue data to digital information. The data is stored in a buffer running synchronously with the BCO. The board processing is an asyncronus buffer with a depth of one to four events. The operations within the FASTBUS crate and the connection to the rest of the experiment are done with the Fastbus Intersegment Processor (FIP) unit. Each FIP forms a partition in the DAS. Most of the sub-detectors have only one FIP unit, but there are detectors like the HPC that have several units. The readout of an event is done on command of the level 2 trigger. The data is transferred from the crate to the cluster by software called Local Event Supervisor (LES). LES is resident in the FIP and ensures that the data are transported both to a Multi Event Buffer (MEB) and a Spy Event Buffer (SEB). The Global Event Supervisor (GES) moves the data from the MEB to the Global Event Buffer (GEB). The data in the SEB are used for on-line monitoring and for the third level trigger processor. The data logging is done from the GEB if the event has been tagged by the trigger. One more level in the DAS which includes the fourth level trigger has not been implemented. This level would be situated between the GEB and the logger emulating and classifying interesting events. A schematic picture of the DAS is shown in figure 1.3.

The logged data are processed instantly giving an immediate feedback on the quality of the data and the performance of the sub-detectors. The DELPHI experiment is operated by four persons during physics data-taking. The work is split between operating the DAS, Slow Control, controlling the data quality and off line processing of raw data. The average efficiency of the DAS is over 80%

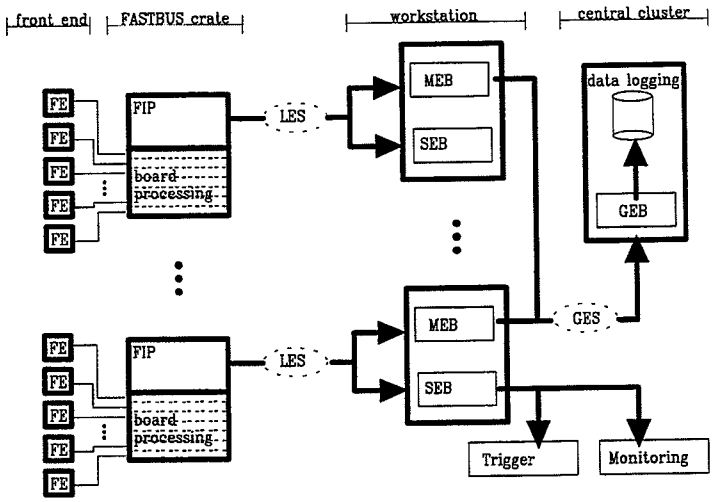

Figure 1.3. A schematic diagram of the data path in DELPHI

which includes the dead time at the start of the fills when high voltages are ramped-up on subdetectors, and the trigger dead time during data taking which is around 5%. The average event size for a Z^0-event is around 120 kbytes.

2. The Standard Model

In the Standard Model the pure leptonic theory of the electro-weak interactions is extended to the theory for hadrons and the strong interactions. The Standard Model can be represented by three unitary symmetry groups of colour, isospin and hypercharge

$$SU(3)_C \otimes SU(2)_L \otimes U(1)_Y.$$

The minimal representation of the Standard Model (SM) has 18 free parameters which have to be experimentally verified;

- 6 quark masses ($m_u, m_d, m_c, m_s, m_t, m_b$)
- 3 lepton masses (m_e, m_μ, m_τ)
- the Higgs mass (m_H)
- 3 gauge couplings (G_F, α, α_s)
- the weak mixing angle ($sin^2\theta_W$)
- 4 parameters describing the CKM matrix ($\theta_1, \theta_2, \theta_3, \delta$).

The Standard Model has been successful in predicting the existence of the gauge bosons Z^0, W^- and W^+, but the discovery of the Higgs particle is yet to be made. Even if the Standard Model and the experimental data agree the model has drawbacks. Features like the family structure, the amount of free parameters, the inability to predict fermion masses, the lack of evidence for the Higgs and the fact that extrapolation of gauge coupling constants show that no unification can happen in the framework of the SM leave space for theories that extend the SM.

The most promising theories presently are based on supersymmetry (SUSY)[15] and the Grand Unification Theories (GUT)[16]. In SUSY models all known bosons get new fermion partners and all known fermions get new boson partners. In the simplest version of the theory every particle has one SUSY partner, a sparticle. As an example, the quark in the SM with spin 1/2 gets a SUSY partner called squark with spin 1. The quantum variable R is introduced with R = +1 for the standard particles and R = -1 for sparticles. The R-symmetry allows a particle to be transformed to its sparticle partner and vice versa. Because of the R-symmetry at least the lightest sparticle must be stable. No sparticles have

been observed so far.

The GUT models are based on a suggestion that there might be a Grand Unified gauge theory beyond the SM. Even if the strength of the three interactions in the SM are very different at low energies the coupling constants at high energies may approach each other at around 10^{15} GeV. The SM would emerge from a single coupling constant after symmetry breaking of the Grand Unification. The simplest grand unification symmetry that incorporates the SM is the SU(5)[17], but there are several other models as well. The GUT has been tested by extrapolating the measurements of the running coupling constants at low energies to the GUT scale[18]. The exercise shows that by a simple extension of the SM to SU(5) the coupling constants do not meet. The unification can still be achieved if new physics is introduced such as SUSY[19].

2.1 Strong interactions

The theory of quantum chromodynamics, QCD[20] [21], describes the strong colour interactions between the quarks and gluons. The existence of three quark fermion constituents in a baryon and a quark-antiquark pair in the mesons was postulated by Gell-Mann [22] in early 1960's. The quarks, appear in three coloured doublets, have quantum numbers called flavours. Constructing a baryon of three fermions clearly violates the Pauli principle and to overcome the problem the quantum variable colour was introduced. Each quark flavour can exist in three colours and the antiquark carries anti-colour. The quark-quark interactions are invariant and can be described by the unitary symmetry $SU(3)_C$ with each quark flavour forming a colour triplet. The field quanta, the gluons, mediating the "colour charge", form an octet representation of $SU(3)_C$. Neither quarks nor gluons can exist as free particles which is incorporated in the theory as a "confinement". All hadrons are colourless.

In contrary to the abelian electromagnetic interaction the non-abelian feature of the QCD theory allows self-interaction between gluons. The strong coupling constant changes in strength depending on the scale or energy at which it is measured. The value can be approximated to the leading order by

$$\alpha_s(\mu^2) = \frac{1}{b_0 \ln(\frac{\mu^2}{\Lambda^2})}$$

$$b_0 = \frac{33-2n_f}{12\pi} \quad ,$$

where n_f is the number of flavours, μ the mass scale and Λ the experimentally measured QCD scale parameter. At LEP energies the measured $\alpha_s(M_Z^2) \equiv 0.128$[23]. The magnitude of the lifetime for a particle decaying through strong interaction is at the order of 10^{-23} s.

2.2 Electroweak interactions

The unification of the electromagnetic interactions (QED) and the weak interactions is represented in the model of the electroweak interactions formulated by Glashow-Salam-Weinberg[24]. The electroweak interactions are described by the unitary symmetry group $SU(2)_L$ for "weak isospin" and $U(1)_Y$ for "weak hypercharge". Initially no masses exist but they are generated when the $SU(2)_L \otimes U(1)_Y$ symmetry is spontaneously broken by the Higgs mechanism[25] to the $U(1)_Q$ of QED.

A feature of the weak theory is that only left-handed fermions with weak isospin I=1/2 interact and not right-handed fermions with I=0, therefore the notation L in the $SU(2)_L$. The relation between charge and isospin-hypercharge is given by

$$Q = I_3 + \frac{Y}{2} \quad ,$$

where I_3 is the third component of the weak isospin quantum number and Y is the hypercharge quantum number.

The fields for the observable particles mediating the electroweak force are transformations of the isovector triplet fields $\mathbf{W}^n_\mu$ of $SU(2)_L$ and of the isovector

singlet field $\mathbf{B}_\mu$ of $U(1)_Y$,

$$W_\mu^\pm = \frac{1}{\sqrt{2}}(W_\mu^1 \pm iW_\mu^2)$$

$$Z_\mu = \cos\theta_W W_\mu^3 + \sin\theta_W B_\mu$$

$$A_\mu = \sin\theta_W W_\mu^3 + \cos\theta_W B_\mu \ ,$$

where θ_W is the weak mixing angle (Weinberg angle).

All the initially massless bosons W^-, Z^0 and W^+ have, because of the spontaneous symmetry breaking Higgs mechanism, acquired mass. The photon A, however, stays massless. The charged current interaction, mediated by W^+ and W^- bosons, is parity-violating and interacts only with left-handed fermions. The neutral current, mediated by the photon A and Z^0 boson, on the other hand, is parity-conserving and interacts both with left- and right-handed fermions. The $SU(2)\otimes U(1)$ family structure for the leptons can be written

$$\begin{pmatrix} \nu_e \\ e \end{pmatrix}_L , \begin{pmatrix} \nu_\mu \\ \mu \end{pmatrix}_L , \begin{pmatrix} \nu_\tau \\ \tau \end{pmatrix}_L , e_R , \mu_R , \tau_R .$$

The quarks are grouped similarly in left-handed doublets and right-handed singlets. The quark family structure, however, differs from the lepton family structure because the down-type quark states are "rotated" by a mixing angle. The up-type quark states are left unmixed by convention. The quark mixing is factorised in the Cabibbo-Kobayashi-Maskawa[26][27] (CKM) mixing matrix which relates the weak eigenstates to the mass eigenstates:

$$\begin{pmatrix} d' \\ s' \\ b' \end{pmatrix} = \begin{pmatrix} V_{ud} & V_{us} & V_{ub} \\ V_{cd} & V_{cs} & V_{cb} \\ V_{td} & V_{ts} & V_{tb} \end{pmatrix} \begin{pmatrix} d \\ s \\ b \end{pmatrix} .$$

The matrix **V** is parametrised[27] reducing it to three angles θ_i and one phase δ. The phase can acquire a value between 0 and 2π, but any value different from 0 means breaking of the CP-invariance for the weak interactions.

The weak mixing angle relates the electromagnetic coupling known as e to the weak coupling g_w, given by $g_w sin\theta_W = e$. The running electroweak coupling constants usually defined as $\alpha_1(\mu^2)$ and $\alpha_2(\mu^2)$ are

$$\alpha_1(\mu^2) = \frac{5\alpha(\mu^2)}{3\cos^2\theta_W}$$

$$\alpha_2(\mu^2) = \frac{\alpha(\mu^2)}{\sin^2\theta_W} \quad ,$$

where $\alpha(\mu^2)$ is the running fine structure constant and θ_W is the weak mixing angle. At values measured at LEP experiments are $\alpha(M_Z^2)^{-1} = 127.9$ and $sin^2\theta_W = 0.23$. The typical lifetime for a weak decay is of the order of 10^{-8} s.

2.3 The Higgs mechanism

The problem with a simple electroweak theory is that the fermions and bosons are massless. The masses cannot be simply generated by adding a mass term to the wave function, since the theory would not stay renormalisable. Therefore the masses are generated via the Higgs mechanism based on spontaneous symmetry breaking. In the simplest way this is introduced into the electro-weak theory with a doublet of complex scalar fields which is invariant under SU(2) gauge transformations,

$$\phi = \begin{pmatrix} \phi^+ \\ \phi^0 \end{pmatrix}.$$

When the doublet field is expanded around the ground state in order to achieve a spontaneous symmetry breaking a single physical scalar Higgs field is generated. The Higgs field couples to fermions and bosons with a strength proportional to their masses.

Although the fermions and bosons are essential for the Standard Model the Higgs mechanism gives no prediction for their masses. Experimental measurements remains the only way to estimate the masses. Moreover the Higgs mechanism is the base for the Standard Model, but the existence of a Higgs scalar has not yet been verified.

3. Heavy Flavours

There are several reasons to study heavy flavoured quarks, especially bottom, at LEP. The large branching ratio and the possibility to tag b-quarks with a high efficiency and purity open the chance to probe the Standard Model with a good sensitivity. In the search for the Higgs particle the b-tagging plays an important role since the Higgs will predominantly decay into b-quarks. The Standard Model predicts to the first order that a universality exists for the branching ratio of the Z^0 into up-type and down-type quarks. The branching ratio of the Z^0 into down (d), strange (s) and bottom (b) quarks is around 15% and into up (u), charm (c) and top (t) quarks around 12%. Because of the electroweak mixing between quarks the branching ratios of the Z^0 into quarks are different. Precise studies of the electroweak properties in the Z^0 decay are one way of probing the Standard Model at LEP energies. The coupling of b-quarks to t-quarks is stronger than for other quark flavours and therefore the properties of the t-quark is influence the electroweak parameters of especially the b-quarks, even if the t-quark threshold is far above the energies available at LEP. Precision studies are helped by the relatively long lifetime of the b quark and the very clean background conditions in the e^+e^--collider. The tagging of b-quarks is easier than before because of high precision vertex detectors installed in the experiments.

3.1 Annihilation of e^+e^- into b-jets

The creation of quarks in an e^+e^- collision and consecutive hadronic decay is a four step process.

- Annihilation of e^+e^- pairs into a virtual Z^0 or a γ which decays into primary $q\bar{q}$ -quarks. Real γ can be radiated from the initial e^+e^--state or the final $q\bar{q}$ -state.
- Gluon radiation off the primary quarks producing more partons.
- Fragmentation of the coloured partons into stable and unstable colourless hadrons.
- Decay of the unstable hadrons into particles that can be observed.

The process is schematically drawn in figure 3.1.

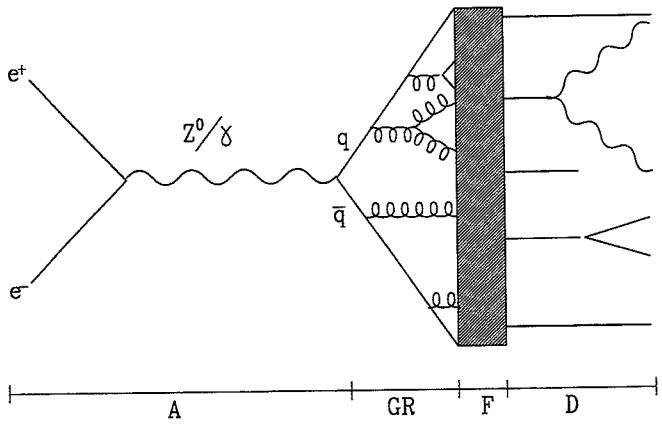

Figure 3.1. The decay of Z^0 to observable particles where A=annihilation, GR=gluon radiation, F=fragmentation and D=decay.

3.1.1 Production of b-quarks

The coupling of the Z^0-boson to quarks through the vector and the vector-axial charge is defined in the electroweak theory. The partial width of the Z^0 into quarks is described by the Born approximation,

$$\Gamma_B(Z \rightarrow b\bar{b}) = \frac{G_F m_Z^3}{8\sqrt{2}\pi}\beta\left[\frac{3-\beta^2}{2}v_b^2 + \beta^2 a_b^2\right],$$

where

$$\begin{cases} v_q = 2I_q^{3L} - 4e_q \sin^2\theta_W \\ a_q = 2I_q^{3L} \end{cases}$$

and $2I_q^{3L} = +1$ for up and -1 for down quarks.

Without any further corrections the difference in width for different types

of quarks is only mass dependent which enters through the velocity β, given by $\beta = \sqrt{1-\mu_b^2}$, where $\mu_b^2 = \frac{4m_b^2}{s}$. In this approximation of the first order the radiative corrections from the α are included through the electroweak mixing angle $\sin^2\theta_W$ and the Fermi constant G_F for a mass of the top quark less than 100 GeV.

The partial width incorporating all electroweak, QED and QCD corrections can be written as

$$\Gamma(Z^0 \to b\bar{b}) = \Gamma_B^V(G_F^{eff}, \sin^2\theta_W^{eff}) \left[1+\frac{3}{4}\frac{e_b^2\alpha}{\pi}\right]\left[1+c_1(\frac{\alpha_s}{\pi})+\ldots\right] +$$

$$\Gamma_B^A(G_F^{eff}, \sin^2\theta_W^{eff}) \left[1+\frac{3}{4}\frac{e_b^2\alpha}{\pi}\right]\left[1+d_1(\frac{\alpha_s}{\pi})+\ldots\right].$$

where the electroweak corrections are included in the first term as adjustments to the Fermi constant and electroweak mixing angle. The second term holds the QED corrections and the third term the QCD corrections.

The electroweak corrections are split into a flavour independent and a flavour dependent one. The corrections are strongly sensitive to the top mass but also to some extent sensitive to the mass of the Higgs boson. The flavour independent correction is caused by loop corrections to the electroweak propagators including γ-Z mixing shown in figure 3.2.

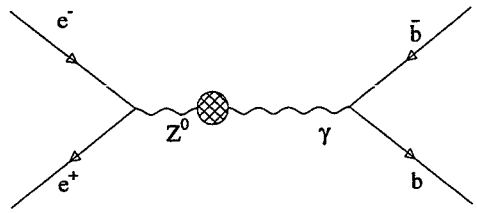

Figure 3.2. The Feynman diagram for Z^0-γ mixing in the flavour independent electroweak correction.

The flavour dependent corrections to the vertex shown in figure 3.3 are effective only for b-quark final states because of the t-quark coupling.

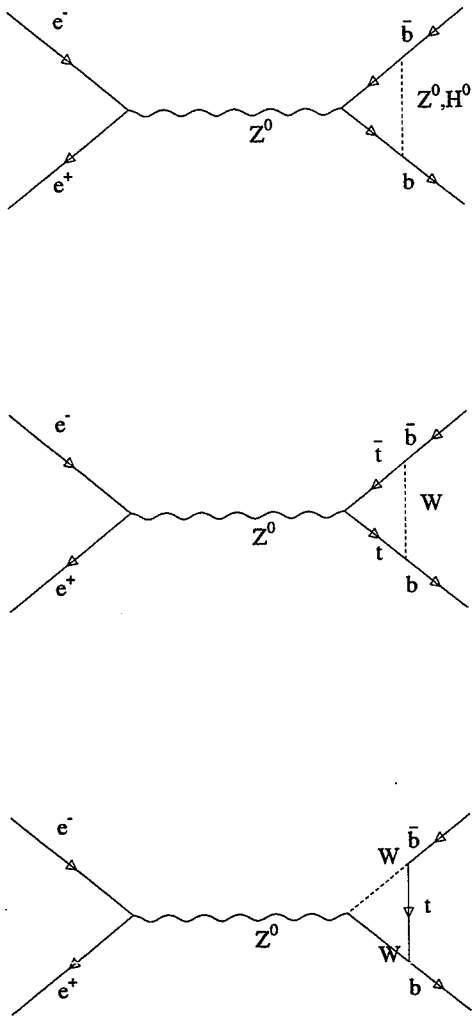

Figure 3.3. Feynman diagrams for flavour dependent electroweak corrections.

The correction enters the vector and vector-axial coupling with the same amount, $\frac{2}{3}\delta_t$, where

$$\delta_t = \frac{3\sqrt{2}\,G_F m_t^2}{(4\pi)^2}.$$

Both flavour and flavour independent electroweak corrections can be incorporated into the Born approximation by shifting the Fermi constant and the mixing angle. This results in an effective Fermi coupling constant of G_F^{eff} and an effective electroweak mixing angle of $\sin\theta_W^{eff}$, defined by

$$G_F^{eff} = G_F(1+\delta_t-\delta_b\frac{4}{3}\delta_t)$$
$$\sin\theta_W^{eff} = \sin^2\theta_W+\cos^2\theta_W\ \delta_t+\delta_b\frac{2}{3}\sin^2\theta_W\ \delta_t\ ,$$

where δ_b=1 for b-quarks and 0 otherwise.

The QED corrections do not depend on the top quark and generally the corrections are very small.

The QCD corrections to the partial width of the Z^0 decay are different for the vector and the axial-vector couplings. The difference is caused by breaking of the chiral invariance because of the masses and the large split in mass between the bottom and the top quark. The first order corrections in α_s have been calculated for non-zero quark masses[28][29], giving

$$c_1 = 1+3\mu_b^2+...$$
$$d_1 = 1+\mu_b^2\ \log(4/\mu_b^2)+...\ ,$$

where $\mu_b^2=4m_b^2/s$. The second order correction takes into account the difference between the b- and t-quark masses[30]. The coefficients in the second order QCD-correction are top mass dependent.

3.1.2 Hadronisation of heavy quarks

The processes which occur between the decay of a Z^0-boson and the final particles observed in a detector are described both by a perturbative process of gluon radiation and by a non-perturbative fragmentation processes.

The quarks radiating hard gluons is the mechanism for creating gluon jets. The process can be numerically calculated with the strong perturbation theory. For b-quarks produced in Z^0 decays about 20% of the initial energy is lost to gluon radiation. Measurements of b-meson spectrums at LEP show however that around 70% of the initial energy of the b-quark is on average transferred to the b-flavoured hadron[31].

The fragmentation process itself cannot be quantitatively computed by QCD, but the form of the fragmentation function has been parametrised by several models described in literature[32][33][34][35]. In the fragmentation process of heavy quarks the energy is mainly retained in the heavy quark and only a little energy is left over for creation of light quarks. Repetition of this process results in a jet of hadrons with limited transverse momentum.

In the Peterson fragmentation model the probability for a heavy quark Q to get fragmented into $Q\overline{q}$ + q is proportional to the inverse of the energy transfer given by the Peterson function

$$\Delta E = 1 - \frac{1}{z} - \frac{\varepsilon_q}{1-z} \quad ,$$

where z is the fraction of the momentum retained in the B meson and ε_q the square ratio of the light quark to the heavy quark mass. The average fraction of energy taken by the B meson is in the Peterson function $\langle z \rangle \approx 0.8$ for the square ratio of the light-to-charm quark and charm-to-bottom quark masses $\varepsilon_q \approx 0.1$.

3.1.3 Lifetimes of heavy hadrons

The lifetime of hadrons with a heavy quark constituent, Q, is to the first order dependent on the momentum transfer in weak decays which is of the order of m_Q. In the spectator model the lifetime of all weakly decaying states of a heavy quark is determined by the intrinsic lifetime of the heavy quark. The hadronic decay of a heavy hadron with a b-quark constitute is approximated in the spectator model by [36]

$$\frac{1}{\tau_B} = \frac{G_F^2 m_b^5}{198\,\pi^3} \left[3.92 \mid V_{cb} \mid^2 + 7.55 \mid V_{ub} \mid^2 \right] ,$$

where G_F is the Fermi coupling constant, m_b the mass of the b-quark and $|V_{qq}|$ are elements in the Cabibbo-Kobayashi-Maskawa mixing matrix. The spectator model gives a good approximation of the lifetime for hadrons with a massive b-quark constituent. For hadrons with a c-quark the model does not give good agreement with experiments. The model needs to be corrected for non-spectator effects to explain differences in lifetimes of heavy hadrons. The corrections to the lifetimes are mainly forced by quark interference in the final state and W-exchange. The interference between quarks in the final state due to the Pauli principle changes the lifetime from the spectator model value. If the constituent in the heavy hadron is a positively charged light valence quark or antiquark, the quark is annihilated after the W-exchange. This effect gives a shortening of the lifetime. The magnitude of the non-spectator model corrections is found to decrease with the heavy quark mass.

3.2 Detecting heavy flavours

Efficient tagging of hadrons containing b-quarks is essential for many of the precision measurements of the Standard Model. The hard fragmentation of the b-quark and the long lifetime of the produced hadrons are the main characteristics of a b-quark which makes it possible to separate it from other quark decays. A variable commonly used is the boosted sphericity product (BSP)[35] which relies on the different fragmentation of the b-quark compared with the light quarks. An independent method to enrich the b-sample is the impact parameter method or dipole method[37] which are both based on the long lifetimes of b-quark

flavoured hadrons. Since the two event variables are based on two completely different processes, QCD and electroweak interactions, they are uncorrelated. The event-variables are therefore frequently combined by multidimensional analysis[38] or by neural networks[39] giving a better tagging.

The boosted sphericity product method (BSP)[40] is used to improve the b-quark purity of the data sample by enriching the b-quarks in the sample with hopefully small loss of b-quarks. The BSP method is an event shape variable describing the sphericity of the event. The sphericity of the event is generated by boosting the beauty hadron to its rest frame as illustrated in figure 3.4. The boosting factor is given by $\gamma = \sqrt{s} \ / \ 2m_q$, where m_q is the mass of the b-quark and s is the center-of-mass energy in the collision.

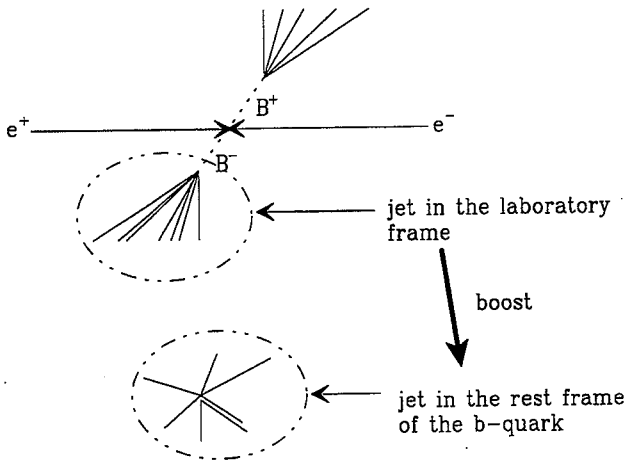

Figure 3.4. The event seen after being boosted from laboratory frame to the rest frame of the b-quark.

Calculating the sphericity of the jet by looking at only charged tracks or on both charged and neutral tracks will give a higher average sphericity for the b-quarks than for the other quarks. The sphericity is determined separately in each jet/hemisphere and the BSP is given by the product of the two sphericities.

There are several methods to detect the flight distance of the heavy hadron before decaying. In the impact parameter method the distance between the secondary vertex and the primary vertex is either separately reconstructed or given by the beamspot. The impact parameter is defined as the distance of the closest approach from the track to the primary vertex as shown in figure 3.5.

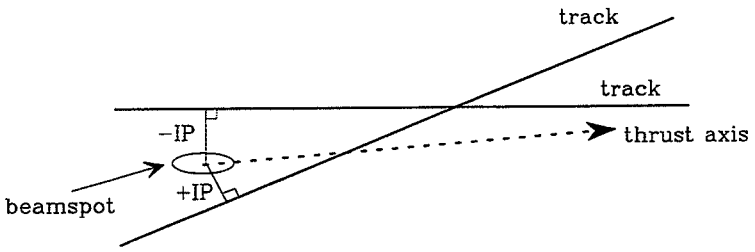

Figure 3.5. The impact parameter definition.

The lifetime sign can be chosen in several ways but commonly the crossing point of the thrust-axis of the jet behind the primary vertex will give a negative lifetime. The impact parameter is typically determined by the $r\phi$-projected tracks since this resolution is better and the beamspot is smaller in this projection. Reconstructing the primary vertex instead of using the beamspot constraint will degrade precision of the impact parameter but decrease the correlation between two jets/hemispheres. Several variations of the impact parameter method exist. In the dipole method the distance between the vertices is determined, which in fact gives the sum of the lifetimes. In this method the correlation is naturally big between the hemispheres.

4. Designing vertex detectors

The purpose of a vertex detector is to give precision track information close to the interaction point. If the measurement is good the secondary vertex of a decay of a heavy hadron can be resolved from the primary vertex. With a precise detector the momentum resolution can also be improved, especially for low momentum tracks.

In the LEP experiments the vertex detectors are small size assemblies with detector units made of silicon. The vertex detectors have barrel geometry with limited polar angle coverage. Because of very limited space between the beampipe and the gaseous tracking detectors at the start-up of the LEP only two experiments, ALEPH and DELPHI were equipped with silicon vertex detectors. The first vertex detectors had no more than two layers of silicon. After a year of running the beampipe radius was reduced allowing an additional third layer of silicon to be added in DELPHI and the first silicon vertex detectors to be inserted in OPAL and L3. The vertex detectors at LEP supply too few track points to serve as a genuine stand alone device for tracking.

A two layer vertex detector will supply as much information as a three layer one if the sensor layers are fully efficient and the alignment with the other trackers in the experiment is good. Typically the sensors have defects that decrease the detection efficiency and hits for some particle tracks will lose a high precision point. The precision of fitting a track with only one high precision point is very bad. Consequently the third layer will add redundancy to the vertex detector and assist internal and external alignment procedures.

One parameter that indicates the quality of a vertex detector is the error on the impact parameter which is the error on the extrapolation to the interaction point. The error on the impact parameter is given by

$$\sigma_{imp}^2 = \sigma_{geo}^2 + \sigma_{MS}^2 \ ,$$

where σ_{geo} is the error limited by the detector geometry and σ_{MS} is the contribution to the error by multiple scattering.

4.1 Geometrical optimisation of a vertex detector

The formula for the extrapolation error at r=0 for a straight track trough two layers with the resolutions σ_1, σ_2 at radius r_1, r_2 is approximated by

$$\sigma_{geo}^2=(\frac{r_1\sigma_2}{d})^2+(\frac{r_2\sigma_1}{d})^2 ,$$

where d is the lever arm as shown in figure 4.1.

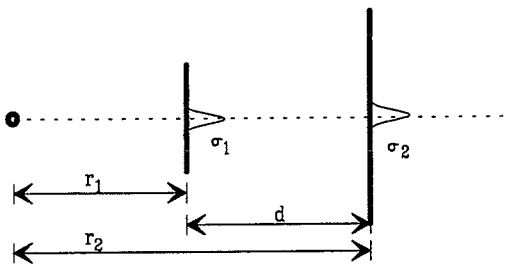

Figure 4.1. A sketch of two sensor layers in a vertex detector.

In order to get a small error on the impact parameter it is obvious that the lever arm should be long or the radius of the sensor layers short and the resolution of the detector layers as good as possible. The resolution of the layers is given first of all by the geometry of the silicon sensors and the noise performance of the electronics but in addition the uncertainty in the geometrical alignment is folded into the resolution.

In the design of the vertex detector there is typically little room for varying the geometrical parameters because of limited space between the main trackers and the beampipe. The background from the beam in the collider limits the radius of the beampipe as well as the radiation tolerance of the sensors and electronics in the tracker. The geometrical optimisation is more a maximising procedure of available space. However in a three layer vertex detector the position of the middle layer can be optimise. For three hit tracks the positioning of the middle layer gives little difference in the performance but the purpose of an extra layer between two layers is mainly to give redundancy when one layer fails and in this way give useful physics data with at least two hits/track. Figure 4.2 shows σ_{geo} as

a function of the position of the sensor layer in the middle when the two other layers have a geometry like in the DELPHI Vertex Detector. The radii of the two fixed layers are 63 mm and 108 mm. The error of the impact parameter at around 80 mm is equal for tracks having hits in the middle outer layers and the closer middle layers. For a full optimisation of the layers the error caused by the multiple scattering which will be discussed in the next section should not be neglected.

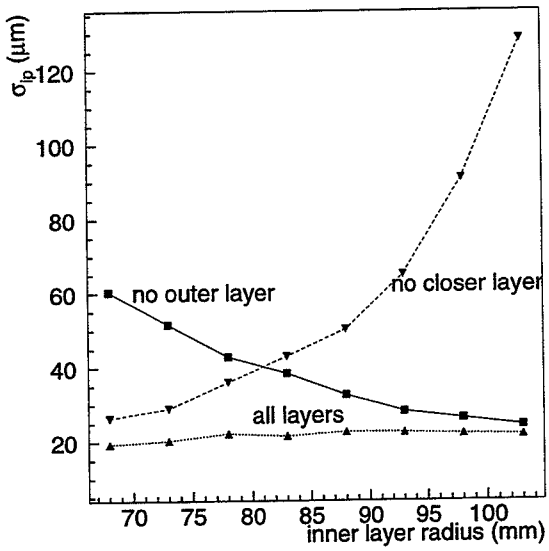

Figure 4.2. The geometrical error on the impact point as a function of the position of the middle layer in the three layer DELPHI Vertex Detector. The closer layer is at r=63 mm and outer layer at r=108 mm.

4.2 Multiple scattering

A particle penetrating material undergoes scattering. This introduces an additional error, σ_{MS}, which affects the extrapolation precision. The projected angle θ, in which a single charged particle is scattered when traversing material, is approximated by

$$\theta = \frac{13.6MeV}{p_T}\sqrt{\frac{x}{X_0}}\left[1+0.088\log_{10}\frac{x}{X_0}\right],$$

where p_T is the transverse momentum of the particle and x/X_0 is the fraction of radiation length of the scattering material[41][42]. The formula is only accurate to 11% for all materials but for most approximations the accuracy of the formula is sufficient. The radiation length can be approximated by

$$X_0 = \frac{716.4 \frac{g}{cm^2} A}{Z(Z+1)\ln\frac{287}{\sqrt{Z}}},$$

where Z is the charge and A is the mass of the material[43]. The radiation length for materials most commonly used in vertex detectors is listed in table 4.1.

Material	δ [g/cm^3]	X_0[g/cm^2]	X_0[cm] calc.	X_0[cm] report.
Be	1.85	65.0	35.1	35.3
Si	2.33	22.1	9.5	9.36
Al	2.70	24.3	8.7	8.9
BeO	3.01	41.5	13.8	14.4
Al_2O_3	3.98	28.3	7.11	7.55
Carbon fiber[a]	1.75	43.1	24.6	
Kevlar[b]	1.45	43.3	29.8	

Table 4.1. The radiation length for some materials used in vertex detectors.

The multiple scattering term in the error of the impact parameter is mainly caused by tracks being scattered in material while the change of particle momentum caused by energy loss can be neglected. The parametrisation of the multiple scattering error is described in ref. [44][45]. The error can be approximated by

[a] Polyacrylonitrile (PAN) based fiber.

[b] Armid fiber introduced by E. I Dupont de Nemours & CO.

$$\sigma_{MS}^2 = \sum_{i=1}^{n} (r_i \theta_i)^2 \quad ,$$

where n is the number of scattering layers. In the three layer vertex detector the position of the middle layer gives little change in σ_{MS}. The graph labelled "all layers" in figure 4.3 shows simulated σ_{MS} term which increases by 20% when the middle layer is moved from r=103 mm to r=68 mm for the geometry described in figure 4.2.The two other graphs in figure 4.3 shows the simulated σ_{MS} term when the track is measured with only two layers closer-middle or middle-outer.

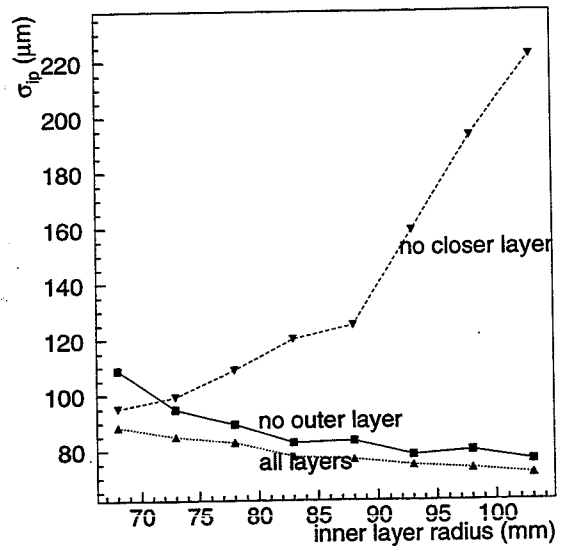

Figure 4.3. The error on the impact parameter for 1 GeV perpendicular tracks.

4.3 The DELPHI vertex detector designs 1989-1994

The DELPHI vertex detector has undergone three major upgrades since the first installation in autumn 1989. The first upgrade was done because of the additional space gained by the reduction of the beampipe diameter in 1991 which allowed a third layer to be added to the existing configuration. In 1994 the detector was upgraded with two layers of double sided sensors giving Rϕ- and Rz-readout. The third upgrade was done for 1996 extending the coverage of the detector by doubling the barrel length and mounting a silicon tracker in the forward regions. The third upgrade is outside the scope of this thesis. The geometries of the three vertex detector designs in DELPHI are shown in figure 4.4.

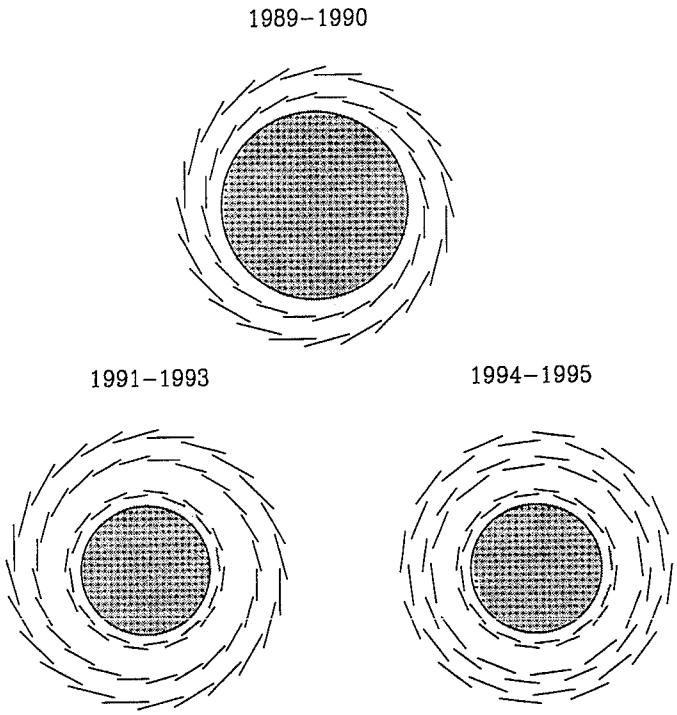

Figure 4.4. The rϕ view of the geometrical lay-out for three versions of the DELPHI Vertex Detector.

The geometry has changed from a design with overlaps in a "paddle-wheel" fashion to a design which is staggered. The geometry was changed mainly for practical reasons allowing a faster change of ladders but it also makes the detector more symmetric having tracks traversing a sensor with angles between -7.5 deg and 7.5 deg instead of 0 deg to 15 deg. In the first upgrade of 1991 the two layer vertex detector got a new layer of single sided microstrip detectors positioned closest to the beampipe, the closer layer. The two old layers, inner and outer, remained unchanged. In the second upgrade 1994 the closer and the outer layers were replaced with new layers of double sided microstrip detectors. Half of the inner layer modules, mounted on small radii, were replaced with modules from the ancient outer layer.

The error on the impact parameter for perpendicular tracks is given in table 4.2 for all the versions. The numbers are generated with Monte Carlo simulation of the vertex detectors in which the thickness and the radius of the layer are averaged.

	r_{BP} mm	$(X/X_0)_{BP}$ 10^{-2}	r_{CL} mm	$(X/X_0)_{CL}$ 10^{-2}	r_{IN} mm	$(X/X_0)_{IN}$ 10^{-2}	r_{OUT} mm	σ_{MS} $\mu m/p_T^2$	$\sigma_{R\varphi}$ μm
A	78.0	1.3	-	-	90.8	0.40	110	130	60
B	53.0	0.4	62.9	0.51	90.8	0.43	110	80	20
C	53.0	0.4	63.2	0.60	89.9	0.43	108	73	22

A=Two layers 1989-90, B=Three layers 1991-1993, C=Double sided 1994-1995
r_{BP}=beam pipe radius, r_{CL}=closer layer radius, r_{IN}=inner layer radius, r_{OUT}=outer layer radius

Table 4.2. The parameters of three DELPHI vertex detector designs and resulting error in impact parameter.

The impact parameter resolution plotted over the momentum range $0.4<p_T<20$ GeV for the three vertex detector designs is shown in figure 4.5.

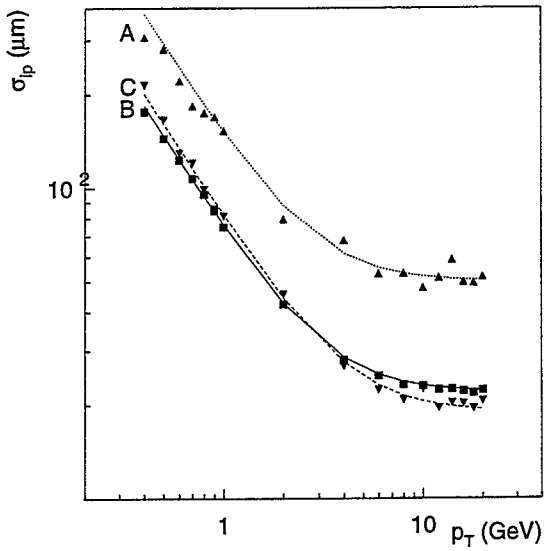

Figure 4.5. The error on the impact parameter as function of transverse momentum for three DELPHI Vertex detector designs. The explanation for A, B and C can be found in table 4.2.

4.4 Alignment of vertex detectors

The optimal resolution of the vertex detector cannot be obtained without proper alignment. The alignment philosophy in the DELPHI Vertex Detector (VD) relies on:

- mechanical accuracy to a reasonable cost
- accurate alignment jigs for every step
- final 3D survey of reference points and detector layers.

The mechanical accuracy of the detector parts in the vertex detector is done with a precision of around 20 μm which can be achieved with standard machines. The main consideration for the mechanical parts is to avoid stress being built into the assembly. Badly machined parts will cause instabilities in the vertex detector that may relax after some time. The assembly jigs have a simpler geometry than

the detector support mechanics and can easily be machined to a precision better than 10 μm. This ensures a precise alignment of the mechanics. The detector ladders shown in figure 4.6 are all aligned under a microscope to around 20 μm precision during assembly. The ladders are slightly deformed by a stiffening bar which is applied, since the vertex detector is self supporting and needs strong detector ladders.

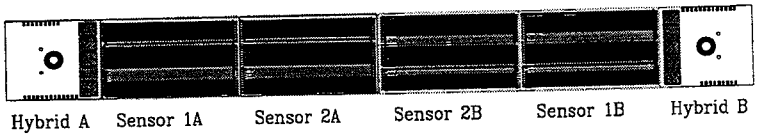

Figure 4.6. A drawing of a detector ladder.

The detector ladders are all measured before mounting to a precision of a few microns with an optical measuring device. The position of the strips in the sensors is measured with respect to two reference points which are on the hybrids supporting the ladders at each end shown in figure 4.7. Every detector ladder holds an entry in the detector database which will be used later in the alignment procedure. In the process of mounting detector ladders the vertex detector is surveyed twice by a high precision probing machine measuring the position of points and surfaces in 3D space. The same reference points measured in the optical survey of the ladders can also be touched. Each sensor in the ladder is touched at five points (the four corners and in the centre) giving a measurement of the bending of the ladders. The VD is surveyed the first time when the outer layer and the inner layer (the middle layer) are assembled. The closer layer is mounted after the closer layer support structure is attached to the mechanical support of the outer layers. This operation may distort the assembly. A second measurement is done afterwards, probing the closer and the outer layers. The two sets of measurements are compared with respect to the outer layer which should remain unchanged between the measurements. Any discrepancy between the two sets of measurements shows that the mounting of the closer layer has distorted the assembly and the position of the inner layer may be altered.

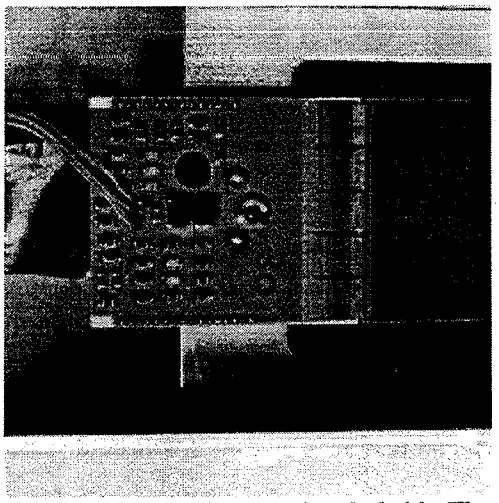

Figure 4.7. A picture of a hybrid. The reference point, a sphere, is screwed into the bush in the center of the hybrid.

The installation of the VD introduces a large uncertainty into the alignment procedure. The vertex detector is transported from the laboratory to the experimental area and installed into the experiment. The transport of the detector and the installation into the experiment may distort the vertex detector. Therefore the VD is re-surveyed after the extraction from the experiment at the end of the year.

The final detector database is obtained by track alignment. The global position of the vertex detector in the DELPHI experiment has to be determined relative to the other sub-detectors in the experiment. The starting point for the track-alignment is taken from the survey database. The complicated procedure of track-alignment is described in ref[46]. The vertex detector is first internally aligned. This is possible since the detector has three layers. Two layers can determine the residual for a hit in the third layer. The overlaps between modules in each layer are especially helpful for this procedure since there are regions with 6-hit tracks. The alignment can either be done using cosmic muons or $\mu^+\mu^-$ from leptonic Z^0 decays. In the alignment procedure the ladders are aligned as units assuming that they are stable. Only those ladders giving big errors on residuals have to be aligned sensor by sensor. The internally aligned VD is finally externally aligned with respect to the rest of the experiment as two solid half-shells.

5. Sensors and electronics

Important components of vertex detectors are the sensors and readout electronics with high density packing of read-out channels giving precise position resolution. The quality requirements are high since a large area is covered with sensors and readout electronics and any defects will degrade the efficiency. The spatial resolution of vertex detectors in LEP is of the order of 5-10 μm. With the current technology for silicon sensors and electronics better resolution could be achieved today, but the gain would give little improvements in physics output with a price to be paid for increased power consumption and money. The performance of silicon strip detectors and readout electronics will be discussed below.

5.1 The silicon strip sensors

The production of silicon sensors by planar technology was introduced in 1980[47]. This technique, typically used for processing integrated electronics, allows processing of small size sensor elements not possible before. A typical silicon strip detector for LEP experiments has ion implanted or diffused p^+-doped strips on the junction side of a high resistivity n-type silicon bulk. The strips are surrounded by a bias line and a p^+-doped guard ring structure. Silicon sensors with only one-dimensional readout have a uniform n^+-doping on the ohmic side. The readout lines shown in figure 5.1 are aluminised either directly on top of the p^+-strips making DC-coupled strips or with a thin coupling oxide in between forming AC-coupled strips[48]. In large devices with many readout channels AC-coupled strips are preferred since they reduce pedestal variations and make the channel offsets insensitive to integration time settings. External capacitors between the sensors and the readout electronics give an alternative way to AC-couple strips[49]. This method reduces the complexity of the sensors but gives problems connected with processing high value densely packed coupling capacitors together with one extra bond-wire per readout channel.

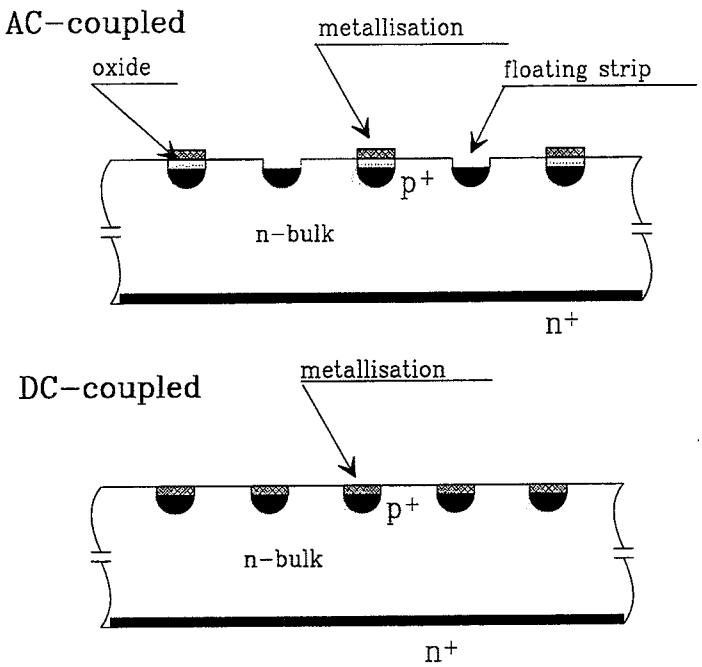

Figure 5.1. A schematic drawing showing AC-coupled strips with a floating strip in between and DC-coupled strips.

A method to get good position resolution with a reduced number of readout channels is to leave "floating" strips not connected to electronics between strips read out[50]. The charge deposited between readout lines is capacitively coupled to the closest strips but the "floating" strip will capacitively couple an equal amount of the charge to the neighbouring strips which are read out. The position of the track is obtained by comparing the pulse heights and correcting the interpolated position by an experimentally measured η-distribution[51].

The polarisation of the sensor is done on the junction side either by static biasing or dynamic biasing. Static biasing can be achieved with polysilicon resistors[52] which today can reach a value of around 100 MΩ for a typical sensor geometry in LEP. The polysilicon resistors are directly processed onto the sensors with both the strip implants and the biasing line connected to the resistors through contact holes. Dynamic biasing is done by a transistor-like "reach-through" structure[53] which can have the gate connected making the value of the dynamic resistor tunable[54]. Dynamic biasing needs less complex processing than static biasing and it also gives higher resistor values. The static

biasing scheme is more robust and can as well be implemented on the ohmic side of the sensor when needed. On the ohmic side dynamic biasing can be realised using electron accumulation layers[55].

5.2 Double-sided silicon strip sensors

Sensors which are optimised for low radiation length and supply two-dimensional position information, are processed on both sides with some angle between the strips on each side. The vertex detectors in LEP experiments have perpendicular strips since the clean environment makes it easy to select real hits from "ghost" hits and comparable resolution can be achieved in both directions.

The processing of strips on the ohmic side is troublesome because the electrons under the SiO_2 surface make the side conductive. The separation of the n^+-doped strips is typically obtained by introducing either p^+-doping between the strips or aluminum field-plates on top of the strips or between the strips. The strips separated by field plates as in the DELPHI VD have to be AC coupled because the metallisation needs a different potential than the implant in order to create a field around the strip and break the conduction between strips. This method of separation is far from trivial since the voltage over the thin coupling oxide might create pinholes turning the AC coupled strip coupled into DC and making a short circuit between the polarisation voltage and the electronics at a potential close to ground. In addition the MOS structures are not favourable regarding micro discharges. The use of p^+-separation with floating electronics give a more robust way of separating strips. Figure 5.2 shows two methods of separating the ohmic side.

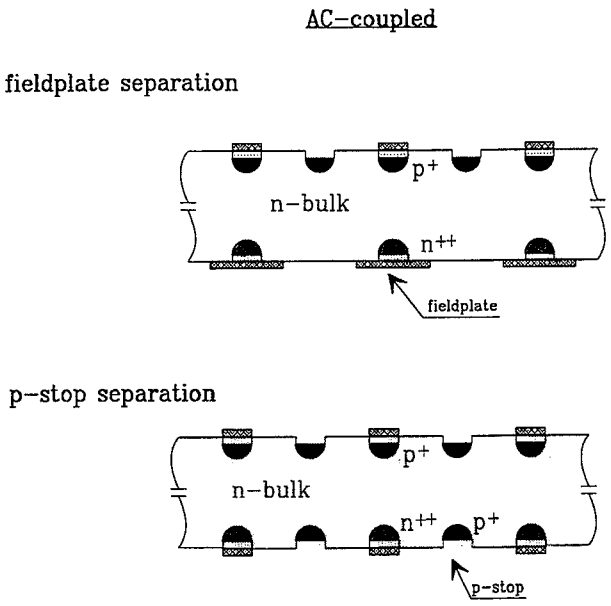

Figure 5.2. Two methods for separating the strips on the ohmic side of a sensor.

The perpendicular strips create an additional problem when the aim is to minimise material in the active area. In contrary to the strips on the junction side ending at the edge outside the active area, the strips on the ohmic side end at the edge in the active area. The strips on the ohmic side can be rerouted to the same edge as the junction side strips if an additional routing layer is added. This is either done by an extra routing kapton[56] foil or a quartz plate[57] which is mounted and bonded onto the sensor, or by integrating the routing lines on the sensor with a double-metal process. The DELPHI VD introduced the double-metal technology on microstrip sensors achieving a fully integrated double sided sensor. The process is demanding requiring a layer of thick insulator made of polyimide or silicon oxide between the first metallisation layer on top of the strips and the second metallisation perpendicular to the first one, routing the signals to the bonding pads. The second metal layer is connected through the thick insulator to the first metallisation with contact holes. Steep edges of the contact holes create an additional challenge for the process to get the second metallisation in contact with the first without interruptions.

5.2.1 Parasitic capacitance from the double-metal layer

The main noise contribution comes from interstrip capacitance which usually limits the maximum length of the sensor ladder. The interstrip capacitance per nit length is a function of the strip pitch and the implant width. For double-sided sensors with double-metal readout the capacitance calculation gets more complicated because of the additional capacitance coming from the double-metal coupling. A naive calculation would take into account only the square geometrical intersections of metal strips: This simple model gives a capacitance more than an order of magnitude less than measured (in fact 1/15). Another model[58] is based on grid capacitances seen by individual strips. In this model, a strip of layer 1 sees a complete grid above itself, with a coefficient $\alpha<1$ which is the electrostatic "transparency" of the grid ($\alpha=1$ for a full plane). The fact that a single strip is capacitively coupled to a complete grid comes from the multiplexing structure, and implies that a single strip is then connected to the complete sensor. In the same way, a single strip of metal layer 2, the upper one (5 μm wide) sees a total capacitance resulting from the whole underlying structure, which has a "plane-equivalent" coefficient α very close to 1, due to the presence of silicon dioxide and fixed charges inside it. The values of the α coefficient can be determined by electrostatic simulations or by tuning the model to measurements.

In the model, the total capacitance seen by one metal output of layer 2 is the following:

$$C = \varepsilon_0 \varepsilon_r \frac{w_2(1+k_2)N_1 p_1 \alpha_1 m + w_1(1+k_1)N_2 p_2 \alpha_2}{t},$$

with ε: dielectric constant of oxide (3.9)
w: width of strip
k: fringing of strips
N: number of strips in the opposite layer
p: interstrip pitch
α: electrostatic grid coefficient
m: multiplexing number
t: thickness of oxide (1 to 2.5 μm).

Typical values of the electrostatic parameters are:

w_1 = 18 μm:

t	$(1+k_1)$	α_2
1 μm	1.12	1/5.9
2 μm	1.19	1/4

w_1 = 11 μm:

t	$(1+k_1)$	α_2
1 μm	1.19	1/5.9
2 μm	1.28	1/4

w_2 = 5 μm, m=3:

t	$(1+k_2)$	α_1
1 μm	1.12	1
2 μm	1.19	1

As an example, sensors in the closer layer ladder have the following specifications;

- first metal length: 19.2 mm
- first metal width: 11 μm
- oxide thickness: 2 μm
- second metal length: 76.8 mm
- second metal width: 5 μm.
- multiplexing number: 3.

The capacitance of this type of sensor comes from the interstrip capacitance, which is measured to be 1.2-1.4 pF/cm, and an extra contribution from the parasitic capacitance. Calculating the parasitic capacitance using the formula and adding the interstrip capacitance gives for this sensor a capacitance of 17.1 pF where the contribution from the first metal layer is 9.2 pF, or 1.6 pF/cm, and from the second metal layer 7.9 pF, or 1.0 pF/cm. For a design with half the oxide thickness the corresponding value is 24.7 pF with a contribution from the first metal layer of 9.8 pF and from the second metal layer of 14.6 pF.

5.3 Readout electronics for the double-sided double-metal sensors in the DELPHI VD

The front-end electronics for silicon strip sensors need high channel density and low power consumption. The readout pitch of the DELPHI VD sensors are 50 μm and 1-2 mW/channel can still be safely cooled. The front-end chip used in the DELPHI VD has 128 channels with charge sensitive amplifiers and multiplexed output[59][60]. The front-end for the single-sided sensors, MX3, was upgraded for the double-sided sensors to MX6 with a better noise performance. The reason for the upgrade was the high capacitance of the double-sided sensors which with the old MX3 readout circuit would have resulted in too low a signal-to-noise ratio to give a comfortable resolution and detection efficiency.

5.3.1 MX6 noise

The noise in a read-out channel comes from several sources. The amplifier itself has a noise which couples to the next amplifiers via the sensor. Every resistor in the detector coupled to the amplifier inputs also contributes. The serial noise comes from the transistor noise resistance, R_s, and from the protection resistor, R_{pr}, in series with the input. R_s has been measured on test structures under standard working conditions to 330 Ω. R_{pr} amounts to 300 Ω. The stray capacitance is C_x = 10 pF. The squared Equivalent Noise Charge (ENC^2) for a channel connected to a total detector capacitance, C_D, shared between its two nearest neighbours (p-side case), is given by

$$ENC^2 = 2kT\frac{A_{fs}}{t_p}[((C_x+C_D)^2 + \frac{C_D^2}{2})R_s + \frac{3}{2}C_D^2R_{pr}],$$

where t_p is the integration time. The coefficient A_{fs} depends on the integration time and for a typical t_p=2 μs the value is 4.1. Using the numerical values given above, one expects an asymptotic slope of 25 noise electrons per additional pF, if C_D is large compared to C_x. In the n-side case where the coupling between the two metal layers gives the main contribution to the input capacitance, the formula becomes:

$$ENC^2 = 2kT\frac{A_{fs}}{t_p}[R_s(C_x + C_D)^2 + C_D^2R_{pr}]$$

and the asymptotic slope is 20 electrons per pF.

The main contribution to the noise is the capacitance but the contribution from sheet resistance of long and thin read-out electrodes plays a major role. The read-out line resistance will multiply with the capacitance changing the noise slope. Figure 5.3 show the noise slope for the MX6 front-end chip with and without an extra 400 Ω strip resistance R_s.

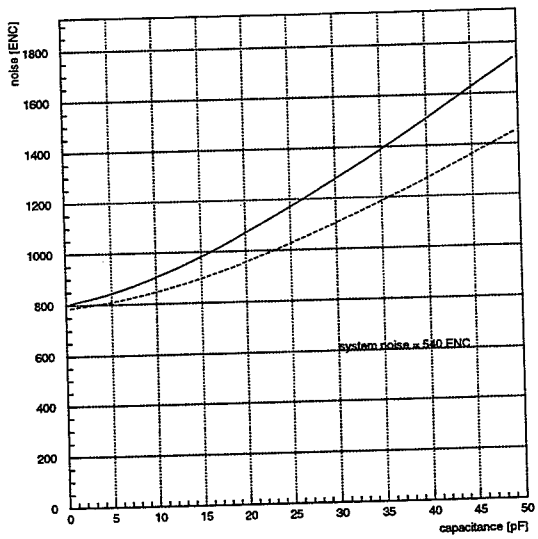

Figure 5.3. Noise versus capacitance for a strip with R_s = 0 Ω (dashed curve) R_s = 400 Ω (solid curve).

The strip resistance decreases as the strip width grows larger but again the capacitance between the two metal layers increases. For the DELPHI sensors the strip width varies between 5 μm and 7 μm giving an R_s between 25 Ω/cm and 50 Ω/cm.

6. Silicon trackers for LHC

The success of silicon vertex detectors in e^+e^- machines has made the use of silicon attractive to pp-colliders such as LHC[61][62] and Tevatron[63][64] as well. In all the major proposals for experiments at pp-machines large areas of silicon are suggested for the central tracker. The tolerance of ionizing radiation and fast propagation of the charge make solid state detectors suitable for the environment close to the interaction point. The purpose of building solid-state trackers in the highly complex event topologies at the pp-colliders is mainly to reject background and enhance the granularity for tracking. Two multipurpose experiments, ATLAS and CMS, and a dedicated b-physics experiment will be constructed at the LHC-collider.

6.1 Physics at low luminosity

In the startup phase of the LHC-collider, which may take a few years, the luminosity is not foreseen to reach the design value. At low luminosity the aim is to concentrate on heavy flavour physics. The radiation background in this period is not as severe as it will be at high luminosity, which may allow an extra silicon strip or pixel layer to be added very close to the interaction point. With an extra layer at small radius the b-tagging can be improved by better vertex separation. The added layer will not survive a long time at full luminosity but the plan is to remove it when necessary. The centre-of-mass energy for the LHC-collider is above the $t\bar{t}$ threshold (320-400 GeV) giving an opportunity to study all the quark families. The Higgs particle will probably remain undetected until the high luminosity period because of the low cross-section. The plans for the startup phase place strong demands on a properly working detector for exploiting the physics potential of CP-violation.

6.2 Physics at high luminosity

At high luminosity the main goal for all multipurpose LHC experiments is to complete the study of the Standard Model by discovering or excluding the Higgs particle and possibly discovering new physics signatures like SUSY sparticles. For all processes the cross-section is low, requiring high luminosity. In the ATLAS experiment the silicon tracker, called the SemiConductor Tracker (SCT), will contribute to the momentum resolution in searching for the Higgs in the mass regime 120 GeV to 170 GeV in the four lepton decay channel shown in figure 6.1. Generally the SCT is important for background rejection and pattern-recognition at high luminosity. Because of the very severe background the heavy quark events will not have a high purity and efficiency like at LEP.

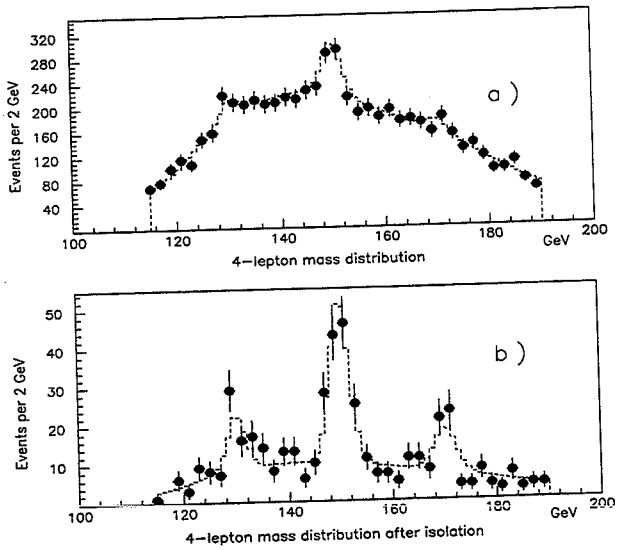

Figure 6.1. Signal for $H \rightarrow Z^0Z^{0*} \rightarrow$ llll (m_H=150 GeV) a) with and b) without track isolation cuts.

6.3 Instrumentation of trackers at LHC

At high luminosity the limiting parameter for the distance from the interaction point to the first layer of sensors is the radiation hardness. The event rate and detector occupancy will be severe requiring the closest detector layer to survive 10 Mrad ionizing radiation and particle fluxes equal to 10^{14} neutrons/cm^2 for a 10 year period. The high trigger rate and radiation level push current technology to the limit. A comparison of parameters for the DELPHI VD and the proposed ATLAS SCT is listed in table 6.1.

	ATLAS-SCT	DELPHI-VD
Radius	20-60 cm	6-15 cm
Active surface	~40 m^2	~0.7 m^2
Number of modules	~3000	72 (×2)
Number of readout channels	2.9 M	0.126 M
Power	10 kW	0.15 kW
Position resolution	<20 μm (rφ) <500 μm (rz)	7 μm (rφ) 20 μm (rz)
Time resolution	25 ns	2.2 μs
Radiation tolerance (10 years)	10 Mrad [c] 10^{13}-10^{14} n/cm^2 [d]	10 krad [c]

Table 6.1. Parameters for the DELPHI VD and the proposed ATLAS SCT.

Apart from the future silicon tracker being an order of magnitude larger, the biggest challenge will be the radiation tolerance and speed requirements. Research and development has continued for several years to find a solution for sensors and electronics for silicon trackers. The radiation damage can be classified in two categories; bulk damage and surface damage, which influence the performance differently:

[c]Charged particles.

[d]Particle fluxes normalized to 1 MeV neutrons.

- The radiation damage from charged particles causes surface damage, develops rapidly even at low doses and reaches full saturation at a few hundred krads.
- The damage from particles displacing the crystal lattice in the bulk material is a continuous process and the damage is cumulative.

6.3.1 Sensors

With an optimised design the effects from surface damage can be minimised. When the surface damage reaches saturation the interstrip capacitance will be 1.5 to 2 times higher than that for an un-irradiated sensor. The interstrip resistance will fall to about half. These effects will of course increase the noise seen by the front-end. However, the robustness of the front-end should be good enough to conform with increased noise.

A sensor made of n-type bulk silicon will after a few years in LHC turn intrinsic and later into p-type as shown in figure 6.2[65]. The junction will move from one side of the silicon to the other side. With increased bulk damage a higher bias voltage is needed to deplete the detector, increasing the leakage current and noise. The depletion voltage may in the end exceed the breakdown voltage of the diodes forcing the sensor to be operated underdepleted. The detector geometry can be optimise to reach high voltages (300-400 V) before breakdown, but this may not be enough for LHC. By using n-strips on p-bulk material or n^{++}-strips on n-bulk the effect of the migration of the junction can be minimised. The bulk damages will limit the lifetime of a silicon sensor in the experiment, since running underdepleted will degrade the performance, and the high leakage current in the sensors increase the risk for thermal runaway. In the LEP experiments there is no need for cooling the sensors since the leakage current is low (nA per strip) but at LHC the leakage current will be high (μA per strip). The reason for the concern is that thermal runaway in sensors is a fast process since the leakage current is temperature dependent and the temperature is current dependent. High leakage current warm up the sensor which make it draw even more current.

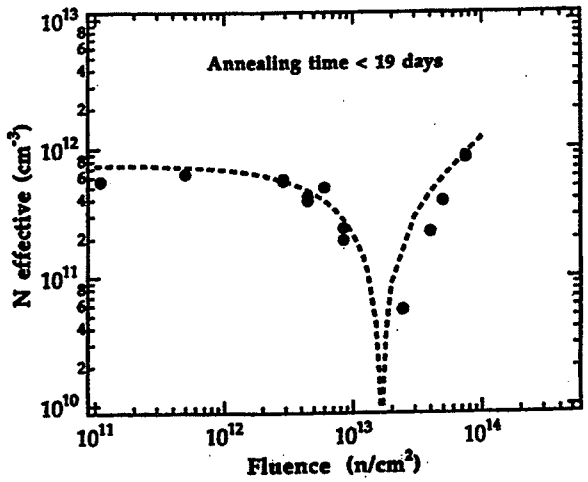

Figure 6.2. Doping concentration of the silicon bulk vs fluency.

6.3.2 Front-end electronics

The front-end electronics is much less sensitive to bulk damages since in contrary to the sensors the bulk is not depleted. Particles traversing the bulk may however cause single event upset "latch-up", which can be harmful in a big tracker. The surface damage, on the other hand, is a problem to be addressed in the design. Some especially radiation hard processes exist, such as Silicon On Insulator (SOI), Silicon On Sapphire (SOS) and specially treated radiation hard bulk CMOS, for producing radiation hard front-end electronics. The bipolar processes appear to be radiation hard by default. The present noise performance of radiation hard processes is not as good as for non-radiation hard CMOS, but since the radiation hard processes typically are only optimise for digital electronics the adaptation to analogue low-noise electronics will take some time. A power consumption below 2 mW/channel and a time resolution better 25 ns with a channel noise below 1500 RMS electrons after irradiation with a 20 pF load from the sensor has to be reached for LHC. The most promising technique to achieve the fast time-response

is to use bipolar technology. The process has first to be proven radiation hard at levels required at LHC before it can be used. A different approach to reach fast time information by using slow shaping has been studied[66]. With a deconvolution filter the time stamp can be recaptured from a slow pulse. This technique saves power in the front-end because of its slower risetime. The extra power required for the deconvolution is small since the deconvolution is done after the trigger, which has reduced the data sample from 40 MHz to 100 kHz.

7. Conclusions

One of the most appealing ways for probing the Standard Model at the LEP collider is to study decays of hadrons flavoured with heavy b-quarks. Because of the clean machine background and the vertex detectors constructed of silicon microstrip sensors the conditions for high precision measurements are good at LEP.

DELPHI is one of the first collider experiments installing silicon vertex detectors. The silicon detector was installed already in 1989 and has in recent years been upgraded several times. In order to achieve high precision tracking with high efficiency, the DELPHI detector has three layers of silicon. Three silicon layers allow internal alignment of the detector and adds redundancy to the tracking without having the performance degraded by multiple scattering. With the concept of selfsupporting ladders and double-metal processing of silicon sensors low mass can be achieved in the volume used for tracking. The double metal process and long ladders have a drawback in the increase of sensor capacitance. Properly designed front-end electronics can, however, allow high capacitance maintaining good signal to noise ratio.

At the next collider at CERN, the LHC, the environment close to the collision point will be very different from that at LEP. High levels of radiation and big amounts of particle tracks to be detected place high requirements on the instrumentation. In addition, the silicon trackers at LHC will in every aspect be one order of magnitude bigger than the silicon vertex detectors at LEP. The components to be used for the construction need to be radiation hard and much faster than the components running at LEP. Prototype analogue frontend electronics has been designed to meet the requirements. The electronics, yet to be implemented in commercially available radiation hard processes, has shown to meet the speed requirements in testbeam and laboratory conditions.

References

[1] LEP Design Report, CERN-LEP/84-01, (June 1984).

[2] J.M. Jowett, CERN SL/93-24, (10 May 1993).

[3] Design Study of the Large Hadron Collider, CERN 91-03.

[4] Proceedings of the LEP summer study, CERN 79-01 Volume 1, (14 February 1979).

[5] DELPHI Collaboration, CERN/LEPC 83-3, (17 May 1983).

[6] DELPHI Collaboration, Nucl. Instr. and Meth. A303 (1991) 233-276.

[7] L. Bugge et al., DELPHI 94-9 PHYS 354, (26 January 1994).

[8] A. Benvenuti et al., DELPHI 94-31 CAL 112, (23 March 1994).

[9] Y. Sacquin, DELPHI 92-41 TRACK 70, (31 March 1992).

[10] R. McNulty, DELPHI 92-40 TRACK 69, (27 March 1992).

[11] W. Adam et al., CERN-PPE/93-154, (5 August 1993).

[12] G. van Apeldoorn et al., DELPHI 94-18 RICH 61, (16 February 1994).

[13] W. Adam et al., DELPHI 93-137 RICH 59, (26 November 1993).

[14] W. Adam et al., IEEE Trans. Nucl. Sci. 39 (1992) 166.

[15] Y. Golfand and E. Likhtman, JETP Lett. 13 (1971) 232;
D. Volkov and A. Akulov, Pis'ma Zh.ETF 16 (1972) 621;
P. Ramond, Phys. Rev. D3 (1971) 2415.

[16] H. Georgi and S. L. Glashow, Phys. Rev. Lett. 32 (1974) 32;
J. Pati and A. Salam, Phys. Rev. D10 (1974) 257.

[17] H. Georgi and S.L. Glashow, Phys. Rev. Lett. 32 (1974) 438.

[18] U. Amaldi, W. DeBoer, H. Furstenau, Phys. Lett. B260 (1991) 447.

[19] U. Amaldi, CERN-PPE/91-88, 3 June 1991 (to be published in Annals of the New York Academy of Science).

[20] M. Gell-Mann, Phys. Lett. 8 (1964) 214.

[21] G. Zweig, CERN TH-401, (1964);
G. Zweig, CERN TH-412, (1964).

[22] M. Gell-Mann and Zweig, Phys. Rev. 125, 3 (1962) 1067.

[23] LEP collaborations, Phys. Lett. B276 (1992) 247.

[24] S.I. Glashow, Nucl. Phys. B 22 (1961) 579;
S. Weiberg, Phys. Rev. Lett. 19 (1967) 1264;
A. Salam, in Proc. of the 8th Nobel Symp., p 367, ed. N. Svartholm, Almqvist and Wiksell, Stockholm 1968.

[25] P.W. Higgs, Phys. Lett. 12 (1964) 132;
P.W. Higgs, Phys. Rev. Lett. 13 (1964) 508;
P.W. Higgs, Phys. Rev. 145 (1966) 1156.

[26] N. Cabibbo, Phys. Rev. Lett. 10 (1963) 531.

[27] M. Kobayashi and T. Maskawa, Prog. Theor. Phys. 49 (1973) 652.

[28] J. Schwinger, "Particle, Sources and Fields" Vol II, Addison-Wesley, (1973).

[29] J. Jersak, E. Laermann and P. M. Zerwas, Phys. Lett. 98B (1981) 363 and Phys. Rev. D25 (1982) 1218.

[30] B. A. Kniehl and H. J. Kühn, Phys. Lett. 248B (1989) 229.

[31] B. Adeva et al., Phys. Lett. 241B (1990) 416.

[32] C. Peterson, D. Schlatter and L.L Zerwas, Phys. Rev. D27 (1983) 105.

[33] B. Andersson, G. Gustafson and B. Söderberg, Z. Phys. C20 (1983) 317.

[34] M.G. Bowler, Z.Phys. C11 (1981) 169.

[35] D.A. Morris, Nucl. Phys. B 313 (1989) 634.

[36] Z Physics at LEP 1, Edited by G. Altarelli, R. Kleiss and C. Verzegnassi, CERN 89-08 Vol. 1 (21 September 1989).

[37] Tasso Coll. Z. Phys. C, 44 (1989) 1.

[38] C. de la Vaissière and S. Palma-Lopes, DELPHI 89-32 PHYS 38, (11 April 1989).

[39] P. Branchini, M. Ciuchini and P. Del Giudice, DELPHI 92-20 PHYS 159, (25 February 1992).

[40] Tasso Coll. M. Althof et. al., Phys. Lett. 149B (1984) 524.

[41] V. L. Highland, Nucl. Instr. and Meth. 129 (1975) 479.

[42] G. R. Lynch and O. I. Dahl, Nucl. Instr. and Meth. B58 (1991) 6.

[43] Y-S. Tsai, Rev. Mod. Phys. Vol. 46, 4 (1974) 815.

[44] A. Katchko, FERMILAB-Pub-92/46.

[45] P. Billoir, Nucl. Instr. and Meth. 225 (1984) 352.

[46] N. Bingefors et. al., Nucl. Instr. and Meth. A328 (1993) 447-471.

[47] J. Kemmer, Nucl. Instr. and Meth. 176 (1980) 449.

[48] M. Caccia et al.,Nucl. Instr. and Meth. A260 (1987) 124.

[49] G. Batigani et al., Nucl. Instr. and Meth. A310 (1991) 160.

[50] J.B.A.England et al.,CERN EP 80-218 (1980).

[51] I. Hietanen et al., Nucl. Instr. and Meth. A310 (1991) 671.

[52] L. Evensen et al., Nucl. Proc. 4th Int. Conf. on Solid State Sensors and Actuators, Tokyo, Japan, June 1987.

[53] P. Holl et al., IEEE, Trans. Nucl. Sci. NS-36 (1989) 251.

[54] P. P. Allport et al., Nucl. Instr. and Meth. 301 (1991) 155.

[55] G. Batignani et al., Nucl. Instr. and Meth. A269 (1991) 160.

[56] D. DiBitonto et al.,Nucl. Instr. and Meth. A338 (1994) 404.

[57] P.P Allport et al., CERN-PPE/94-16 (28 January 1994).

[58] Private communication with J. Lounis.

[59] J. C. Stanton, RAL-89-009 (1989).

[60] J. Stanton and N. Kurtz, RAL-89-028 (1989).

[61] ATLAS Collaboration, Letter of Intent, CERN/LHCC/92-4, (1 October 1992).

[62] CMS Collaboration, Letter of Intent, CERN/LHCC 92-3, (1 October 1992).

[63] CDF Collaboration, The CDF Upgrade, Nucl. Phys. Proc. Suppl. 44, (1995).

[64] D0 Collaboration, The DO upgrade, Nucl. Phys. Proc. Suppl. 44, (1995).

[65] RD20 Collaboration, Status report to the DRDC, CERN/DRDC 92-28, (13 May 1992).

[66] N. Bingefors et al., Nucl. Instr. and Meth. A326 (1992) 112.

Publication 1.

Nuclear Instruments and Methods in Physics Research A301 (1991) 116–120
North-Holland

Ion-implanted silicon detectors processed on a 100 mm wafer

Iiro Hietanen, Jukka Lindgren, Risto Orava and Tuure Tuuva
University of Helsinki, Helsinki, Finland

Richard Brenner
Åbo Akademi, Turku, Finland

Mikael Andersson, Kari Leinonen and Hannu Ronkainen
Technical Research Center of Finland, Espoo, Finland

Received 15 October 1990

A planar process for manufacturing large silicon detectors on a 100 mm wafer has been developed. Several oxidation and annealing temperatures were studied in order to optimize detector performance. A strip detector with an active area of 32×58 mm^2 together with various single detector diodes were processed and tested. The 1280 strip detector with 25 μm strip and readout pitch was connected to multiplexing LSI electronics and tested with tracks from a ^{90}Sr beta source. The most probable signal pulse height was found to be 14 times the σ_{noise} of any individual channel.

1. Introduction

The use of planar silicon detectors in both position sensitive and energy dispersive applications has rapidly increased. Detector systems of large angular coverage unavoidable consists of a large number of individual detector plates traditionally processed on 3 in. silicon wafers. The effective wafer processing area is almost doubled by the use of 100 mm wafers, enabling detector designs with less inactive material and fewer electrical connections.

In order to adapt the standard 100 mm IC processing steps to detector manufacturing, several oxidation temperatures and two different ion-implantation annealing approaches were studied. The design, processing and electrical characteristics of the manufactured single diode and strip detector are described. Results from the first strip detector tests with minimum ionizing particles are presented.

2. Design

The large available area on the silicon wafers enabled the design of a 32×58 mm^2 strip detector together with a great variety of detector diodes equipped with guard-ring or field-plate electrodes. The strip detector area was chosen to be compatible with the detectors manufactured for the Microvertex detector of the DELPHI experiment [1], whereas the round and square diodes had an active area of 0.01 mm^2 to 1 cm^2. For the production of these directly coupled detectors, two photolithographic mask levels were needed, one for defining the p^+ implants and another for patterning the diode aluminizations.

The layout design of the rectangular, symmetric 1280 strip detector is presented in fig. 1. The strip pitch is 25 μm, whereas the readout pads, located in the two ends of the detector by turns, are in two parallel rows at a pitch of 50 μm. In order to ensure sufficient breakdown characteristics, 12 floating guard rings were located as the outermost structures. In addition, a 50 μm wide guard diode was placed outside the strip area to prevent edge currents from reaching the active detector area. The mask width of the strip and outer guard ring implants was 5 μm.

3. Processing

The CMOS processing line of the Technical Research Center of Finland was utilized for the detector processing. The thickness of the acquired 100 mm silicon wafers was 525 μm and the resistivity range 1400–2600 Ω cm.

Several process variations were utilized to study two different processing philosophies: maintaining the raw material properties by using only low processing temperatures, or even improving the material characteristics by using standard IC manufacturing temperatures with

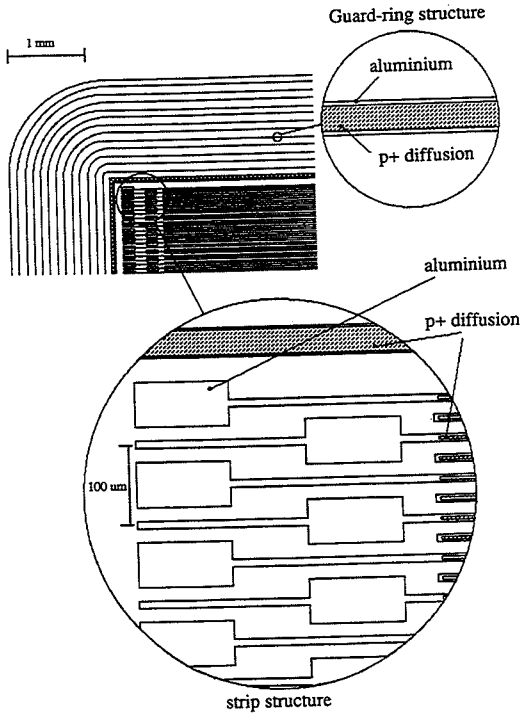

Fig. 1. Strip detector layout design.

backside gettering. The 1.1 μm field oxide was processed by a combination of a thermal pyrogenic oxidation step (800 °C) and a LPCVD LTO (low temperature oxide) step. After the first resist step, the field oxide was patterned by wet chemical etching in BHF (buffered hydrofluoric acid). The resist was stripped by O_2 plasma etching. For the ion-implantation steps a thin thermal oxide (20 nm) was grown by a pyrogenic oxidation step at 800 °C. The boron junction implant and phosphorus back-plane implant were performed at an energy of 20 keV to a dose of 5×10^{14} cm^{-2}, and at 30 keV to 3×10^{15} cm^{-2}, respectively. A low annealing temperature of 800 °C was utilized in two process variations, whereas a known efficient gettering method, the combination of back-side implantation, heavy phosphorus doping and annealing at 900 °C, was exploited in another two anneals. The front-side aluminization was sputtered after etching the implantation oxide. The 50 nm aluminium was patterned in the second photolithographic step and the resist was stripped again using O_2 plasma. Finally, the 500 nm back-side aluminization was sputtered.

4. Results

4.1. Electrical measurements

Various capacitance and current measurements were utilized for evaluation of the wafer material and

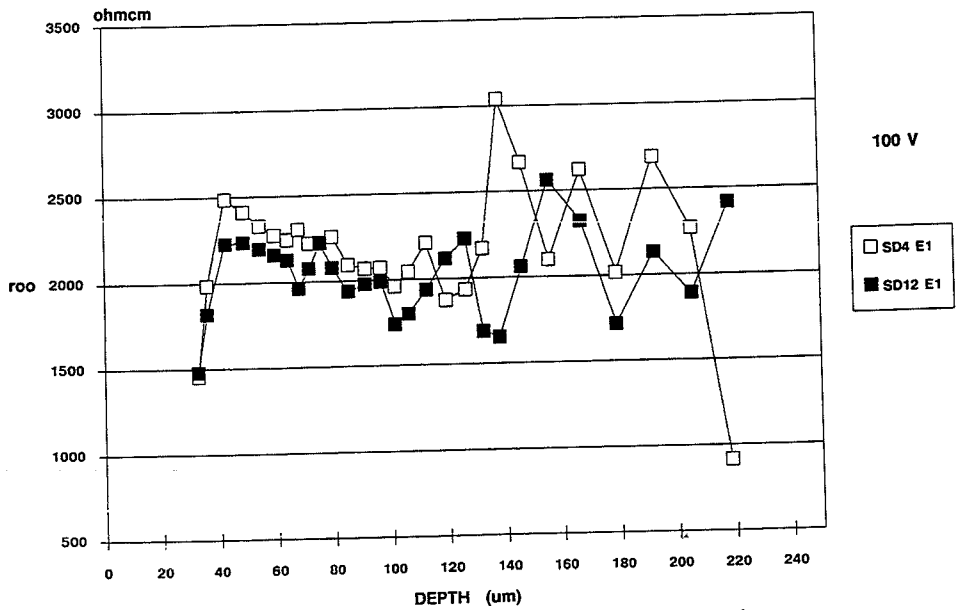

Fig. 2. Wafer resistivity as a function of distance from the wafer surface.

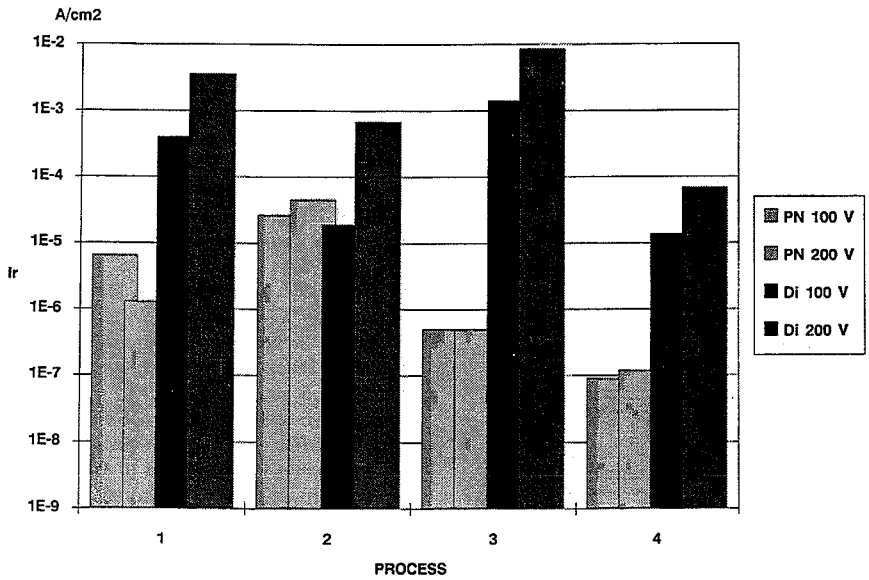

Fig. 3. Leakage currents in the four different anneal variations.

processing qualities as well as for characterization of the basic detector structures.

The resistivity profiles of the silicon wafers were studied in diode $C-V$ measurements showing results quite similar to those given by the manufacturer. In fig. 2, the silicon resistivity as a function of distance from the wafer surface is presented.

The four different process variations were compared by measuring diode leakage currents from structures equipped with guard rings. The vertical pn-junction

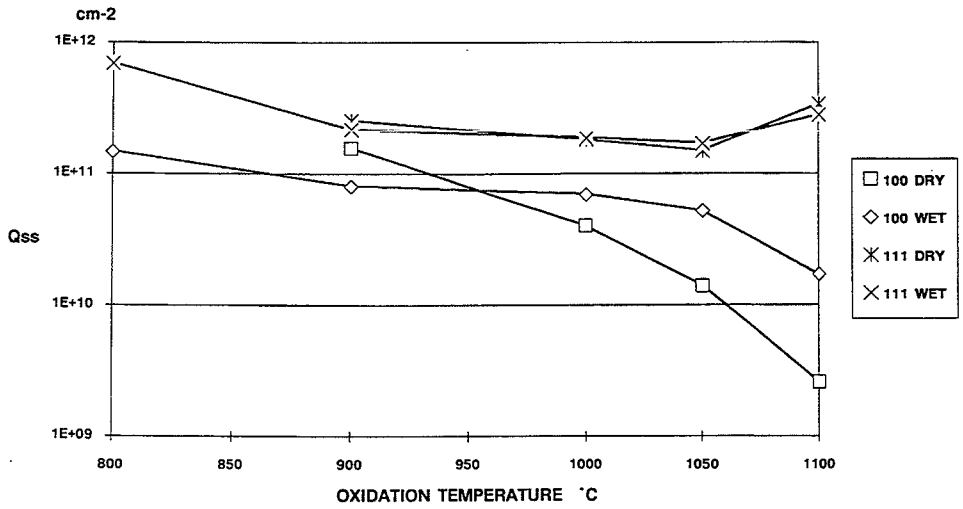

Fig. 4. Reduced effective oxide charge as a function of oxidation temperature.

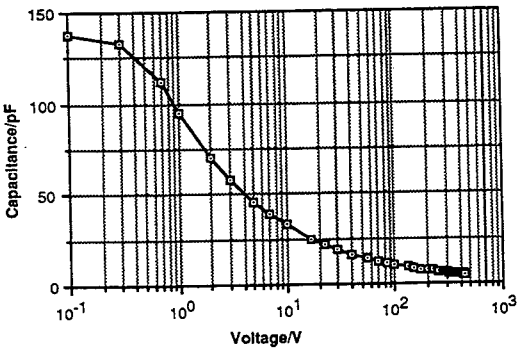

Fig. 5. Diode $C-V$ measurement.

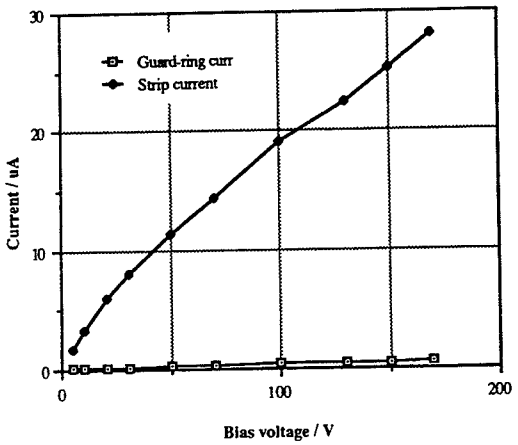

Fig. 6. Leakage current of detector SD10-10.

current in these diodes was also measured by collecting the diode surface and edge currents to the innermost biased guard ring. Results from these measurements are presented in fig. 3. The large contribution of the lateral current components can be clearly seen in all the anneal variations. This was due to the positive oxide charge and surface states present in the silicon–silicon dioxide interface. The main reason for the relatively high oxide and interface charge densities was the low oxidation temperature. Remarkably lower current in the process #4 is explained by gettering during the longer anneal at 900 °C.

In order to optimize the oxidation parameters for further detector processing runs both ⟨100⟩ and ⟨111⟩ oriented silicon wafers were oxidized in different process temperatures. The lowest reduced effective charge density for ⟨111⟩ silicon was measured around 1050 °C both in dry and wet oxidation steps, fig. 4.

The depletion characteristics of the processed detector diodes were studied by measuring a $C-V$ curve for a 5 mm × 5 mm square diode. Results from the measurement utilizing a capacitance bridge with generator frequency of 10 kHz are shown in fig. 5. Derived from the thickness and resistivity of the silicon wafers, a depletion voltage around 400 V was expected. Interpretation of the $C-V$ behaviour is somewhat complicated due to the lateral spread of the depletion region and limitations arising from the diode breakdown characteristics. Over the whole measurement range the $1/\sqrt{V_{\text{bias}}}$ dependence of the depletion capacitance is evident.

4.2. Strip detector measurements

For further tests with minimum ionizing particles, a strip detector of the process variation #4 (anneal at 900 °C), junction depth $x_j = 0.52$ μm) was bonded to NMOS Microplex readout chips [2] in both ends of the detector to enable interleaved readout at a pitch of 25 μm. The leakage current of this detector is presented in fig. 6, where the square-root behaviour, characteristic of the bulk generation current, is clearly seen.

The interstrip capacitance between two neighbouring strips was measured in a region of 11 adjacent strips. As shown in fig. 7, the average capacitance value was 9.7 pF for the 58 mm strips, i.e. 1.7 pF/cm. This value is explained by the presence of oxide and silicon–silicon dioxide interface charges discussed above.

A special setup utilizing scintillator triggers was used in the measurements with electrons from a ^{90}Sr source. Analog data from the readout chips was AD converted in a SIROCCO unit [3] and further transferred into a Macintosh computer. In order to achieve readout coincidence, i.e. detector readout when the actual signal from an electron was present in the detector, the scintillator trigger signal had to be synchronized with the readout timing. The wide energy range of the ^{90}Sr source also required a certain energy threshold for the acceptable trigger signals. A detector bias voltage of 200

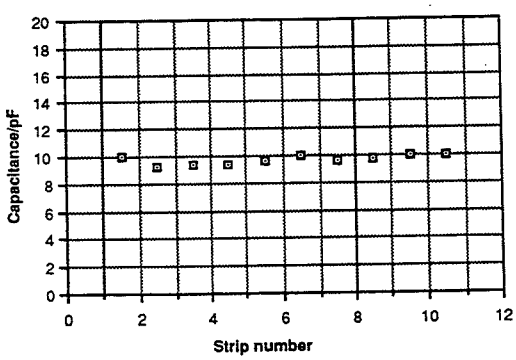

Fig. 7. Interstrip capacitance in detector SD 11-10.

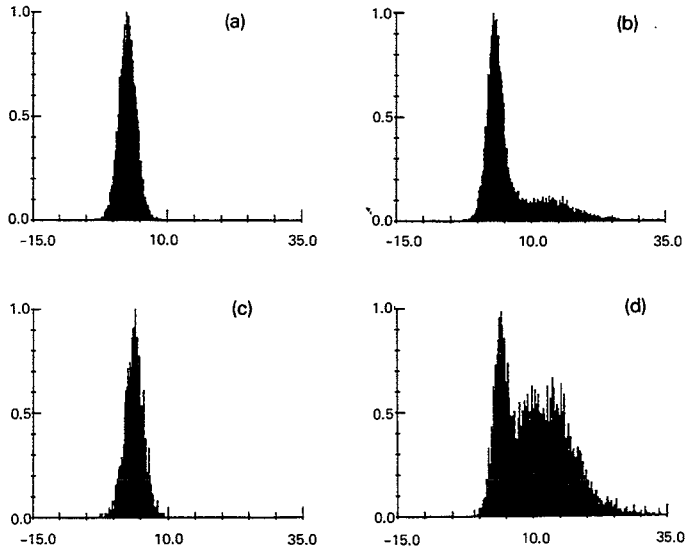

Fig. 8. Pulse height spectra in the beta measurements; (a)–(d) see text.

V, corresponding to a detector depletion depth of 360 μm, was used in the beta measurements.

The cluster algorithm of the analysis software accepted a maximum of two adjacent strips in a cluster, demanding signals above $3\sigma_{noise}$ or $4\sigma_{noise}$ in both strips. One additional strip on both edges was added to the cluster to enable partial cancellation of noise clusters. Due to negative feedback between adjacent amplifier channels, a noise pulse in the charge amplifier output tends to produce a signal of opposite polarity in the neighbouring channels. Total cluster signal is calculated by adding the signals of the individual strips in units of σ_{noise}.

Results from two separate runs are presented in fig. 8. The cluster pulse height spectra of the first run, where noise with continuous trigger was recorded, are shown in fig. 8a and fig. 8c for the two σ_{noise} cuts. In the second run the ^{90}Sr source was presented and a scintillator trigger signal in use. Results from this run, clearly showing the tail of the energy-loss distribution towards higher energies, are presented in fig. 8b and fig 8d. The most probable energy loss corresponds to $14\sigma_{noise}$.

5. Conclusions

A process utilizing ion implantation and annealing at 900 °C has been shown to produce planar silicon detectors of satisfactory electrical properties. Optimum temperature for thermal oxidation steps has been found to be around 1050 °C. Detector manufacturing on 100 mm silicon wafers is possible utilizing well known IC processing steps. Strip detector tests performed with minimum ionizing particles demonstrated a most probable signal pulse height of 14 times the σ_{noise} of any individual readout channel.

Acknowledgements

We would like to thank Mr. Pertti Lehtimäki of Nokia Ltd., Finland, for the precise sawing of the silicon wafers. Mr. Robert Boulter of CERN skillfully bonded our detector to the Microplex readout chips. The data acquisition program used in the beta measurements was for the greater part written by Mr. Hans Dijkstra of CERN. This work was supported by the Finnish Technology Development Center (TEKES).

References

[1] DELPHI Microvertex Detector, Addendum to the Technical Proposal, CERN, DELPHI 86-86 GEN-52 (1986).
[2] J.T. Walker, S. Parker, B. Hyams and S.L. Shapiro, Nucl. Instr. and Meth. 226 (1984) 200.
[3] A. Lang and J.P. Vanuxem, CERN-EP-Electronics note 86-01 (1986).

Publication 2.

Nuclear Instruments and Methods in Physics Research A315 (1992) 502–506
North-Holland

NUCLEAR
INSTRUMENTS
& METHODS
IN PHYSICS
RESEARCH
Section A

Double-sided capacitively coupled silicon strip detectors on a 100mm wafer

Presented by I. Hietanen

R. Brenner, I. Hietanen, J. Lindgren, R. Orava, C. Rönnqvist, T. Schulman, T. Tuuva and M. Voutilainen
Research Institute for High Energy Physics (SEFT), Helsinki, Finland

M. Andersson, K. Leinonen and H. Ronkainen
Technical Research Center of Finland (VTT), Espoo, Finland

Silicon strip detectors with double-sided readout have been designed and processed on 100 mm silicon wafers. Detectors with integrated coupling capacitors and polysilicon bias resistors were tested by static electrical measurements, laser illumination and with tracks from a ^{90}Sr source. Strip separation on the detector n-side has been achieved by the use of capacitively coupled readout electrodes as field-plates. Interstrip resistance of >10 MΩ has been measured in all detector designs. Measurements with ^{90}Sr tracks show S/N = 21 on the detector p-side and S/N = 18 on the n-side.

1. Introduction

In order to meet the requirements of advanced silicon vertex telescopes double-sided silicon strip detectors need to be utilized. Considerable effort has been directed to the R&D of strip detectors enabling both $r\phi$ and z readout in collider experiments [1,2]. This paper describes the characterization of such detectors by the use of static electrical measurement methods, as well as the dynamic tests performed with detectors equipped with LSI readout electronics. Laser spot illumination was first utilized to confirm the operation of both detector sides and the latter test period comprised measurements with minimum ionizing particles from a ^{90}Sr source. Results from these characterization tests are presented.

2. Design

The wafer level layout of the designed detectors is presented in fig. 1. A detailed description of the detector processing at the Technical Research Center of Finland and layouts of the individual strip detectors is presented in an earlier paper [3]. The readout pitch is 50 μm in all detector designs and on both detector faces. Some detectors have intermediate strips on the p-side resulting in strip pitch of 25 μm. These strips are equally biased but do not have readout electrodes above the 200 nm coupling oxide. A common bias line connects all the strips via polysilicon bias resistors.

Double metal processing has been utilized on the detector n-side to design cross-electrodes enabling readout of both detector faces at one edge. This principle has been presented in fig. 2. In detectors with double metal processing (see fig. 1) each cross-elec-

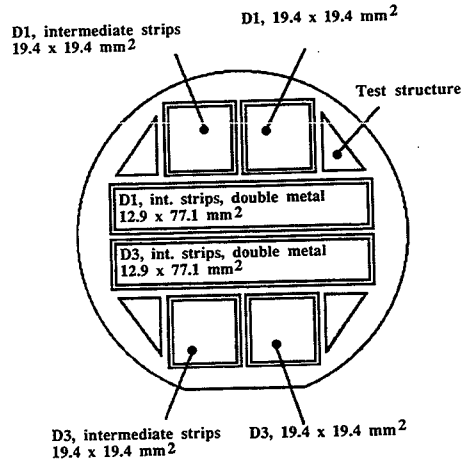

Fig. 1. Wafer layout of the designed double-sided silicon strip detectors.

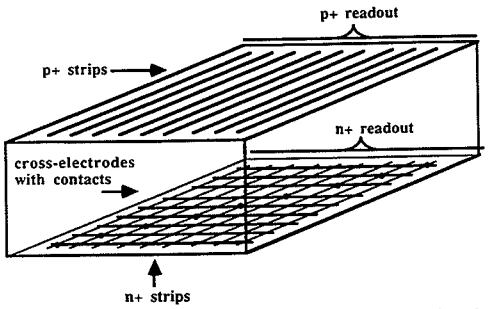

Fig. 2. Principle of cross-electrode readout in the designed double metal double-sided strip detectors.

trode is connected to 6 n-strips hence resulting in detectors with length-to-width ratio of 6:1.

A combination of polysilicon and aluminum strip electrodes was chosen to improve the quality of the coupling oxide and to enable the design of polysilicon field-plate rings around the strip ends on the detector n-side. Due to the well-known effect of accumulation layer formation in the intermediate field-oxide region between the n-strips, a method of isolation of the individual strips is needed. In these detector designs this has been achieved by the use of the capacitively coupled strip electrodes as field-plates. A special problem occurs in the n-strip end region where the outgoing contact to the bias resistor precludes the use of the strip electrode as field-plate in the conventional metal-oxide-strip implant configuration. The polysilicon field-plate rings were designed to prevent the formation of a low-resistivity path between the neighbouring strip ends, fig. 3.

Three different strip widths were studied on all detector faces. The mask widths of the implant strips were 4, 5 and 7 μm on the detector p-side and 4, 7 and 10 μm on the n-side.

3. Static measurements

The depletion characteristics of the processed detectors were studied in C–V measurements of diode

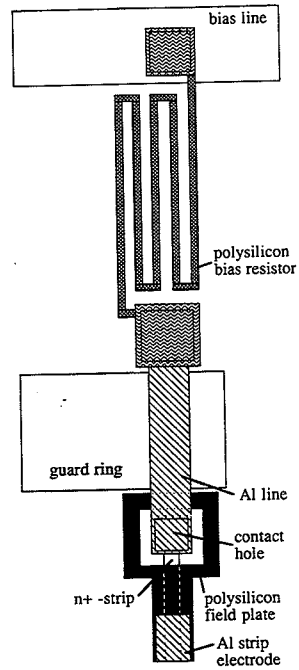

Fig. 3. A detail of the strip end region on the detector n-side.

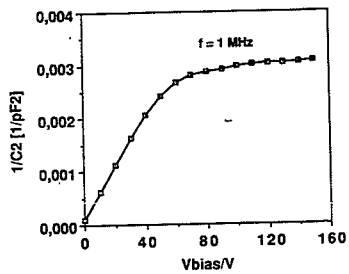

Fig. 4. $1/C^2$ vs V for a 0.5 mm^2 test diode.

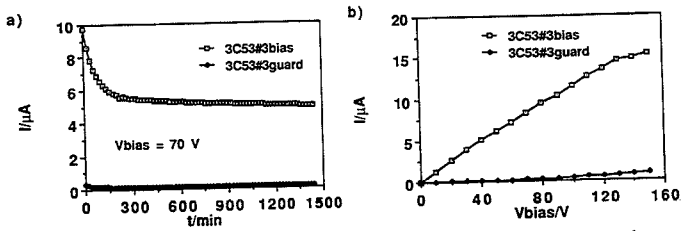

Fig. 5. Leakage current of detector 3C53#3 as a function of time and bias voltage.

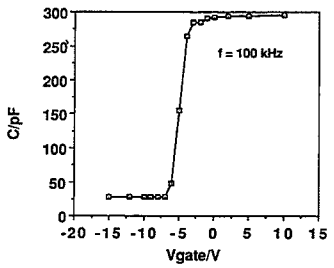

Fig. 6. $C-V$ curve for a 10 mm^2 test bulk capacitor.

test structures. The backplane capacitance of a 0.5 cm^2 test diode is presented in fig. 4. The slope of the $1/C^2$ vs V curve is inversely proportional to the doping level of the depleting silicon material and hence in an ideal measurement the curve should steeply level off when the heavily doped backplane is reached. Total depletion of the detector is clearly achieved at bias voltages > 70 V.

The leakage current of detector 3C53#3 as a function of time and bias voltage is presented in fig. 5. In the long period (24 h) measurement the leakage current drops to a value below that of the short period $I-V$ measurement of fig. 5b. The contribution of the guard-ring current is insignificant compared to the bias line current. A clear correlation between leakage currents of different detector designs and the corresponding proportional areas of non-diode or field oxide regions was observed. This implies that the main contribution to the leakage current is due to surface effects i.e. the oxide charge.

To study the effective oxide charge density the flat band voltage of a 10 mm^2 test bulk capacitor was measured, fig. 6. The flatband voltage shift relative to an ideal bulk capacitor is 5.0 V corresponding to reduced effective oxide charge density of 5.4×10^{11} cm^{-2}.

The design value of polysilicon bias resistors was 3 MΩ on both detector sides. Resistance values in a region of 10 strips on a typical detector are presented in fig. 7. Satisfying match to the design value was achieved on both faces. Variations in bias resistor values over processed wafers were less than $+/-10\%$.

The ohmic separation of the n-side strips was studied as a function of detector bias voltage and readout electrode field-plate voltage. The result from a measurement in the region of narrowest n-strips (mask width 4 μm) is shown in fig. 8. The interstrip resistance was measured indirectly by measuring the resistance between one strip and the bias line. At total strip separation (i.e. when the resistance between neighbouring strips exceeds 100 MΩ) the measurement value should equal that of the polysilicon bias resistor. Total strip separation can be seen (fig. 8) to be achieved at

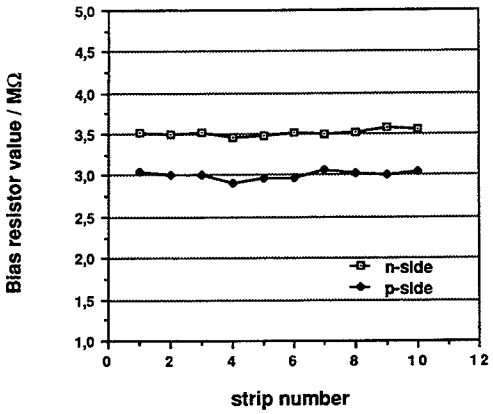

Fig. 7. Polysilicon bias resistor values in a region of 10 strips on a typical detector.

$V_{bias} = 120$ V when the field-plate voltage $V_p > 35$ V. In further studies the resistance between neighbouring n-strip implants and the resistance of an individual strip to the surrounding guard-ring were distinguished. It was observed that a total separation field in the region between neighbouring n-strips was achieved at field-plate voltage between 10 V and 25 V but that the strips were still connected through the low resistance path to the guard-ring. Separation between strips and the guard-ring was achieved when $V_p > 35$ V. Two separate regions of unequal slope of the curves in fig. 8 also indicate this behaviour.

4. Dynamic measurements

The basic operation of the double-sided strip detectors equipped with LSI Microplex readout electronics [4] was studied in measurements with laser spot illumination. A section of the serial analog signal with laser illumination on detector p-side is shown in the oscilloscope plot of fig. 9. The first half of this section

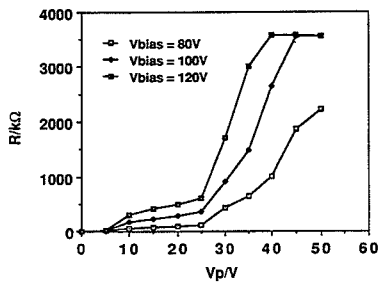

Fig. 8. n-side strip separation measurement.

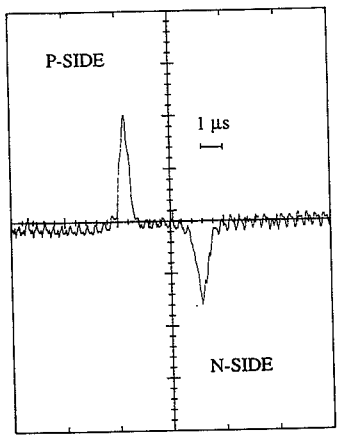

Fig. 9. The serial analog output of a detector in laser spot measurement.

represents 18 strips on detector p-side. In the second half the analog signal of 18 strips on the n-side can be seen, i.e. laser has been positioned in the detector corner region. The charge distribution on the n-side is wider due to slightly lower interstrip resistance and higher interstrip capacitance caused by wider strip implants. This detector does not have cross-electrode readout but similar result was obtained for a cross-readout detector. A bias voltage of 60 V was entirely connected on the detector n-side resulting in field-plate voltage of ≈ 56 V. The readout frequency of the LSI readout chips was 2.3 MHz.

The energy-loss spectra of the detectors were studied in measurements with minimum ionizing particles (MIPs) from a ^{90}Sr source. A measurement setup utilizing scintillator triggers was used [5]. Triggering threshold is set for the high end tail of the β spectrum. The cluster algorithm of the data acquisition software accepts a maximum of two strips in an individual cluster demanding signals above 5rms of the corresponding pedestals in both strips. The distributions of the total cluster signals on the two detector sides are presented in fig. 10. The most probable cluster signal is 69 ADC counts on both sides. The values of the average noise on the p-side and n-side were 3.3 ADC and 3.9 ADC, respectively. This results in signal-to-

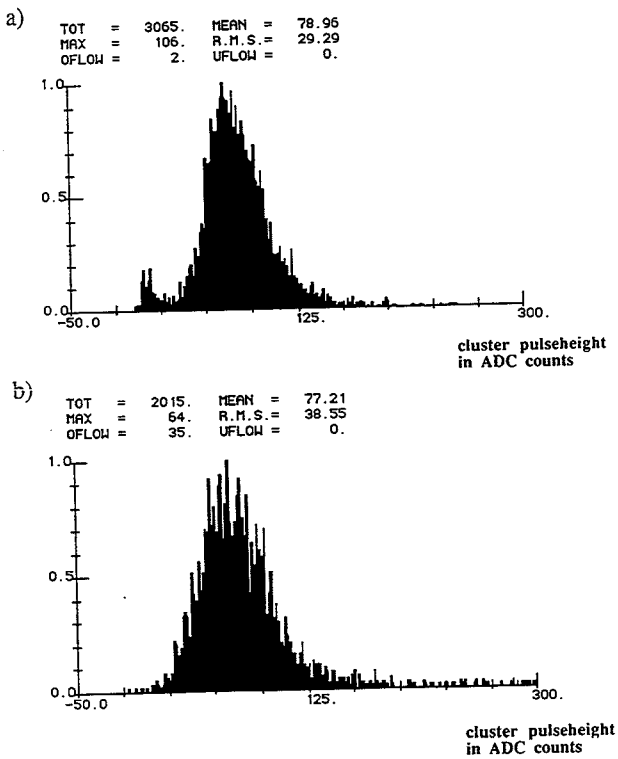

Fig. 10. Cluster pulseheight distribution on detector p-side and n-side.

noise ratios of $S/N_p = 21$ and $S/N_n = 18$. Detector biasing similar to that in the laser measurements was used.

5. Conclusions

Double-sided silicon strip detectors with integrated coupling capacitors and bias resistors have been designed, processed and characterized. Static measurements have shown that the developed detector process produces high quality strip detectors. In the laser measurements signals of equal magnitude were seen on both sides of the detector. This was also observed in tests with minimum ionizing particles from a ^{90}Sr source. Signal-to-noise ratios of $S/N_p = 21$ on the p-side and $S/N_n = 18$ on the n-side were measured. Detectors with cross-electrode readout have equal static parameters and are currently under further testing.

Acknowledgements

We would like to thank Mr. Robert Boulter of CERN for the skillful bonding of our detectors to the Microplex readout chips.

References

[1] B.S. Avset et al., IEEE Trans. Nucl. Sci. NS-37 (1990) 1153.
[2] P. Holl et al., Nucl. Instr. and Meth. A257 (1987) 587.
[3] I. Hietanen et al., University of Helsinki SEFT, Report Series, HU-SEFT-1991-13.
[4] J.T. Walker et al., Nucl. Instr. and Meth. 226 (1984) 200.
[5] I. Hietanen, University of Helsinki SEFT, Report Series, HU-SEFT-1990-2.

Publication 3.

Nuclear Instruments and Methods in Physics Research A326 (1993) 189–197
North-Holland

NUCLEAR
INSTRUMENTS
& METHODS
IN PHYSICS
RESEARCH
Section A

Measurement of the spatial resolution of double-sided double-metal AC-coupled silicon microstrips detectors

R. Brenner, R. Harr [1], A. Rudge, D. Santos [2], J. Straver and P. Weilhammer
CERN, Geneva, Switzerland

A. Czermak, S. Gadomski and M. Turala
Institute of Nuclear Physics, Crakow, Poland

V. Bonvicini, W. Kucewicz [3], S. Masciocchi and G. Vegni
INFN and University of Milan, Italy

A. Peisert
INFN, Padova, Italy

J. Ardelan, A. Hrisoho, K. Troung and F. Couchot
LAL, Orsay, France

C. Colledani, W. Dulinski, D. Husson, A. Lounis, N. Mayet, M. Schaeffer and R. Turchetta
LEPSI, Strasbourg, France

A. Smith
University of Liverpool, UK

R. Apsimon, P. Seller and M. Tyndel
Rutherford Appleton Laboratory, Didcot, Chilton, UK

M. Aalste, I. Hietanen, J. Lindgren, K. Osterberg, R. Orava, C. Ronnqvist, T. Tuuva and M. Voutilainen
SEFT, Helsinki, Finland

The design and first results from double-sided silicon microstrip detectors designed for use in the DELPHI experiment at LEP are presented. The detectors are AC-coupled on both the n- and p-side. A novel readout scheme using a second metal layer has been implemented, allowing the readout of both coordinates on the same edge of the detector. The detectors have been tested in a high energy beam at the CERN SPS. Results on spatial resolution, pulse-height correlation and charge division are presented. The spatial resolution of the n-side has been measured as a function of the beam particle incident angle from 0 to 60°.

1. Introduction

Silicon strip detectors are today strongly demanded as precise vertex detectors in high energy physics experiments. Single-sided detectors, with p strips on n

[1] Visitor from Yale University, New Haven, USA.
[2] Visitor from Pontificia Universidade Catolica de Rio de , Janeiro, Brazil.
[3] Present address: University of Mining and Metallurgy, Crakow, Poland.

doped silicon have been used in high energy experiments for more than ten years [1]. At this time only one experiment (ALEPH at LEP) has used double-sided detectors [2], but in recent years many efforts have been put into the development of these detectors (see for example [3–5]). Double-sided detectors are also serious candidates as high resolution vertex detectors for the future colliders LHC and SSC [6,7].

The main technological problem encountered in the development of double-sided detectors is to create resistively separated strips on the n-side. Fixed positively charges are always present in the oxide at the $Si–SiO_2$ interface. These charges cause an accumulation layer of electrons to form on the silicon side of the interface. In the n-doped bulk silicon, this layer acts as a low resistance conduction path. As a consequence the signal spreads between several strips and the position information is lost.

One way to overcome this problem is to add additional "p-stop" implants between n^+ strips. This is the solution adopted by the ALEPH experiment, and laboratory as well as beam test measurements have proven its effectiveness [2,3].

A few years ago we started developing a new kind of double-sided detector [8]. In order to ensure the ohmic separation between n^+ strips we make use of the MOS structure naturally available in AC-coupled detectors. The aluminium electrode of the MOS coupling capacitors is made larger than the underlying n^+ strips. The potential difference existing between the silicon and the metal electrode serves to control the free carrier silicon charge density below that part of the electrode that extends beyond the n^+ strips. Thus the interstrip resistance can be voltage-controlled [9,10]. The field plate solution allows to keep the design of the n-side as close as possible to that of the p-side. Moreover, due to the absence of additional strips between the n^+ strips, a reduced readout pitch can be designed and thus better spatial resolutions can be achieved.

At collider experiments another practical problem occurs. Strips on the two sides of the detectors end up on two orthogonal edges. In a barrel geometry the readout of Z strips is thus quite clumsy [2]. Mounting the electronics just by the end of the Z strips means adding material in front of the other detectors, thus increasing multiple scattering in the central region of the spectrometer. In our prototypes, we have integrated the fanout on the detector, using a second metal layer. In this way, the readout of both sides is made on the same edge.

2. Design

The design of the double-metal detectors (see fig. 1) follows from that of the AC-coupled single-sided de-

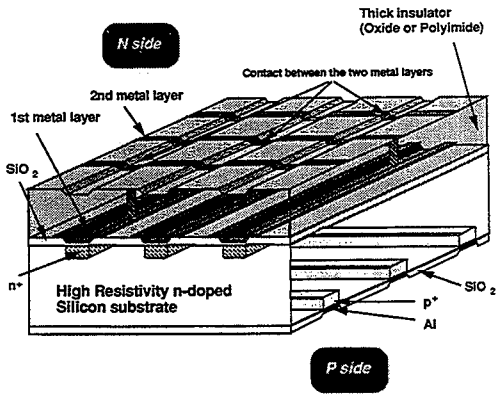

Fig. 1. 3D view of a double-sided detector with double-metal on-chip fanout. Drawing not in scale.

Table 1
Main parameters of the tested prototypes

	VTT	SI
Wafer type		
Resistivity [kΩ cm]	7	11
Orientation	(111)	(111)
Diameter [in.]	4	3
Thickness [μm]	280±10	280±15
Polishing	double sided	double sided
Chip size [mm²]	19×19	19×51
p-side		
diffusion strip width [μm]	5	5
diffusion strip pitch [μm]	25	25
readout pitch [μm]	50	50
readout line width [μm]	8	11
Number of diffused strips	768	769
Number of readout channels	384	384
n-side		
diffusion strip width [μm]	5	5
diffusion strip pitch [μm]	50	35
readout pitch [μm]	50 and 100	35 and 70
1st metal layer width [μm]	18	17
2nd metal layer width [μm]	5	5
2nd metal layer layer pitch [μm]	50	50
Number of diffused strips	384	1441
Number of 1st metal layer strips	384	1441
Number of 2nd metal layer strips (readout channels)	384	384
Double metal layer insulator		
dielectric	SiO_2	polyimide
thickness [μm]	0.5–1.0	2.3
dielectric constant	3.9	3.4

tectors successfully used by the DELPHI collaboration [11]. The main parameters of the two prototypes we tested are shown in table 1. They were manufactured by S.I. (Oslo, Norway) and V.T.T. (Helsinki, Finland). MOS capacitors for AC-coupling are integrated on the detector itself. Each strip is individually biased via a polysilicon resistance connected to an aluminium bias bus. On the n-side, the ohmic separation is obtained by field shaping [8]. The first metal layer lines play the double role of field shaping electrodes and of metal plate of the MOS coupling capacitors. They are larger than the underlying n^+ strips. In order to avoid resistive coupling of the n^+ strips to the guard ring, at one edge of the strip the field electrode ends with a ring under the short metal lines connecting the bias resistors and the n^+ strips. At the other edge it is longer than the n^+ strips. Strips on the second metal layer are orthogonal to the strips in the first metal layer. On one edge they end in four rows of bonding pads. Each line of the first metal layer is connected to a line on the second metal layer. The two metal layers are separated by a thick insulator layer. Since in DELPHI, as well as in other collider experiments, the geometry is such that there are more z strips than $r\phi$ ones, we have tested different multiplexing schemes (see ref. [12] for more details).

3. Electrical measurements

The main electrical parameters of our detectors have been measured in the laboratory prior to the beam tests. Table 2 summarizes the results.

The coupling capacitance has been measured with the quasistatic CV method. The polysilicon resistors and the resistance between adjacent strips on the n-side were measured by applying a high voltage to the diffusion strips on the n-side, and keeping the diffusion lines on the p-side and the readout lines on both sides

Table 2
Main electrical parameters of the tested detectors

Detector parameters	VTT	SI
p-side		
Polysilicon resistance [MΩ]	10	5.5
Coupling capacitance [pF/cm]	10.5	5.9
Interstrip resistance [GΩ]	> 1	> 1
n-side		
Polysilicon resistance [MΩ]	26	9
Coupling capacitance [pF/cm]	19.5	20
Interstrip resistance [GΩ]	> 0.4	> 1
Detector leakage current [μA]	0.3	7.5
Guard ring leakage current [μA]	0.01	350
Depletion voltage [V]	60	25

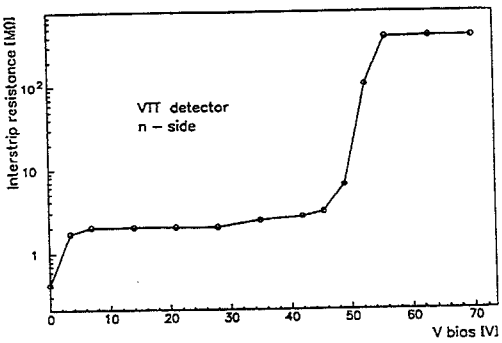

Fig. 2. Interstrip resistance on the n-side of the VTT detector measured as a function of the bias voltage.

at ground potential. The values quoted in table 2 were measured when detectors were fully depleted. Fig. 2 shows the variation of the interstrip resistance with the applied voltage measured on the VTT detector.

The capacitance of a single strip to the adjacent lines was measured in the same conditions on the n-side. This capacitance is a convolution of a direct capacitance between diffusion lines and the capacitance of the metal lines in the two layers. The first term decreases rapidly with the distance between strips [13], while the second has a long range. A simple model which allows calculation of this contribution is proposed in reference [12]. In this model the double metal layer makes each strip couple to all the others, no matter what is the distance between them. This effect can be seen by measuring the capacitance of one strip to its neighbours connected together. Fig. 3 (from ref. [13]) shows this capacitance as a function of the number of adjacent strips measured on the VTT detector.

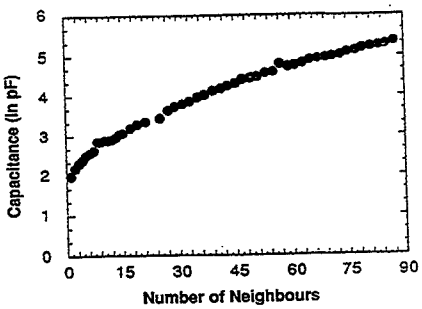

Fig. 3. Capacitance of one strip with respect to the neighbours as a function of the number of neighbours (figure appeared in ref. [13]).

4. Beam test setup

Tests were performed in the West Area at the SPS, CERN. During most of the data taking period, we used a pion beam with a momentum of 70 GeV/c. At this energy and for our setup, the multiple scattering is not negligible. This point is taken into account in the off-line analysis (see section 5).

Reference detectors are of the same type as the ones used in the DELPHI Microvertex. They are single-sided, AC-coupled microstrip detectors, with integrated capacitors. Their size is 32×60 mm. 1280 p^+ strips at a pitch of 25 μm are diffused on the detector. Each strip is individually biased via an integrated polysilicon resistance connected to a common metal bias bus line. Readout is done every second strip. The reference detectors are equipped with NMOS Microplex chips [14]. There are eight reference detectors, four (x detectors) measure points in the xz plane and four (y detectors) measure points in the orthogonal yz plane (fig. 4).

The double-sided detectors under test are equipped with CMOS MX6 VLSI readout circuits [12].

Each silicon detector is mounted on a precisely machined mechanical support which acts also as the heat sink. The supports are mounted on an optical bench that is installed on a marble table. The double-sided detector is mounted on a pivoting support. This support can rotate around a vertical axis by ±180°.

Multiplexed differential analog signals coming from the silicon detectors are fed into CAMAC [15] and VME [16] Sirocco units. A total of six Sirocco units were used.

The trigger is provided by a set of upstream and downstream scintillators mounted on the optical bench. Data acquisition software [16] runs on a VME/OS9 system. Raw data are written to Exabyte cassettes, each event accounting for 16 KB.

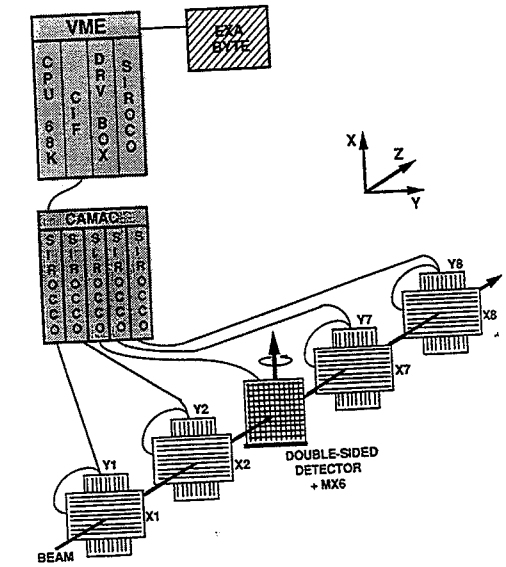

Fig. 4. Beam test setup.

5. Off-line analysis

For each event and for each channel, the pulse-height and the noise are calculated off-line. Digital filtering techniques are used for a continuous update of pedestal and noise [17]; common mode shift of the base line is calculated for each event. The techniques of cluster reconstruction and the algorithms for calculating the position of the clusters are described below.

A weighted least-squares fit to a straight line is used to reconstruct tracks in both projections xz and yz separately. Only tracks defined by the whole set of the eight reference detectors are accepted. A χ^2 cut de-

Table 3
Position resolution for the VTT p-side as a function of the angle. As in the other tables we use the following definitions (see text for details). Cluster finding algorithm: N stands for "normal" and I for "inclined tracks" cluster finding algorithm. Position finding algorithm: ETA stands for "eta", LIN for "linear", DHT for "digital head–tail", AHT for "analog head–tail" with ω defined by eq. (10), AHT (no min) for "analog head–tail" with ω defined by eq. (9)

Angle [degrees]	Cluster finding algorithm	Position finding algorithm	σ_{FIT} [μm]	Error on impact point [μm]	Spatial resolution [μm]
0	N	ETA	7.1±0.3	6.0±0.3	3.8±0.6
5	N	ETA	6.9±0.3	6.1±0.3	3.2±0.9
10	N	ETA	7.1±0.3	6.1±0.3	3.6±0.6
20	N	ETA	7.3±0.3	6.1±0.3	3.7±0.6
30	N	ETA	7.2±0.3	6.2±0.3	3.7±0.6
40	N	ETA	7.5±0.2	6.0±0.3	4.5±0.6
50	N	ETA	8.1±0.3	6.2±0.3	5.2±0.4

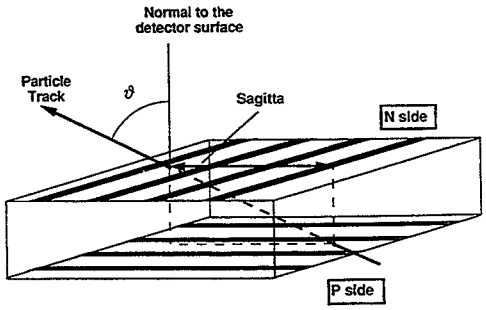

Fig. 5. Inclined track geometry.

fines good track projections. Events for which one and only one good track is found in both projections are accepted. Multiple scattering is taken into account when calculating the error on the reconstructed impact point, using the method described in ref. [18]. In our geometry the error on the reconstructed impact point is about 1.5 μm larger than the same quantity calculated in the absence of multiple scattering (see tables 3 and 4).

5.1. Signal spread for inclined tracks

The details of the data analysis depend on the geometry of the tracks (fig. 5). In our setup, n-side strips are vertical, while p-side strips are horizontal. This means the n-side measures a point in the *yz* projection while the p-side gives a point in the *xz* projection. Two angles are needed to define the inclination of the tracks in space: we can choose the angles that the track forms with the normal to the detector surface in the two projections *xz* and *yz*. We call them ϑ_x and ϑ_y respectively. In our setup ϑ_x is always zero and we can only vary ϑ_y. In the following we will indicate ϑ_y as ϑ. It is also important to consider the projection of the path of the particles in the silicon onto the two planes *xz* and *yz*. In our geometry the first one is always zero, while the second one, that we call sagitta, is given by

$$\text{sagitta} = \text{thickness} \times \tan \vartheta . \tag{1}$$

For sufficiently large angles ϑ, the signal spreads over several strips where the mean number N_{cl} of strips per cluster is roughly given by

$$N_{cl} = \frac{\text{sagitta}}{\text{pitch}} = \frac{\text{thickness}}{\text{pitch}} \times \tan \vartheta . \tag{2}$$

The length of the path of the particle in silicon is proportional to $1/\cos(\vartheta)$. Since the most probable energy loss is roughly proportional to the length of this path [19], we can write

$$S(\vartheta) = \frac{S(0)}{\cos \vartheta} , \tag{3}$$

where $S(\vartheta)$ is the cluster signal measured at an angle ϑ.

Taking into account eqs. (2) and (3), we can say that for sufficiently large ϑ, the average signal collected by one strip (on the n-side only, in our geometry) is given by

$$S_\vartheta = \frac{S(\vartheta)}{N_{cl}} = S(0) \frac{\text{pitch}}{\text{thickness}} \frac{1}{\sin \vartheta} . \tag{4}$$

Neglecting Landau as well as noise fluctuations, we observe that the signal on one strip is exactly S_ϑ on all the strip in the cluster but the first ("tail") and the last ("head") one.

5.2. Cluster finding algorithms

On the basis of the previous considerations we have considered two algorithms for cluster reconstruction. The two algorithms differ on how the selection of the strips in the cluster is done.

Table 4
Position resolution for the VTT n-side as a function of the angle. See table 3 for explanation of abbreviations

Angle [degrees]	Cluster finding algorithm	Position finding algorithm	σ_{FIT} [μm]	Error on impact point [μm]	Spatial resolution [μm]
0	N	ETA	8.8±0.4	5.8±0.2	6.6±0.6
5	N	LIN	8.6±1.0	5.8±0.3	6.3±1.4
10	N	LIN	8.5±0.3	6.1±0.3	5.9±0.5
20	I	AHT	10.3±0.8	6.4±0.3	8.1±1.0
30	I	AHT	14.9±0.9	7.3±0.4	13.0±1.1
40	I	AHT	16.8±0.9	7.8±0.4	14.9±1.0
50	I	AHT	20.9±0.5	9.9±0.5	18.4±1.2

In the first method ("normal" cluster finding algorithm), we look first for a strip (the "central" strip) which has a signal-over-noise ratio S/N higher than a given threshold T_1, and then we add in the cluster all the neighbouring strips for which is $S/N > T_2$.

In the second method ("inclined track" cluster finding algorithm), we include in the cluster all the strip with $S/N > T_1'$, and then we add also the strips next to the two edge strips if their S/N is higher than T_2'.

Once we have defined a cluster, it must pass the following controls.

(a) The signal-over-noise ratio for the cluster must be higher than T_1^{cl}.
(b) The signal of the cluster must be higher than T_2^{cl} and lower than T_3^{cl} ADC counts.
(c) The number of strips in the cluster must be higher than T_4^{cl} and lower than T_5^{cl}.

5.3. Position finding algorithms

For computing the impact point position of the particle passing through the detector, several algorithms can be used. The choice depends on the detector parameters (pitch, bias voltage, thickness) and on the geometry of the track. For non-inclined tracks, most of the charge is collected by two strips in a non linear way [20]: a nonlinear interpolating algorithm can be used [21,22]. This algorithm ("eta" algorithm) is based on the variable η defined as

$$\eta = \frac{PH_R}{PH_R + PH_L}, \tag{5}$$

where PH_R (PH_L) is the pulse-height on the strip on the right (left). The experimental distribution of this variable measured for non-inclined tracks is shown in fig. 6.

For an angle ϑ such that the sagitta is smaller than the pitch, the charge spreads over two strips in an almost linear way. The position is assumed to be directly proportional to the variable η ("linear" algorithm).

For inclined tracks, the first approach is to use the geometrical mean of the positions of the "head" and of "tail" strips of the cluster. The position is then given by ("digital head-tail" algorithm)

$$X_{DHT} = (x_h + x_t)/2. \tag{6}$$

From geometrical considerations (fig. 7), the impact point position is given by

$$X_{IMP} = \frac{x_h + x_t}{2} + \frac{p_h - p_t}{2} = X_{DHT} + \frac{p_h - p_t}{2}. \tag{7}$$

The energy loss is roughly proportional to the path of the particle in silicon, so we can write ('analog head–tail' algorithm)

$$X_{AHT} = (x_h + x_t)/2 + \omega, \tag{8}$$

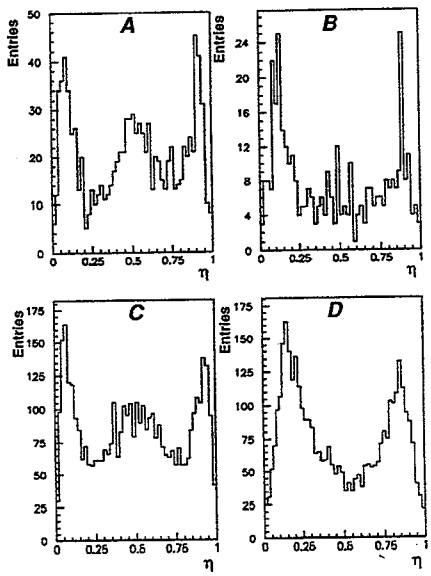

Fig. 6. Distribution of the η variable for non-inclined tracks. (a) VTT detector p-side; (b) VTT detector n-side; (c) SI detector p-side; (d) SI detector n-side.

where

$$\omega = (S_h - S_t)/2S_\vartheta \tag{9}$$

and S_h and S_t are the pulse-heights measured on the head and on the tail strip of the cluster, respectively.

Since Landau fluctuations are more likely to push the energy loss towards values higher than the most probable one, we can hope to have a better position definition if we define ω as

$$\omega = \frac{\min(S_h, S_\vartheta) - \min(S_t, S_\vartheta)}{2S_\vartheta}. \tag{10}$$

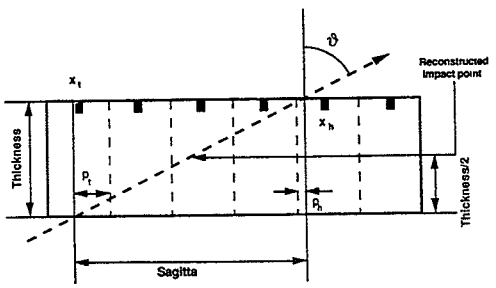

Fig. 7. Reconstructed impact point and position finding algorithm for inclined tracks.

6. Beam test results

Data have been taking at eight different angles ϑ (0, 5, 10, 20, 30, 40, 50 and 60°) with the VTT detector and at 4 ϑ different angles (0, 20, 40 and 60°) with the SI detector. In this paper we will present results from a subset of these runs since data analysis is not yet finished. Due to the lack of time, we could not do an optimal choice of the analysis parameters. Because of the low statistics, only results on n-side regions with a pitch of 50 and 35 μm for the VTT and SI prototypes respectively are considered.

6.1. Landau distribution, noise, Landau correlation, charge division, efficiency

Fig. 8 shows the pulse-height distributions for our prototypes and for non inclined tracks ($\vartheta = 0°$). The differences in S/N ratios are due to the different design of the detectors. Efficiency has been measured for non-inclined tracks and found consistent with 100% on both sides and for both prototypes.

Correlation of the pulse-heights measured on the two sides of a double-sided detector is important in order to reduce ambiguities in the case of multi-hit events. For all the different runs we analysed, we did not find any significant difference between the pulse-heights measured on the two sides. Fig. 9 shows the

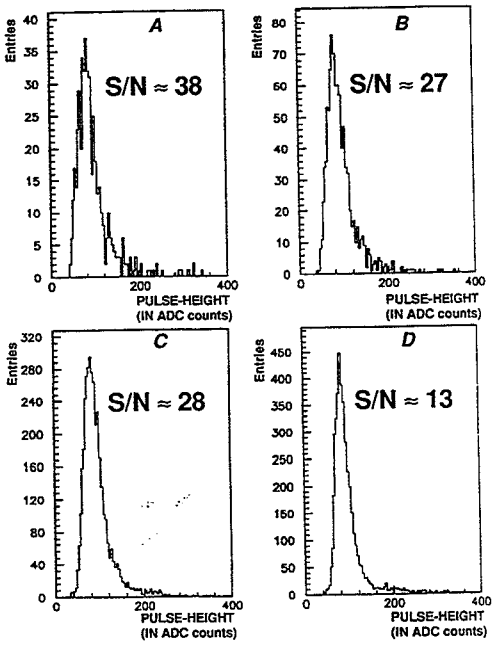

Fig. 8. Pulse-height distributions for non-inclined tracks. (a) VTT detector p-side; (b) VTT detector n-side; (c) SI detector p-side; (d) SI detector n-side. Signal-over-noise ratios S/N are also indicated.

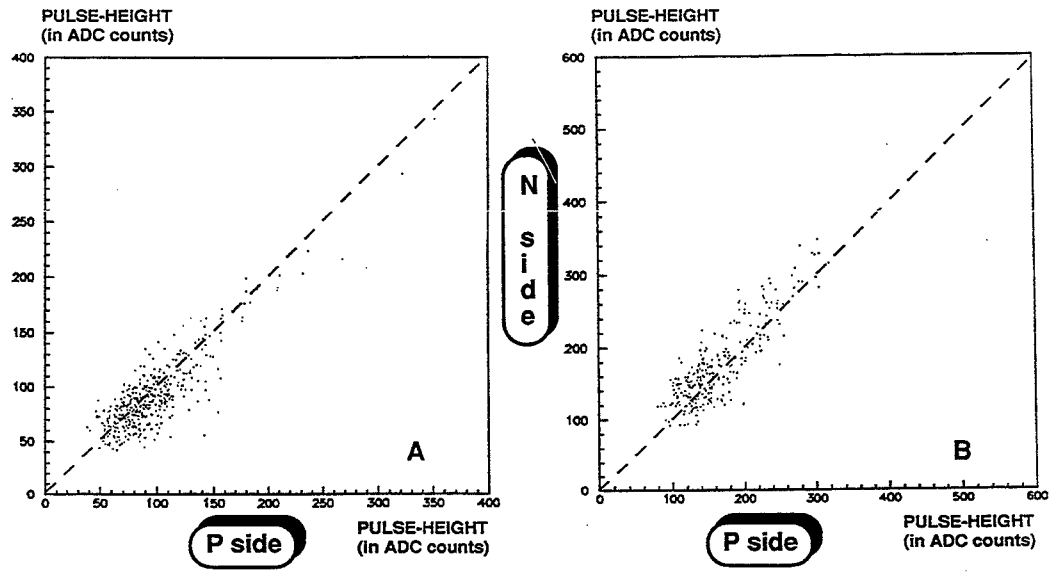

Fig. 9. Landau correlation measured at two different track angle with the VTT detector. (a) $\vartheta = 0°$; (b) $\vartheta = 50°$. Each point in the plots represents one event.

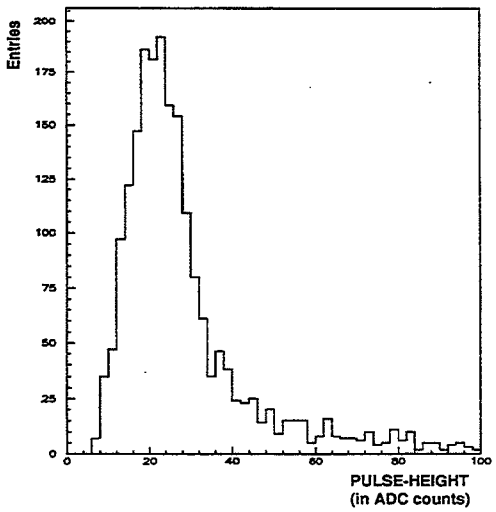

Fig. 10. VTT detector n-side. Data taken at 50°. Pulse-height distributions of all the strips in the cluster except the head and the tail. The shape of the distribution is determined by fluctuations in energy loss.

pulse-height correlation for data taken at two different angles for the VTT detector.

The distribution of the charge between the strips in the cluster has been studied (fig. 6). For small angle ϑ, we consider the distribution of the variable η. On the n-side of both SI and VTT detectors, the readout is done at every strip and the distribution of the variable η shows the characteristic two-peaks structure. On the p-side, where the readout is done every second strip, this distribution has a three-peaks structure, where the central peak is the mark of the intermediate strip. In this case, the charge division between the two readout strips is almost linear.

For larger angles, we expect the pulse-height distribution of all the strips in the cluster but head and the tail to have the Landau shape. This is confirmed by the experimental data (fig. 10). The position of the peak is found to be consistent with that of the distribution shown in fig. 8b.

6.2. Spatial resolution

The results on the spatial resolution are shown in tables 3 to 6 and fig. 11. The resolution on the p-side remains almost constant with the angle ϑ (table 3) the η-algorithm is used at each angle. For the n-side different algorithms are used (table 4). For sufficiently high angle, the analog head–tail with ω defined by eq. (10) gives the best results (table 5). Resolution of 18.4 μm has been obtained for 50° tracks. A minimum in the spatial resolution seems to appear at around 5–10° but the errors on these points are quite large due to statistics. Increasing the angle the spatial resolution worsens but is better than 20 μm at 50°.

7. Conclusions

We have designed and successfully tested a double-sided detector with field plate ohmic separation and on-chip fan-out, processed on a second metal layer on the n-side. One of the prototype features 35 μm pitch on the n-side, that is the smallest pitch ever tried for n^+ strips on n substrate.

Spatial resolution has been measured in a high energy beam. For non-inclined tracks, we have mea-

Table 5
Position resolution for the VTT n-side as a function of the angle and for different algorithms. See table 3 for explanation of abbreviations

Angle	AHT	AHT (no min)	DHT
30	13.0 ± 1.1	16.2 ± 1.3	18.0 ± 1.1
50	18.4 ± 2.1	20.6 ± 1.4	19.9 ± 1.3

Table 6
Position resolution for the SI detector and non-inclined tracks. See table 3 for explanation of abbreviations

Detector	Cluster finding algorithm	Position finding algorithm	σ_{FIT} [μm]	Error on impact point [μm]	Spatial resolution [μm]
SI p-side	N	ETA	6.4 ± 0.1	5.7 ± 0.3	2.9 ± 0.6
SI n-side	N	ETA	8.6 ± 0.1	5.6 ± 0.3	6.5 ± 0.3

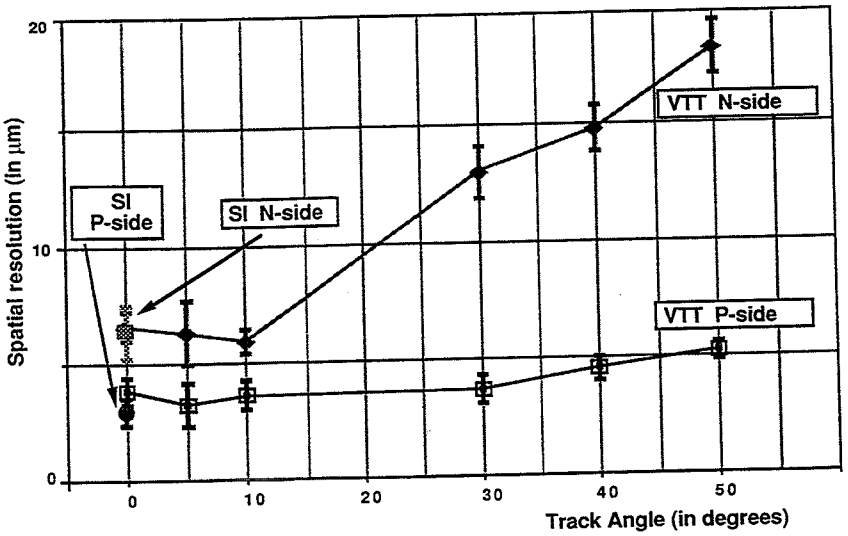

Fig. 11. Summary of the beam test measurements (see also table 3 to 6). As explained in the text, the angle ϑ has a different meaning if we consider the p- or the n-side because of the geometry of our setup.

sured a spatial resolution of 2.9 μm on the p-side. To our knowledge this is the best result ever obtained with 50 μm readout pitch detectors, and this shows the importance of an intermediate strip for charge interpolation. On the n-side we measured 6.5 μm.

We also measured the spatial resolution as a function of the angle of inclination of the tracks on the n-side. At 50° we obtained a resolution of 18.4 μm.

These results prove the effectiveness of our design. Double-sided detectors with double-metal fan-out are being currently processed and will be used by the DELPHI experiment.

Acknowledgements

We would like to thank B.S. Avset and L. Evensen from S.I. and K. Leinonen and S. Eranen from V.T.T. for their close collaboration.

References

[1] J. Kemmer, Nucl. Instr. and Meth. 169 (1980) 489.
[2] G. Batignani et al., these Proceedings (6th European Symp. on Semiconductor Detectors, Milan, Italy, 1992), Nucl. Instr. and Meth. A326 (1993) 183.
[3] G. Batignani et al., Nucl. Instr. and Meth. A310 (1991) 165.
[4] K. Saito et al., these Proceedings (6th European Symp. on Semiconductor Detectors, Milan, Italy, 1992), Nucl. Instr. and Meth. A326 (1993) 204.
[5] L. Hubbeling et al., Nucl. Instr. and Meth. A310 (1991) 197.
[6] H. Borner et al., CERN/DRDC 91-10, DRDC/P26, 7 March, 1991, Geneva.
[7] J. Hylen et al., Nucl. Instr. and Meth. A310 (1991) 497.
[8] B.S. Avset et al., IEEE Trans. on Nucl. Sci. 37, 3 (1990) 1153.
[9] D. Husson, Nucl. Instr. and Meth. A320 (1992) 201.
[10] R. Brenner et al., these Proceedings (6th European Symp. on Semiconductor Detectors, Milan, Italy, 1992), Nucl. Instr. and Meth. A326 (1993) 198.
[11] M. Caccia et al., Nucl. Instr. and Meth. A260 (1987) 124.
[12] R. Brenner et al., Presented at 6th European Symp. on Semiconductor Detectors, Milan, Italy, 1992.
[13] A. Peisert, in: Instrumentation in High Energy Physics. ed. F. Sauli (World Scientific, Singapore, 1992).
[14] S. Walker et al., Nucl. Instr. and Meth. 226 (1984) 200.
[15] A. Lang and J.P. Vanuxem, CERN-EP-electronics note 86-01.
[16] C. Colledani et al., CRN-LEPSI note, to be published.
[17] V. Chabaud et al., Nucl. Instr. and Meth. A292 (1990) 75.
[18] G. Lutz, Nucl. Instr. and Meth. A273 (1988) 349.
[19] Particle Properties Data Booklet, April 1990.
[20] E. Belau et al., Nucl. Instr. and Meth. 214 (1983) 253.
[21] R. Turchetta, CRN/HE 91-07, Ph.D. Thesis, N. d'ordre 1019, April 29th, 1991, Strasbourg.
[22] P. Weilhammer, private communication.

Publication 4.

Nuclear Instruments and Methods in Physics Research A328 (1993) 447–471
North-Holland

NUCLEAR
INSTRUMENTS
& METHODS
IN PHYSICS
RESEARCH
Section A

The DELPHI Microvertex detector

N. Bingefors, H. Borner, R. Boulter, M. Caccia, V. Chabaud, H. Dijkstra, P. Eerola, E. Gross, R. Horisberger, L. Hubbeling, B. Hyams, M. Karlsson, G. Maehlum, K. Ratz, I. Roditi, J. Straver, W. Trischuk and P. Weilhammer
CERN, CH-1211 Geneva 23, Switzerland

Y. Dufour
College de France, Lab. de Physique Corpusculaire, Paris, France

P. Brückman, P. Jałocha, P. Kapusta, M. Turała and A. Zalewska
Institute of Nuclear Physics, Cracow, Poland

J. Lindgren, R. Orava, K. Österberg, C. Ronnqvist, H. Saarikko, J.P. Saarikko and T. Tuuva
Research Inst. for High Energy Physics, Helsinki, Finland

B. d'Almagne, P. Bambade, F. Couchot and F. Fulda
Laboratoire de l'Accélérateur Linéaire, Orsay, France

A. Amery, P.S.L. Booth, A.R. Campion, R. McNulty and N.A. Smith
Univ. of Liverpool, Dept. of Physics, Liverpool, UK

A. Andreazza, M. Battaglia, P. Biffi, V. Bonvicini, W. Kucewicz, C. Meroni, N. Redaelli, A. Stocchi, C. Troncon and G. Vegni
Univ. di Milano, Dipt. di Fisica, Milano, Italy

P. Dauncey
Univ. of Oxford, Dept. of Nuclear Physics, Oxford, UK

M. Mazzucato, M. Pegoraro and A. Peisert
Univ. di Padova, Dipt. di Fisica, Padova, Italy

M. Baubillier, J. Chauveau, W. Da Silva, J.F. Genat and F. Rossel
LPNHE, Univ. Paris VI-VII, Paris, France

T. Adye, R. Apsimon, J. Bizell, L. Denton, G.E. Kalmus, J. Lidbury, P. Seller and M. Tyndel
Rutherford Appleton Lab., Chilton, UK

W. Dulinski, D. Husson, A. Lounis, M. Schaeffer and R. Turchetta
LEPSI, IN2P3 / ULP, Strasbourg, France

R. Brenner and E. Sundell
Åbo Akademi, Dept. of Physics, Turku, Finland

Received 16 October 1992

The DELPHI Microvertex detector, which has been in operation since the start of the 1990 LEP run, consists of three layers of silicon microstrip detectors at average radii of 6.3, 9.0 and 11.0 cm. The 73728 readout strips, oriented along the beam, have a total active area of 0.42 m^2. The strip pitch is 25 μm and every other strip is read out by low power charge amplifiers, giving a signal to noise ratio of 15:1 for minimum ionizing particles. On-line zero suppression results in an average data size of 4 kbyte for Z^0 events. After a mechanical survey and an alignment with tracks, the impact parameter uncertainty as determined from hadronic Z^0 decays is well described by $\sqrt{(69/p_t)^2+24^2}$ μm, with p_t in GeV/c. For the 45 GeV/c tracks from $Z^0 \to \mu^+\mu^-$ decays we find an uncertainty of 21 μm for the impact parameter, which corresponds to a precision of 8 μm per point. The stability during the run is monitored using light spots and capacitive probes. An analysis of tracks through sector overlaps provides an additional check of the stability. The same analysis also results in a value of 6 μm for the intrinsic precision of the detector.

1. Introduction

The aim of a vertex detector is to provide high precision measurements of the position of particles close to the primary collision point, allowing accurate track reconstruction and precise extrapolations to the interaction region. This facilitates the reconstruction of the decay chain through the identification of primary and secondary vertices.

In this article the Microvertex detector, a vertex detector constructed for the DELPHI experiment, is described. DELPHI is one of the four multi-purpose detectors installed at the LEP accelerator at CERN. It is used to study e^+e^- interactions at energies close to the mass of the Z^0 boson. More information about the DELPHI detector can be found elsewhere [1].

The Microvertex detector provides high precision measurements in the plane transverse to the beam [#1]. A part of the detector was tested during the start-up of LEP in 1989. A two layered detector was completed and installed for the data taking in 1990. It was upgraded to the present three layered detector with a smaller beam pipe for the 1991 data taking period. About 130000 hadronic Z^0 events were collected by DELPHI in 1990 and 280000 in 1991.

1.1. Physics motivation

Since the first observations, in the 1970-ties, of the τ lepton, the J/ψ meson containing the c quark and the Υ meson containing the b quark, physics related to these partons has been of special interest.

LEP is very well suited to explore this field. Z^0s are produced with a high cross section and decay into $b\bar{b}$ in 15.4% of events, into $c\bar{c}$ in 11.9% and into $\tau^+\tau^-$ in 3.3%. In addition, the combinatorial background is relatively low compared to that found in hadronic heavy quark production.

The τ lepton and hadrons containing heavy quarks have short lifetimes. Typical values measured are $(2\text{–}15) \times 10^{-13}$ s. At LEP energies this corresponds to distances between the primary interaction vertex and the decay vertex of heavy hadrons of a few mm.

The presence of one or more decay vertices close to the interaction point is by itself a tag for the decays of Z^0 to heavy quarks. The vertex detector is used to recognize such topologies. It provides precise measurements of the tracks position and direction immediately outside the beam pipe of the collider. Using these values the trajectory of a track can be extrapolated back to the primary interaction point allowing the reconstruction of both primary and secondary vertices. It is illustrated in fig. 1a which shows an event display of a candidate for the decay $Z^0 \to b\bar{b}$. A magnification of the area around the interaction region is displayed in fig. 1b showing the ability of the Microvertex detector to clearly separate primary and secondary vertices.

The high precision measurements of the track parameters allow an exploration of the spectroscopy, lifetimes and decay modes of the heavy hadrons. In addition to secondary vertex identification and reconstruction the precision on the effective mass determination is improved due to the improved momentum resolution. Both these effects considerably reduce the combinatorial background and improve the signal/background.

Results already obtained from the analysis of data taken in 1990 and 1991 highlight some of the advantages outlined above, and confirm the usefulness of the Microvertex detector for the DELPHI experiment. Physics measurements made using the 1990 data which depend crucially on the presence of the Microvertex detector are the measurement of the lifetime of the τ lepton [2] and of the average lifetime of B hadrons [3]. The analysis of the data taken in 1991 with the upgraded Microvertex detector is still being performed but already some results have been obtained. Evidence for B_S^0 production [4], and a clear D meson signal accompanied by a high p_t lepton has been obtained by studying the invariant mass of $Kn\pi$, $n = 1, 2, 3$, systems in hadronic events [5]. The importance of the Microvertex detector in this latter analysis is in suppressing the background by demanding a good decay

[#1] R, ϕ, z define a cylindrical co-ordinate system, $+z$ being coincident with the electron beam, R, ϕ defined in the transverse plane.

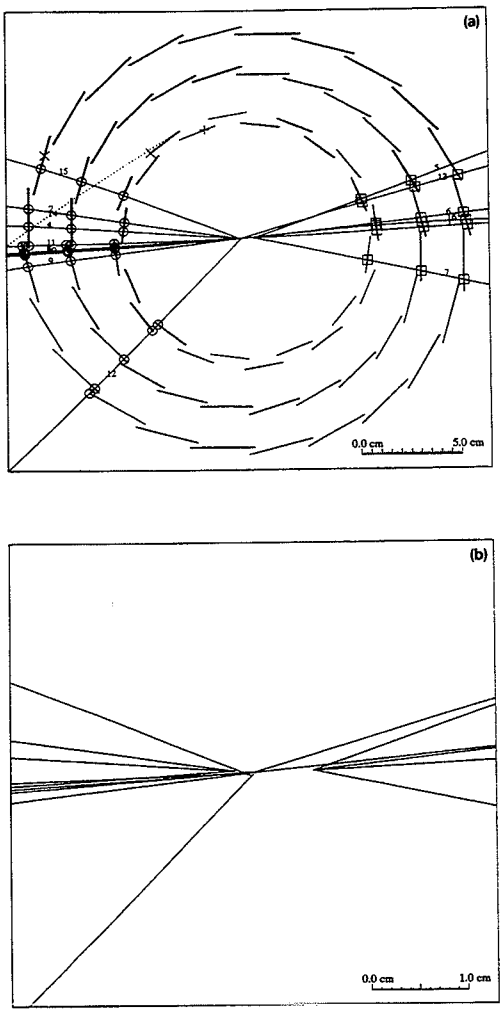

Fig. 1. Event display for a $Z^0 \to b\bar{b}$ candidate. Run 21582, event 6995.

vertex separated from the primary vertex, and in improving the momentum resolution.

1.2. Design optimization and constraints

In the design of the Microvertex detector, the quantity of most interest is the accurate extrapolation of a given track to the vertex region and subsequently the precise reconstruction of vertices. The impact parameter is defined as the distance of closest approach of a given track to the primary interaction point [#2]. For tracks coming from the primary vertex it should be zero, but resolution effects smear this. These are of two types. Firstly multiple scattering in any material in front of the measured points limits the resolution especially for low momentum tracks. Secondly, any uncertainties in the track reconstruction due to the intrinsic resolution of the sub detectors used in the track fit [#3] limit the precision especially at higher momentum. The impact parameter resolution is often parameterized as the quadratic sum of these two terms

$$\sigma_{IP}^2 = \sigma_{asympt}^2 + \left(\frac{\sigma_{ms}}{p_t}\right)^2, \quad (1)$$

with transverse momentum p_t measured in GeV/c.

The optimization of the Microvertex detector is achieved by minimizing the material in front of the detector, by measuring the first point precisely, as close as possible to the interaction region, and finally by having adequate angular resolution [6]. In practice this demands the use of silicon microstrip detectors with an intrinsic measurement precision of better than 5 μm.

The design of the 1990 Microvertex detector of DELPHI was constrained by the small amount of space available between the aluminium LEP beam pipe of inner radius 7.8 cm and thickness 1.2 mm. and the DELPHI Inner detector.

With the two layers of the Microvertex detector placed at radii of 9 and 11 cm, σ_{asympt} was measured using di-muon events [2] to be 80 μm, while the multiple scattering term was $120/p_t$. For the 1991 running, a new beam pipe made of beryllium was installed with an inner radius of 5.3 cm and thickness 1.45 mm. This allowed a third layer to be added to the Microvertex detector at an average radius of 6.3 cm, thus reducing σ_{asympt} to 24 μm and the multiple scattering term to $69/p_t$ μm.

1.3. General layout

A brief overview of the DELPHI Microvertex detector is given here as an introduction to the detailed description of all its components and performances

[#2] It is signed according to the geometric convention, that is, it is given a plus or minus sign depending on whether an observer standing at the interaction point facing the direction of the track, sees it on her right or left.

[#3] The tracking detectors at DELPHI consist of the Microvertex detector between radii of 6 and 11 cm, the Inner detector between 12 and 38 cm, the Time Projection Chamber between 39 cm and 120 cm and the Outer detector between 200 and 205 cm. Further details can be found in ref. [1].

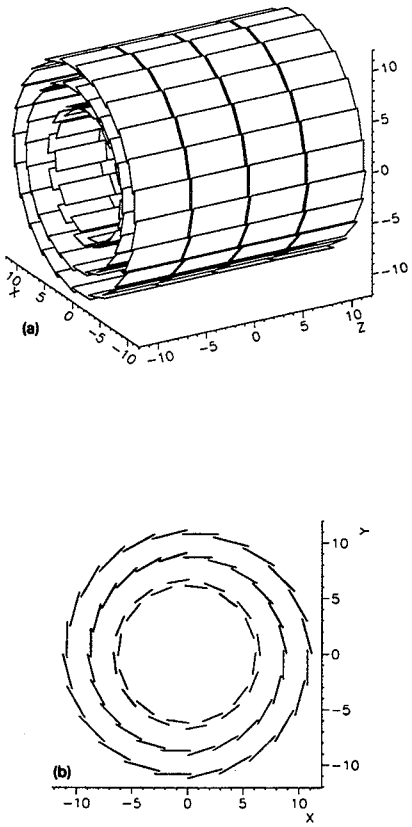

Fig. 2. Schematic layout of the DELPHI Microvertex detector: (a) Perspective view. (b) Projection on the plane transverse to the beam.

given in the following sections. A schematic perspective view of the detector is presented in fig. 2a and in fig. 2b is shown its projection in the plane transverse to the beam.

Three concentric shells of silicon microstrip detectors at average radii of 6.3, 9 and 11 cm cover the central region of the DELPHI detector, and surround the beam pipe. The two shells at the larger radii, called the Inner and the Outer, had been completed for the LEP running period in 1990 while that at the smallest radius, called the Closer, was added for the running in 1991. The Closer shell is 22 cm long, while the Inner and the Outer are 24 cm long.

Each shell consists of 24 modules with about 10% overlap in ϕ between the modules (see fig. 2). Each module consists of 4 silicon detectors, with strips parallel to the beam. Detector pairs are wire-bonded in series and read out at either end.

The silicon microstrip detectors with integrated coupling capacitors and biasing resistors are novel and were developed specifically for DELPHI [7]. They are 285 μm thick and have a diode pitch of 25 μm with a readout pitch of 50 μm. The number of read-out strips totals 73 728. A detailed description of the detectors performance and of the applied acceptance criteria is given in section 2.

The VLSI readout electronics produced in 3 μm CMOS, contain 128 analog channels with serial readout. The readout chips are bonded channel by channel to the strips at both ends of the detector modules which are stiffened by a carbon-fibre support. The components of the modules and their assembly are described in section 3.

The outer ends of each module are mounted on to two aluminium semi-circular rings which surround the beam pipe. The mechanical structure is water cooled to guarantee good thermal stability. Before installation the relative alignment of the modules was surveyed using a three-dimensional measuring machine, to a global accuracy of about 20 μm. The whole detector can be slid into position around the interaction region on rails fixed to the Inner detector. The half-shells assembly, survey, electronics and detector insertion are described in section 4.

The outputs of six chips from the Closer shell, or of four chips from the Inner shell and five chips from the Outer shell are multiplexed together in electronics mounted nearby, giving 768 or 1152 channels per readout line. These signals are analyzed on-line by DSP processors in dedicated Fastbus modules. Section 5 contains the description of our data acquisition system, DSP processing and on-line monitoring.

Three methods are used to monitor any movements of the detector after its installation: a series of light spots, a system of capacitive probes and tracks passing through the overlaps between neighbouring modules. The details are given in section 6.

Both the detector alignment, internal and external, and the efficient association of the Microvertex detector hits to the tracks reconstructed by the other tracking detectors of DELPHI are essential for satisfactory performance. Section 7 describes the procedures followed.

A detailed study of the detector performance has been made using the data collected in 1991. Section 8 provides details of the efficiency, intrinsic precision, impact parameter and two-track resolution of the detector.

Finally a summary is presented in section 9.

2. Silicon microstrip detectors

Each detector has a sensitive length of 52 mm for the Closer shell and 59 mm for the Inner and the

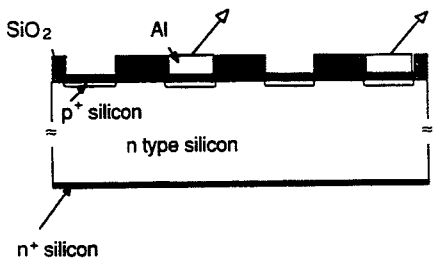

Fig. 3. Cross section of a detector with integrated coupling capacitors and biasing resistors.

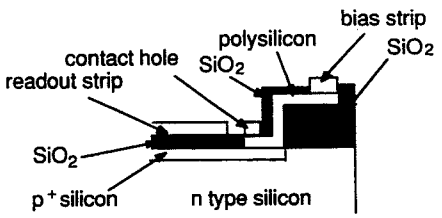

Fig. 4. Cross section through a strip of a detector with integrated coupling capacitors and biasing resistors.

Outer shell. The width of the detector changes from 19.2 mm (384 read-out channels) for the Closer shell through 25.6 mm (512 channels) for the Inner shell to 32 mm (640 channels) for the Outer shell.

2.1. Integrated coupling capacitors and biasing resistors

Silicon detectors with integrated coupling capacitors and biasing resistors [#4] are used in the DELPHI Microvertex detector [7]. The detectors are made on n-type silicon of a resistivity of 4.5 kΩcm to 5.5 kΩcm and deplete between 50 V and 60 V. The lattice orientation is ⟨111⟩. The diodes are formed by diffusion of boron atoms to a concentration of about 10^{18} atoms/cm^3. The diodes are 7 μm wide and are spaced every 25 μm. A layer of silicon dioxide, 0.23 μm thick, is grown during the diffusion, forming the coupling capacitor (see fig. 3). Every second strip has a metal readout line which makes a readout pitch of 50 μm.

The biasing voltage is applied to the diodes through individual polysilicon resistors. Fig. 4 shows a cross section of the silicon detector along a strip and its resistor. The p^+ diffusion line, silicon dioxide and the readout strip are shown. At the end of the diffusion line there is an opening in the coupling oxide where the diode and the resistor make contact. The contact hole is metallized, which makes it possible to measure the resistance of the polysilicon lines and the coupling capacitance. It is also used to check for low resistance connections between the aluminium readout lines and the implanted diodes, called pinholes. All the polysilicon resistors are connected to a common bias line, the bias strip, which runs around the detector.

Fig. 5 shows the top view of a silicon detector. The wide line, a guard ring, between the bias line and the strips is a diffusion line, whose purpose is to define the field and to collect the leakage current from the edge of the detector. Every readout line has four bond pads, two at each end, which serve to bond the first detector to the second detector and to the electronics. The reserve set of bond pads is used in case of an unsuccessful first bonding.

2.2. Acceptance criteria and tests

In order that the leakage current and the biasing resistors do not add more than 1000 electrons ENC the

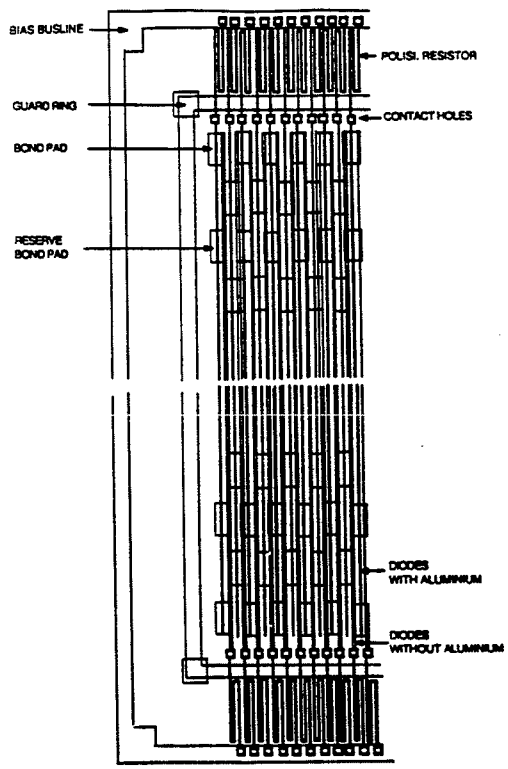

Fig. 5. Top view of a detector with integrated coupling capacitors and biasing resistors.

[#4] The detectors were produced by the Center for Industrial Research, Oslo, Norway.

values accepted were 10 nA/strip i.e. 7 to 12 μA total and more than 1 MΩ for the resistance. To ensure good charge collection and no capacitive losses to the neighbouring strips the lower limit for the coupling capacitance was set to 7 pF/cm. The application of these criteria to the Inner layer detectors is shown in figs. 6 and 7. Fig. 6a shows the leakage current measured on 200 silicon detectors. Most of the detectors satisfied the specifications. Fig. 6b shows the distribution of polysilicon resistors measured on the same sample. Some of them are below the design limit of 1 MΩ, but were accepted because of the deadline for assembling and inserting the Microvertex detector in DELPHI. Fig. 6c shows the coupling capacitance also measured on the Inner layer silicon detectors. All detectors passed this acceptance test.

Although pinholes in the coupling oxide are not lethal for the operation of single sided silicon detectors, they reduce the dynamic range of the electronics and should be avoided. The specifications stated that no more than three pinholes per detector are accepted. The distribution of the number of pinholes is shown in fig. 7a.

In addition to good spatial resolution a high detection efficiency is an important feature of the Microvertex detector. It is obtained by ensuring that the active elements have no defects. Defects like interrupted strips or biasing resistors make an area of the silicon detector inactive. Connections between strips or resistors on the other hand degrade the position measurement, because the collected charge is spread over several channels. Defective strips were limited at not more than 1%. This means that no more than 7, 10 and 12 defective lines on the Closer, Inner and Outer layer detectors would be accepted. Fig. 7b shows the number of defective lines per detector with 1024 strips.

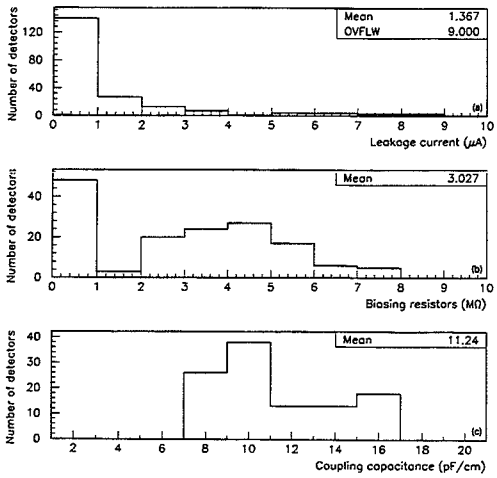

Fig. 6. Results of the standard checks applied to the Inner layer detectors. (a) Distribution of the leakage current. (b) The biasing resistance values. (c) The coupling capacitance values.

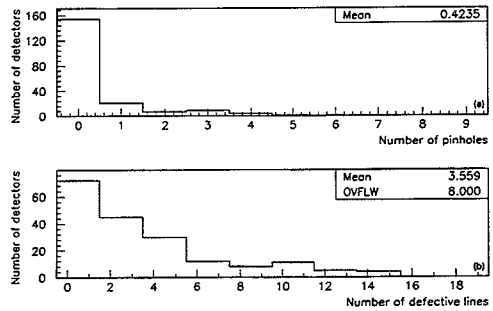

Fig. 7. Further checks for the Inner layer detectors. (a) The number of pinholes. (b) The number of defective strips.

In total 256 silicon detectors were tested for the Inner layer and 150 passed the acceptance criteria, a yield of 57%. Similar results were obtained for the detectors for the Outer layer produced at the same time. Detectors for the Closer layer, produced after the completion of the two others gave a higher yield of 75% thanks to the experience acquired with the previous production.

3. Detector modules

The basic building block of the Microvertex detector is pictured in fig. 8. The first photograph shows one whole module which is built out of two "half-modules", each consisting of two silicon detectors joined to a readout hybrid. A carbon fibre reinforcement profile is glued to the back of the four detectors. The second photograph is a close-up of a readout hybrid, which is a part both of the mechanical construction and of the electronic readout chain. Two screws through each hybrid attach the modules to the support structure (described in section 4). The readout chips (3, 4, or 5, depending on the layer) are glued onto the ceramic substrate of the hybrid. This substrate needs to be a good heat conductor in order to remove the heat generated by the readout chips. Each hybrid reads out two detectors with the strips connected to each other and to the amplifiers by wire-bonding. Thin flexible cables bring supply voltages and timing signals to the hybrid and take the multiplexed output signal to the outside world.

3.1. Readout hybrid

The hybrids for the first two layers (Outer and Inner) are the same except for the width. They are made of aluminium oxide and are aligned to the paddle-wheel-shaped support rings by a smooth reference edge. The heat conductivity of aluminium oxide is 25 W/(m K). The hybrids for the third layer (Closer) are made of beryllium oxide, which has a heat conductivity of 300 W/(m K). They are aligned to the support by a

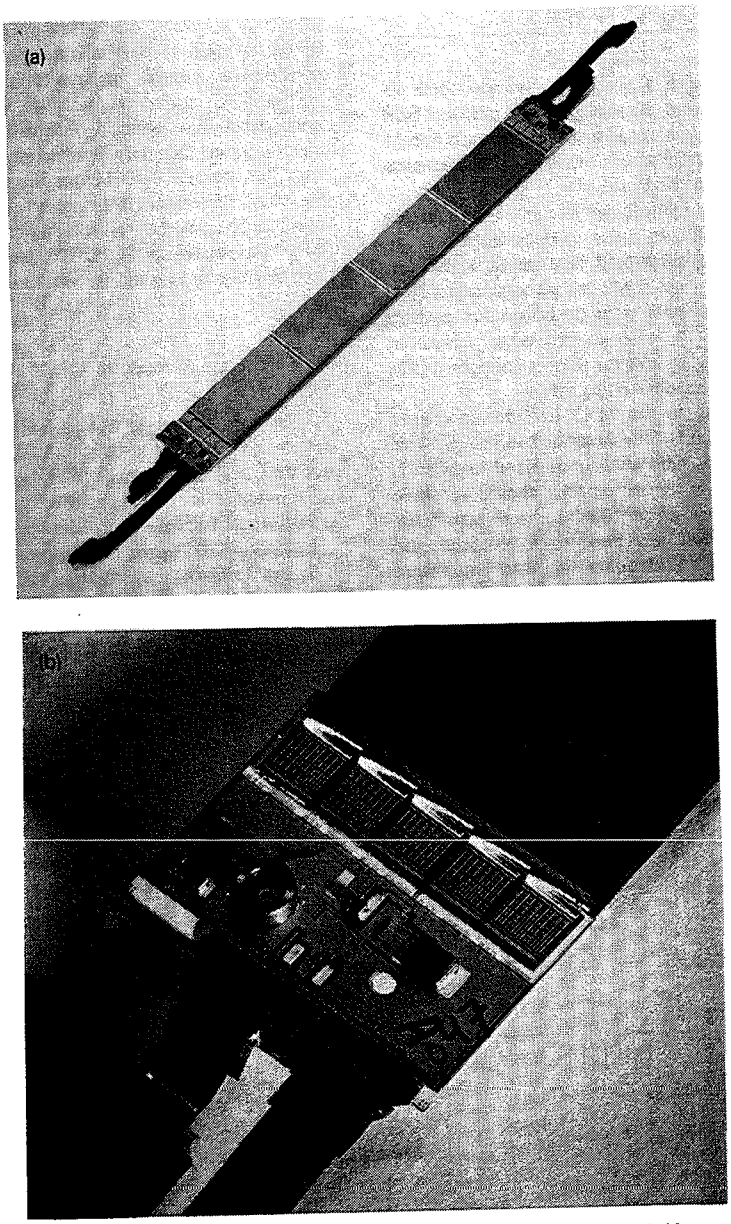

Fig. 8. (a) Outer layer detector module. (b) Close-up of the readout hybrid.

Table 1
MX3 specifications

Size	6.4 mm × 6.9 mm
Number of amplifiers	128
Power	60 mW
Risetime (10–90)%	1 μs (BW limited)
Noise	670 + 55 e^-/pF
Readout rate	2.5 MHz

bush mounted through a precisely machined hole in the hybrid. To facilitate the survey of the modules (see below), a reference cylinder is mounted on each hybrid of the first two layers. For the third layer, a reference sphere is joined with the bush.

The Closer layer hybrids are designed for double-sided silicon detectors. In order to decrease the number of lines going to the hybrid, the timing signals are multiplexed on one line. They are deconvoluted by a custom made chip, which is mounted on the bottom side of the hybrid. A wrap-around edge connector brings the timing signals and the supply voltages to the top side, where the readout chips are.

The readout chip is the MX3 low power charge amplifier array, which is fully described in ref. [8]. The characteristics of this chip are summarized in table 1. Each readout strip is connected to a charge sensitive amplifier. A schematic circuit diagram is shown in fig. 9. Given the relatively low bandwidth required, the MX3 is able to give an adequate signal to noise ratio while dissipating less than 0.5 mW per channel. Double correlated sampling (i.e., taking the difference in integrated signal before and after the interaction) is used to reduce low frequency noise pick-up. In the actual configuration – two silicon detectors connected to a hybrid – the signal to noise ratio for a minimum ionizing particle is around 15:1.

The CMOS technology assures a uniform gain among the 128 amplifiers in the chip. Injecting charge through the calibrate inputs or pulsing the detector back-plane shows that the gain variation within one chip is less than two percent. The variation from chip to chip within one production batch is of the same order of magnitude. The 128 outputs are read out serially at a rate of 2.5 MHz on a single twisted pair. Groups of chips (6 or 9) are daisy-chained to the same readout bus to further reduce the number of lines.

The MX3 radiation tolerance was investigated in some detail. The general observation was that radiation increased the measured noise values almost linearly, but the rate varied from one production batch to the other. This increase in noise was eventually understood to be caused by a worsening leakage current on the input protection FOXFET devices. The radiation dose leading to chip failure varied in the range 50–850 Gy.

3.2. Production of modules

The main challenge was to build a rigid and stable structure with the introduction of a minimum of extra material. Another aim was to make the strips as parallel as possible to the z-axis (the beam direction). This is important because these detectors do not measure the z-coordinate, which is only known to a precision of 1–2 mm from the other DELPHI tracking detectors. Thus, if the strip angles were too large (more than a few mrad from the z-axis), the high resolution in the perpendicular plane would be compromised. This leads to the requirement that the four detectors should be well aligned relative to each other and relative to the readout hybrids which are aligned to the support. The modules should also be flat.

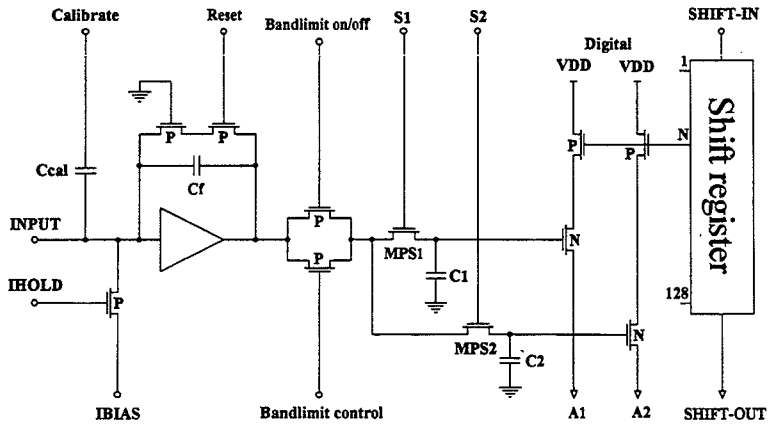

Fig. 9. The MX3 integrated circuit. The 128 input pads are configured in two rows of 64 giving an effective pitch of 44 μm.

The assembly proceeds in several steps using a series of jigs. Each jig holds two pieces (detectors or hybrids) by vacuum and allows one of the pieces to be translated and rotated in the plane of the module. The jigs are mounted on top of two perpendicular translation tables equipped with precision stepper motors. The step sizes are 10 μm along the strips and 1 μm perpendicular to the strips. A metallurgical microscope, mounted above the setup, is used to observe reference features on the detectors and the hybrids. While moving the jig using the translation tables, the relative alignment between the two pieces is checked and adjusted before they are joined.

First, two silicon detectors are joined by glueing two small silicon bridging pieces to the back side. Next, a readout hybrid is attached by glueing one edge of the detector pair directly on top of the edge of the hybrid. At this stage, the strips on the two detectors are connected to each other and to the inputs of the readout chips by a semi-automatic bonding machine. The resulting half-module is then tested electrically. This test includes a back-plane pulsing and a scan with a pulsed infrared laser spot.

Two half-modules are joined by two small bridging pieces as in the first step above. All bridging pieces are metallized on the side facing the back of the detectors, thus providing the connection for the back-plane voltage between the four detectors. The connections for the strip bias voltage and the guard ring voltage are made by wire-bonding.

To strengthen the modules and to make them easier to handle, a trapezoidal, 200 μm thick carbon fibre profile is glued to the back of the four detectors. To avoid a bimetal-like bending of the module caused by the different thermal expansion coefficients, a 2 mm wide and 300 μm thick silicon piece is glued to the other side of the carbon fibre bar. This extra silicon piece also increases the rigidity of the module by roughly a factor of 4. The complete module then undergoes final electrical tests.

The detector modules are measured using the production setup and a simple support jig. The control unit for the stepping motors is linked to a computer, which records the positions of the two translation tables. The strips on the silicon detectors are observed through the microscope and their positions determined with respect to the reference cylinders (or spheres) on the readout hybrids. A three-dimensional survey of the assembled half-shells (section 4.3) measures the cylinders, the spheres and the planes of all silicon detectors.

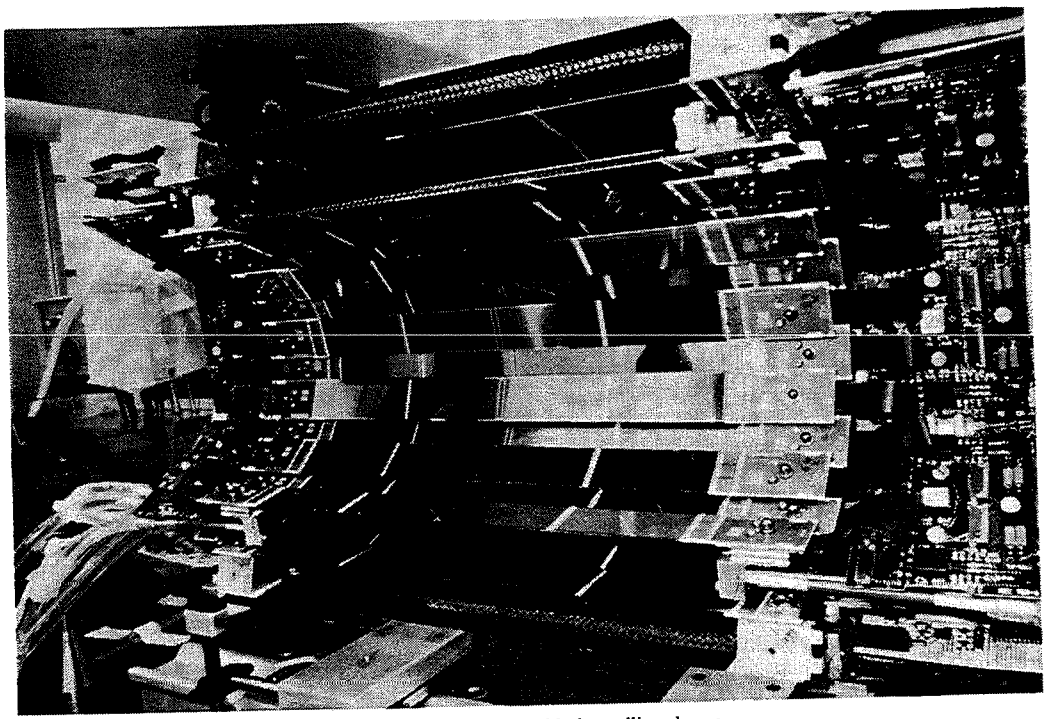

Fig. 10. One half-shell with three silicon layers.

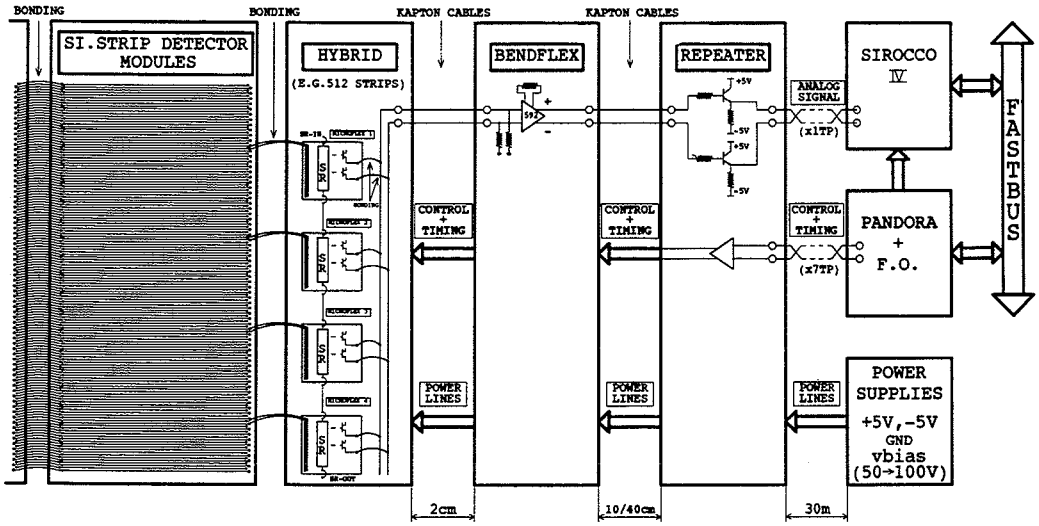

Fig. 11. Functional diagram of the readout electronics.

4. Half-shells

To build the Microvertex detector, the detector modules described in the previous section are assembled into two half-shells. Fig. 10 shows a photograph of one half-shell with all three layers mounted. Each layer consists of twelve detector modules, which are mounted on aluminium support structures called end-rings. The modules themselves hold the two ends together. The thin flexible cables from the readout hybrids are connected to additional readout electronics mounted close to the end-rings. Cooling water flows through channels inside the end-rings and also through channels attached to the adjacent circuit boards.

4.1. Mechanical construction

The first two layers (Outer and Inner) are supported and cooled by the same end-rings, which look like paddle wheels in order to give a small overlap between neighbouring modules. Before the mounting of modules, the two ends are held together by three precision aluminium bars. These are successively removed as the modules are mounted. The third layer (Closer) is supported and cooled by another pair of end-rings, which are aligned to the first pair using a precision jig. After an initial alignment the pairs of rings can be dismounted and then relocated using precisely machined brackets. At this smaller radius, a paddle wheel arrangement would tilt the modules too much so that tracks would no longer be incident at 90°. Instead, the modules alternate between two different radii. (See fig. 2.)

The effective thickness of each aluminium end-ring is about 5 mm. The assembled half-shell is protected by inside and outside covers made of 1 mm thick foam [#5] coated on both sides with 20 μm aluminium foil.

There are five cooling channels per half-shell. These channels have an inner diameter of 3–5 mm and a typical water flow of 40 cl/min. The cooling water siphons between two reservoirs, which are both below the level of the Microvertex detector. The whole fluid system is maintained at a slight underpressure as an insurance against leaks.

The Microvertex detector is inserted into the DELPHI barrel between the Inner detector and the beam pipe. Small skates made of a low friction material (Delrin) are attached to the end-rings and to the adjacent circuit boards. These skates allow the half-shells to slide into place on carbon fibre rails mounted on the inner wall of the inner detector. Each half-shell rests on two rails, one at the bottom and one on the side. The two half-shells are not connected in any way, and there is no contact with the beam pipe.

4.2. Readout electronics

A functional diagram of the complete electronic readout is shown in fig. 11. Starting from the readout hybrid, the differential multiplexed output from the readout chips is transferred by a flexible Kapton cable to an analog differential line driver (NE592) on the

[#5] Rohacell, Roem Schweiz GmbH.

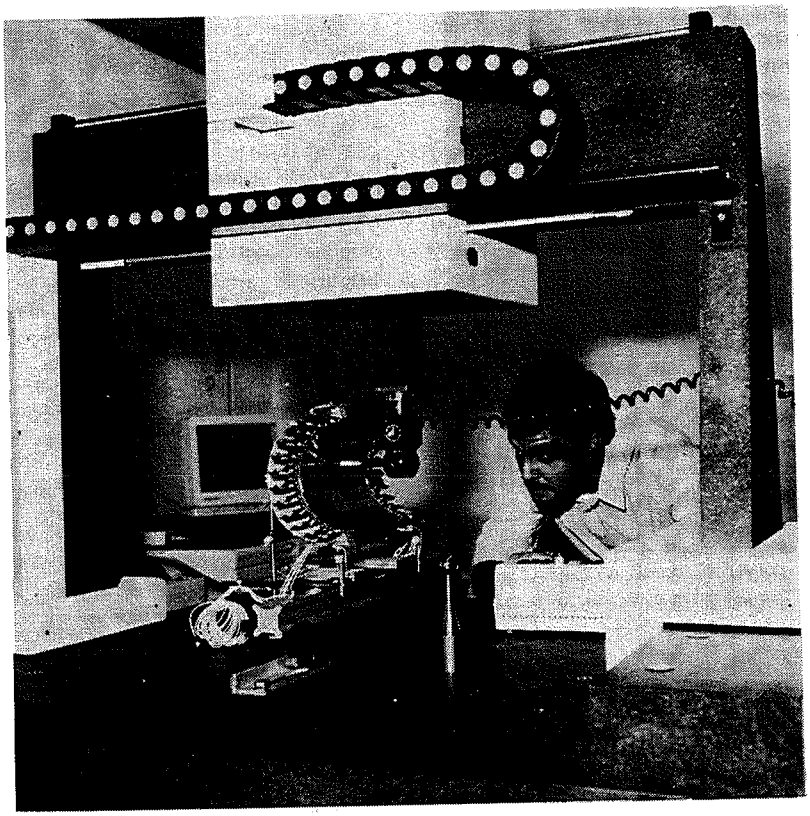

Fig. 12. One half-shell during a survey session.

"bendflex". This is a flexible printed circuit attached to each end of the half-shell. The signal then passes to an adjacent printed circuit board ("repeater"), where a simple emitter follower drives the signal to the counting room (a distance of about 25 m). There the analog signals are digitized and read out in the SIROCCO units (see section 5).

For the later third layer (Closer), the functions of the bendflex and the repeater were combined in a single printed circuit board attached to the half-shell. The NE592 amplifier plus emitter follower were replaced by a custom designed differential analog driver – the FDD [9].

All power supplies, monitoring electronics and control signal generators are situated in the counting room. The timing signals are derived from the standard DELPHI timing unit using a purpose-built fanout [10]. These signals go to the readout chips in the reverse direction through the repeater and bendflexes.

4.3. Survey

As a first step in the alignment of the Microvertex detector, the assembled half-shells are measured with a 3-D survey machine [#6]. Fig. 12 shows a half-shell (without the readout electronics) during a measurement session. The survey machine has a mechanical arm that moves in three orthogonal directions and supports a measuring head, which is a synthetic ruby stylus mounted on a touch probe triggered by a small force (about 10 g). The table and all supporting elements are made of granite to provide good stability. On calibration objects the specified accuracy is $(3 + d/(2 \times 10^5))\mu$m for a measurement of a distance d (in μm) between two points. The machine measures the

[#6] The Galaxy survey machine, POLI S.p.A., Varallo Sesia, Italy.

planes of all silicon detectors and the reference cylinders (or spheres) on all readout hybrids. The position of the strips in the plane of a module relative to the reference objects is measured separately under a microscope (section 3.2).

Each half-shell is measured twice, since the middle layer is normally not accessible to the measuring probe. One survey measuring the first two layers (Outer and Inner) takes place when only those two are mounted. Another survey measuring the first and the third layers (Outer and Closer) is done after all three layers have been mounted. During all surveys, warm water (25°C) circulates in the cooling channels in order to simulate normal working conditions. The two measurements of the Outer layer are overlapped and found to be consistent.

The mapping precision achieved, taking all uncertainties into account, is better than 20 μm. All the steps are described in more detail elsewhere [11]. An alignment using tracks (section 7.2) later refines the strip positions in the planes of the modules, but it is not sensitive enough to improve the radial positions. However, since the radial coordinate has less influence in the track fit, the precision of the survey is sufficient.

5. Data acquisition

The data acquisition for the Microvertex detector is an integral part of the DELPHI data acquisition system. Only those stages that are particular to the Microvertex detector are described here.

5.1. Readout and on-line analysis

Synchronously with each LEP bunch crossing (every 22 μs) the charge collected on each strip is recorded by the MX3 chips. If there is no DELPHI trigger, this information is overwritten during the next bunch crossing, otherwise the next capture cycle is skipped while waiting for the second level trigger. If the event is accepted, the charge is serially read out and digitized by 36 SIROCCO Fastbus modules [#7] [12]. Each SIROCCO has two independent readout units with a 10 MHz flash ADC [#8] for the digitization and a digital signal processor DSP56001 [#9] [13] for zero suppression.

[#7] Designed for the DELPHI Microvertex detector by the CERN Electronics Division.
[#8] Produced by TRW.
[#9] Manufactured by Motorola Inc.

The input to each SIROCCO readout unit is one of the 72 multiplexed analog signals from the Microvertex detector. One analog signal carries the information from either nine MX3 chips containing 1152 channels (Outer and Inner layers) or six MX3 chips containing 768 channels (Closer layer). At a 2.5 MHz readout speed, the digitization takes about 500 μs, after which the Microvertex detector is ready for the next trigger. The 72 DSPs further analyse the data, compressing the 73 728 channels into typically 1000 32-bit words for a hadronic Z^0 event or 150 words for an empty event. An event is analyzed in about 30 ms, comfortably faster than the maximum second level trigger rate of 5 Hz.

In order to find the channels with interesting data, it is necessary to evaluate three quantities: the individual channel pedestal, the common noise and the individual channel noise. The channel pedestals and the common noise are subtracted from the data, and the RMS of the channel noise is used as a reference for distinguishing true signals from background noise. All three quantities are recorded together with the data and used in the on-line and off-line monitoring.

The channel pedestals are assumed to be constant ~~or slowly~~ changing. The values are continually updated using a running average technique, where the new pedestal value is equal to $(1 - w_p)$ times the old value plus w_p times the channel ADC value. The weight w_p is chosen to be 1/32, which updates the pedestals sufficiently fast, while still being relatively insensitive to noise fluctuations.

The common noise is evaluated for each MX3 chip. It is calculated every event by averaging over all channels belonging to the same chip. The individual channel signal is then obtained by subtracting the channel pedestal and the common noise from the ADC value.

The RMS of the individual channel noise is also updated continually via a running average technique. The new RMS value squared is equal to $(1 - w_n)$ times the old value squared plus w_n times the signal squared, where w_n is chosen to be 1/1024. The channel signal-to-noise ratio is equal to the channel signal divided by the RMS noise.

A cut is made by demanding that the sum of the signal-to-noise ratios of two neighbouring channels be greater than 6. Only channels that satisfy this cut, and a few of their neighbours, are kept. This was shown to work well since events without tracks had typically three noise hits, while for tracks passing through the detector the efficiency was close to 100%, as will be discussed in section 8. True signals have their charge spread over two or three channels with the sum of signal-to-noise ratios peaked around 15.

The data records produced by the SIROCCO modules are read out by the DELPHI data acquisition system and written to cassette together with records from the other DELPHI sub-detectors.

5.2. Monitoring

The data quality is monitored on-line with an event display and a monitor program. The event display shows a single selected event. It gives a global view of the hits registered by the Microvertex detector (fig. 13a) and can also show detailed information for any of the clusters (fig. 13b).

The on-line monitor analyses the Microvertex detector data and fills a series of histograms which allow the detector performance to be evaluated. There are histograms with, for example, pedestal and noise values, signal-to-noise ratios and the number of clusters. A simple event reconstruction provides track segments, track residuals and a vertex position. Some of these quantities not only check the data from the Microver-

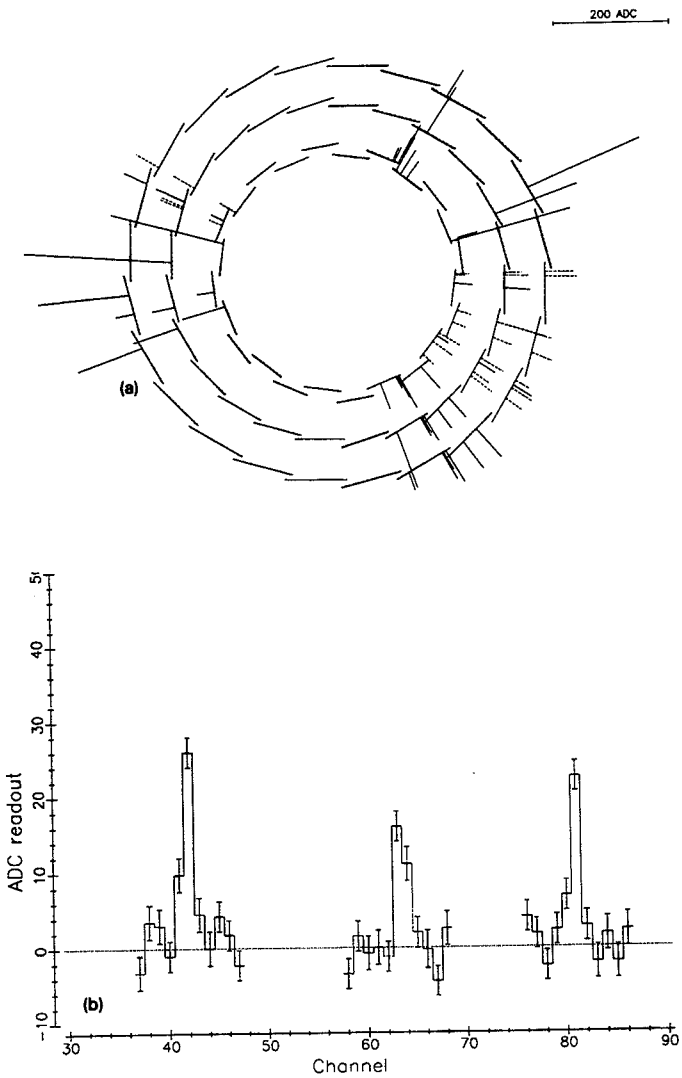

Fig. 13. (a) An on-line display of a hadronic Z^0 decay. (b) A detail showing three adjacent clusters of this event.

tex detector, but also give DELPHI valuable information on the running conditions. The number of clusters per event, for example, is a good monitor of the beam background, and the average position of the reconstructed vertices is an estimate of the beam position.

6. Mechanical stability

The mechanical stability of the Microvertex detector during data taking is essential, since a 1°C temperature change expands the support structure by 5 μm, an amount comparable to the intrinsic precision of the detector. The end-rings are made of aluminium, chosen for its ability to transmit heat, through which water is circulated, removing the 70 W generated by the readout electronics and stabilizing the temperature to 0.3°C. Temperature fluctuations are measured by resistive thermometers located at two points on each end-ring, and provide measurements accurate to 0.2°C once a minute. Two dedicated position monitoring systems measure any movements of the Microvertex detector with respect to the Inner detector and are described below. Movements internal to the Microvertex detector are investigated by an off line software analysis.

6.1. Capacitive probe position monitoring

A series of capacitive probes [#10] are mounted at the top and side of the Microvertex detector's end-rings and on the inside wall of the Inner detector [14]. The probes measure the capacitance, using a 15 kHz signal. Three distinct geometries measure the gap between the two detectors: radially via 8 probes, two on each of the four end-rings; laterally through a similar set; and longitudinally, along the beam axis, through one probe on each half-shell. The radial gap can be measured with a precision of better than 1 μm while the other probes are sensitive to 10 μm movements. The capacitive probe data is recorded every minute by the detector monitoring system which also reads out the thermometer values. This is done independently of the DELPHI data acquisition and necessitates an offline correlation of the probe values with the DELPHI data.

6.2. Light spot position monitoring

The second position monitoring system uses a series of light spots which shine on the Outer layer of silicon detectors. Infrared light from a gallium arsenide laser with a wavelength of 904 nm [#11] is transported from a laser diode situated outside the detector by 48 10-m long 100 μm diameter optical fibres. The light is focussed onto the detectors using small lenses and prisms [#12]. Four light spots shine on every second Outer layer module; two doublets on either end, one with the beam perpendicular to the silicon, the other inclined at a 28° angle with respect to the normal. In principle, these allow a decoupling of radial and tangential module motion. In practice, we observe only small shifts (see below) and hence the differential movement between perpendicular and inclined light spots has not been observed.

The light diodes are pulsed every 64th beam crossing, thus merging light spot measurements with e^+e^- collisions. The 1 kHz rate is limited by the light diode recovery time but still provides sufficient overlap between light diode flashes and triggered DELPHI events. A single light flash provides a 5 μm measurement which averaged over an hour of data taking determines the tangential module position relative to the Inner detector to about 1 μm.

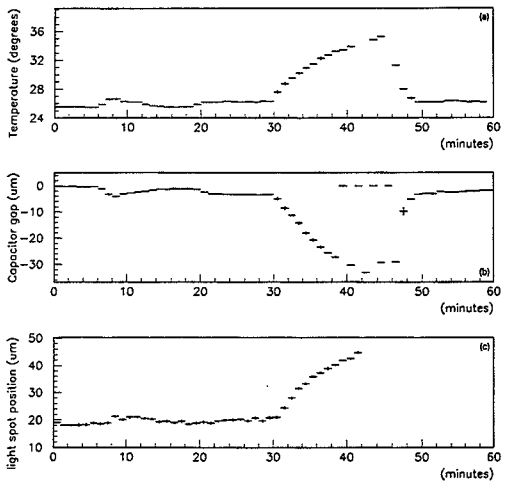

Fig. 14. Response of the Microvertex detector during a forced temperature scan: (a) The detector support structure temperature. (b) A radial gap as measured by the capacitive probes. (c) A tangential light spot position.

6.3. Calibration and results

Both of these systems were calibrated in-situ. The detector was heated by reducing the water flow in the

[#10] A commercially available capacitive probe readout system manufactured by CAPACITEC Inc., 87 Fitchburg Rd., Ayer MA, 01432, USA.

[#11] SG 2001 A.

[#12] A lens-prism combination manufactured by Fisba Optik, CH-9016 St. Gallen, optical fibres by Cableoptic S.A., CH-2016, Cortoillod and custom ordered fibre positioning guides produced by Technika Grenchen, Geneva.

cooling system, thereby causing the end-rings to expand. Fig. 14 shows the end-ring temperature variation during this one hour test. For comparison is plotted a radial gap measurement (capacitors) and a tangential module position (light spots) during this same period. The correlation is clear.

Over the 9 months of data taking in 1991, no motion in excess of 10 μm was observed, however steady drifts of 5 to 7 μm are seen over a period of weeks (see fig. 15). Considerable jumps (20 to 30 μm) can occur outside of data taking when the detector was switched off or DELPHI was opened for repairs, but the modules return to their original position on the resumption of stable operation. At the few micron level, hysteresis and un-correlated behaviour on neighbouring detectors make it impossible to infer the position of modules which are not monitored with a light spot. Thus this information is not used in a time

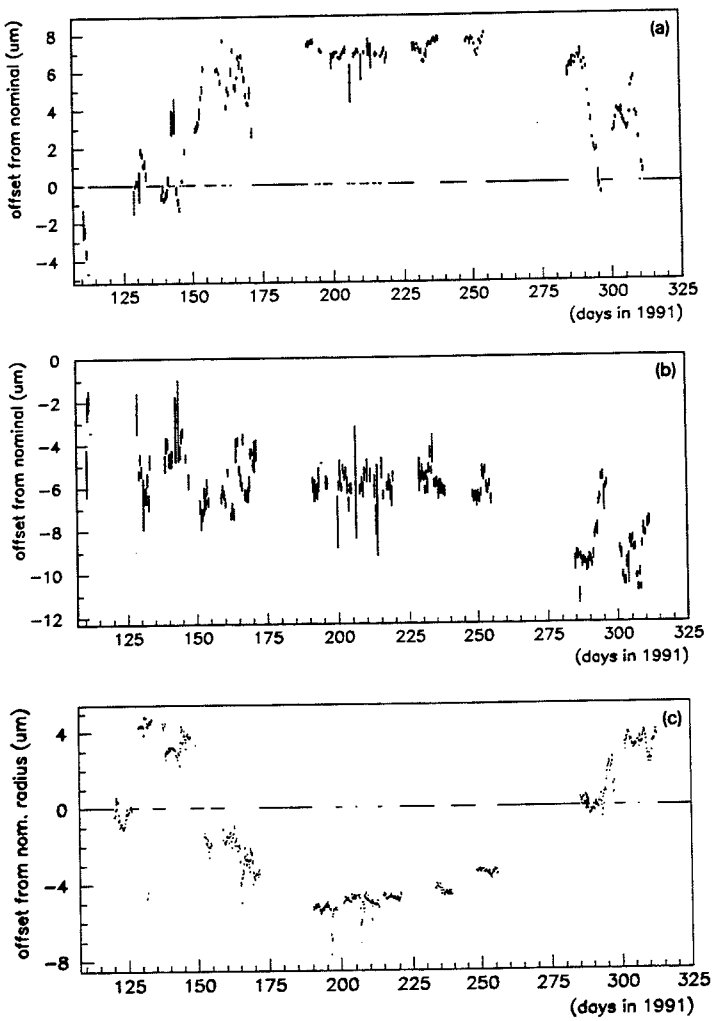

Fig. 15. Light spot and capacitive probe position over the entire 1991 running period. (a) A light spot on the top module in a half shell. (b) A light spot on one from a bottom module in the half shell, which is more tightly constrained by the detector support structure. (c) A radial position of the top capacitive probe.

dependent alignment of the detector but rather to signal the presence of large shifts and identify stable periods of operation.

6.4. Position monitoring with tracks

The stability of the detector was monitored using tracks which pass through the overlap regions, both of neighbouring modules within a half-shell and of the overlaps occurring between the two half-shells. Charged tracks from hadronic Z^0 decays passing through overlaps having at least three hits and a minimum transverse momentum of 0.5 GeV were used. A circle fit was made through any two hits taking the curvature from the external tracking, and the distance of other hits from this track was calculated. The variation of this residual provides a measurement of the detector stability. Under typical running conditions there are 50 tracks/day/overlap which provide a measurement accuracy of better than 2 μm.

During the 1991 data taking period the contribution to the precision from mechanical instabilities is estimated to be less than 3 μm. The overlaps between the two half-shells (fig. 16a) behave no differently than those within the same half shell (fig. 16b). The average RMS of the 1991 residual distributions of all overlaps was less than 2 μm (fig. 16c).

7. Off-line reconstruction and alignment

As described in section 5.1, only clusters with a signal larger than six times the single channel noise were written to cassette. The off-line analysis starts by calculating the position of each cluster in the local coordinate system of a singe silicon detector. This one-dimensional position is the pulse height weighted average of the strip with the largest pulse height and its largest neighbour. The analysis then proceeds by associating the Microvertex detector clusters with tracks found in the rest of the DELPHI tracking detectors. The z coordinate from the associated track is used to correct each cluster position for the effect of any small

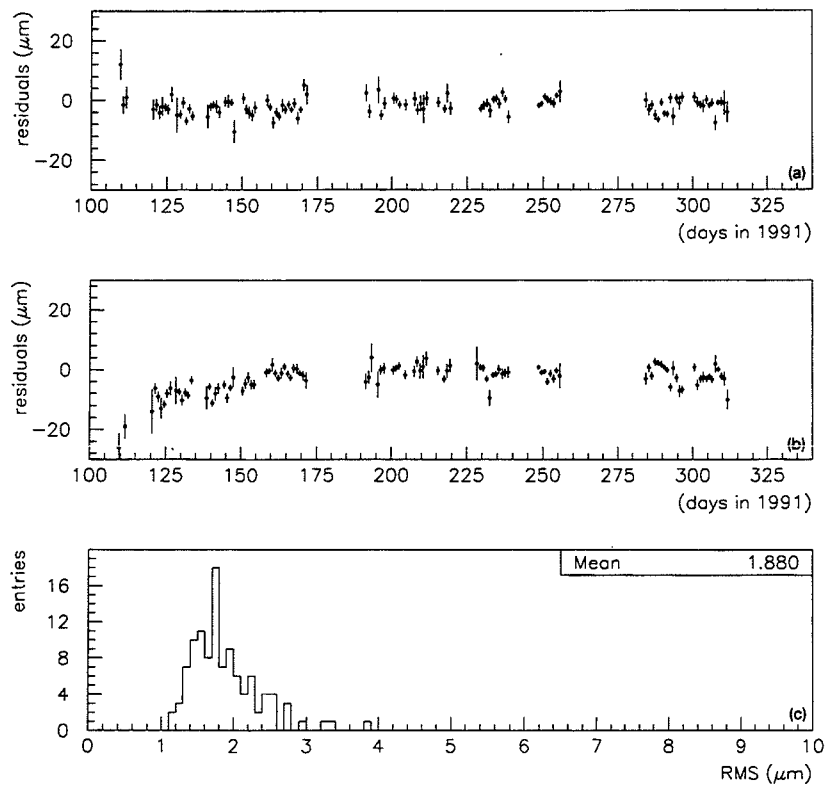

Fig. 16. Sector overlap stability, measured with particle tracks. (a) Residuals measured at the top half shell overlap. (b) Residuals measured in an overlap within a half-shell. (c) Histogram of RMS values of the 1991 residual distribution of all overlaps.

angle between the strips and the z axis. Associated and corrected hits are then included in a final track fit. This section describes the association between tracks and clusters and the detector alignment using tracks. More detailed cluster studies are presented in section 8.

7.1. Association

As indicated above, tracks are first found without using the Microvertex detector. In a second stage, the tracks are extrapolated to the three silicon layers and associated with the clusters. If the external track extrapolations were accurate enough, on the order of the readout pitch (50 μm), the track-cluster association would be straightforward. There would be at most one possible cluster per layer. Unfortunately, the track extrapolation precision will never reach that level. The typical uncertainty on these extrapolations was 250 μm, but has recently been reduced to 150 μm. This improvement arose using the Microvertex detector to calibrate the other tracking detectors. The large track extrapolation uncertainties create ambiguities in the association of clusters to tracks in events with a high track density. Both in jets and three-prong tau decays, for example, it is very common to have two tracks separated by less than one millimeter at the radius of the Microvertex detector.

With the track uncertainties and track density indicated above, it is clear that we cannot expect to make a unique association in each silicon layer separately. But by using all three layers together, we can eliminate many of the ambiguities. The procedure starts by setting a window around a track in the first (Outer) layer. The size of this first window depends on how well the track position at the Microvertex detector was determined by the external track fit and is typically of the order of one mm. For each cluster found within the window, the track is forced through that cluster and extrapolated to the next silicon layer, where a more narrow search window can be used. The size of this second window depends on how well the track angle is known from the external fit and, for low momentum tracks, on the expected amount of multiple scattering. If a cluster is found in the second layer, the track can be forced through two clusters and extrapolated to the third (Closer) silicon layer. At this point, the uncertainties on the original track are virtually eliminated, and a possible third cluster is required to lie within a very narrow window with a full width of one to two hundred microns.

This sequence of tighter and tighter cuts removes most of the ambiguities in the track-cluster association. Fig. 17 shows the fraction of tracks that are uniquely associated to clusters, as a function of the track multiplicity, in the fifteen-degree sector to which the track belongs. In hadronic Z^0 decays, the most populated sector typically has a track multiplicity of four or five. The figure shows how the number of ambiguities is successively reduced by the second and third layers. Having no ambiguities for a track does not necessarily mean that the association is correct, but it is a good start.

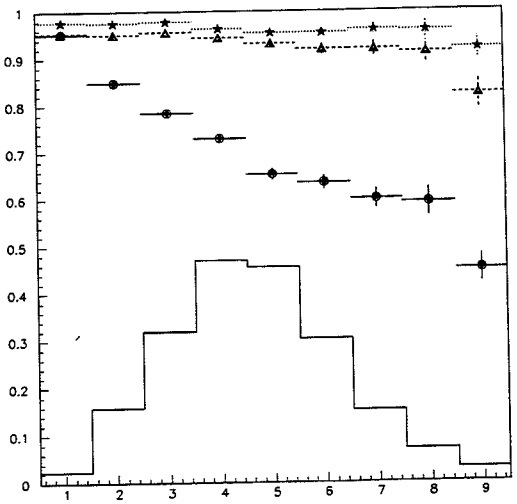

Fig. 17. Fraction of tracks uniquely associated to clusters as a function of the local track multiplicity for the cases of one silicon layer (circles), two layers (triangles) and three layers (stars). The histogram shows the track multiplicity in the most hit sector for hadronic Z^0 events.

A non-negligible fraction (about 15%) of the external tracks have much larger uncertainties than the typical ones given above. Many of these tracks can be correctly associated to clusters by doing a second pass with much looser cuts in the first and second layers. The cut in the third layer remains the same, because it does not depend on the external tracking. The looser cuts do not create many ambiguities, since most of the clusters are already associated to other tracks. Because of inefficiencies in the Microvertex detector, some tracks do not find clusters in all three layers, in which case the association is less reliable. It is also possible for a track to find more than three clusters (up to a maximum of six) if it goes through an overlap between two sectors.

7.2. Alignment

The starting point for a software alignment of the Microvertex detector is the mechanical measurement, in which the relative module positions in the same half-shell are known with an accuracy of 20 μm.

There are two steps to the software alignment procedure. In the first step, we align the two half-shells relative to each other with a precision of 10 μm and position the complete detector within the DELPHI reference frame. In the second, we improve the module positions within the detector using a minimization procedure which is internal to the Microvertex detector. The remaining systematic uncertainties are of the order of 5 μm.

7.2.1. External alignment

The Outer detector, built of 24 planks of drift tubes with an intrinsic measurement precision of 100 μm and an overall alignment precision of 700 μm at a radius of two meters defines the DELPHI reference frame.

The alignment uses 2000 di-muon events with hits in the Microvertex and Outer detectors. Viewed in the $R\phi$ plane, a muon pair describes the arc of a circle, neglecting initial and final state radiation effects. The Outer detector hits define a circle, with a curvature calculated from the beam energy and the polar angle. The residuals between the Microvertex hits and the circle are minimized by considering translations in the x and y coordinates (there being no z measurement in the Microvertex detector), and three rotations. In this way, we place each half-shell in the centre of DELPHI with an accuracy of 30 μm.

Further improvement in the orientation of each half-shell is obtained as follows. With an effective resolution for di-muon events of 700 μm at a distance of two meters from the interaction region, the Outer detector determines the muon direction at the Microvertex detector with an accuracy of 0.3 mrad. Imposing this constraint on each muon improves the orientation of each half-shell. Furthermore, each di-muon event can be forced through the Outer layer of the first half-shell with the track direction as given by the Outer detector. By minimizing the hit residuals in the second half-shell to this track, we place the two half-shells, relative to each other, to better than 10 μm.

After this first step, the position of each module in the frame of each half-shell is known to 20 μm. The position of each half-shell in the frame of the Microvertex detector is known to 10 μm, and the position of the Microvertex detector in the DELPHI frame is known to 30 μm.

7.2.2. Internal alignment

In the second step, two techniques are used to align the individual modules of the Microvertex detector.

The first technique uses the di-muons again. A least squares fit is made for each di-muon, with the uncertainty on each Outer detector point set at 700 μm, and on each Microvertex detector point at 8 μm. Two translations and a rotation per module minimize the hit residuals to this constructed track. The translations are along the module plane (thus approximating an $R\phi$ shift), normal to the plane (thus approximately an R shift) and a rotation in the plane. There is no sensitivity to movements in z, and very little to rotations out of the plane.

The second technique uses hadronic events. On an event-by-event basis, all tracks with momentum greater than 1 GeV/c having a hit in each layer of the Microvertex detector are considered. We extrapolate these to the interaction region and find a common vertex. The uncertainty on the vertex and the chi-squared probability are calculated. The latter is reasonably flat except for a large spike at zero. A cut in chi-squared probability at the 1% level eliminates events with secondary vertices and those with ill-measured tracks. For each track, in each event passing these cuts, we refit with the hits in the Microvertex detector and a vertex constraint. The residuals, to each of these refitted tracks, are minimised using the same shifts and rotations per module discussed above. The shifts and rotations applied to each module are consistent between the two techniques.

The precision of the Microvertex detector can be determined by a number of tests, the full details of which are documented elsewhere [15].

Of particular importance is the impact parameter resolution defined in eq. (1). This is not measured directly because of the finite size of the interaction region, however it can be deduced from the apparent distance between the two muons in a di-muon event, both extrapolated back to the interaction region. We refer to this quantity as the "Muon Miss Distance" and

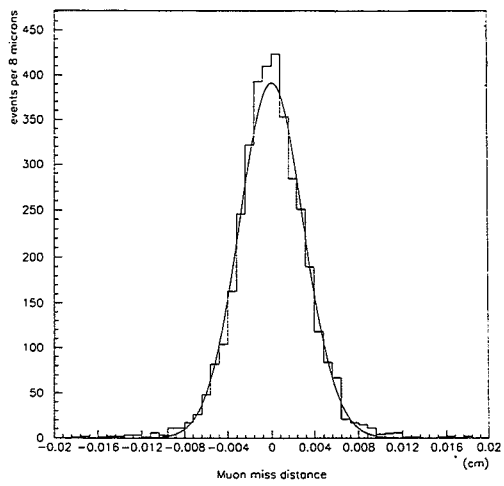

Fig. 18. The distribution of the reconstructed distance between the two muons in $Z^0 \rightarrow \mu^+\mu^-$ events.

plot it in fig. 18. It can be shown that $\sigma_{MMD} = \sqrt{2}\sigma_{IP}$ and thus the impact parameter resolution for high momentum tracks is 21 μm. This also implies a single point precision in the Microvertex detector of 8 μm.

Direct tests of the vertexing ability of the detector are performed in two ways. Firstly in the reconstruction of the point at which tau leptons decay into 3 charged tracks. With the Microvertex single point resolution set at the above mentioned 8 μm, and with due account being taken of multiple scattering, the chisquared probability distribution is flat showing that the resolution has been correctly estimated. Secondly from an enriched sample of Z^0's decaying to quarks u, d, s, an attempt is made to reconstruct the primary vertex. These are consistent with the centre of the beamspot within the calculated errors, and from the resulting distribution it is shown that possible systematics in the radial position of reconstructed vertices are less than 15 μm.

Moreover, several tests concerning the internal consistency of the detector are described in section 8. 3.

In conclusion, we align the modules of the Microvertex detector with respect to each other to an accuracy of 5 μm. The detector position in the DELPHI frame is known, with an accuracy of 30 μm. Numerous tests referred to above, show the internal resolution, time averaged over the 1991 data-taling period, to be 8 μm.

8. Detector performance

8.1. Efficiency

After the installation two detectors had electrical faults, rendering 2.3% of the channels inoperative from the start of the run. During the run a few more detectors developed problems, which were later understood to be caused by bond-wire failures, and in one case a micro-crack in the ceramic hybrid. This caused 8.5% of the channels to be dead at the end of the running period. It should be noted however that, for the whole period, at least one layer was operative for 100% of the ϕ coverage, and for 93% of ϕ there were at least two hits per track.

The efficiency, studied with tracks from the hadronic decays of Z^0s, in a fiducial area of the detector was 95.5%, 97.5% and 96.3% for the Closer, Inner and Outer layer respectively. The inefficiencies include a small contribution of the association efficiency to tracks found by the other tracking detectors in DELPHI, a contribution related to the quality of tracks and a contribution due to noisy channels in the Microvertex detector. The first two contributions can be eliminated by calculating the efficiency for the good quality tracks from the leptonic decays of Z^0s. The corresponding numbers were 97.5%, 99.0% and 97.9%.

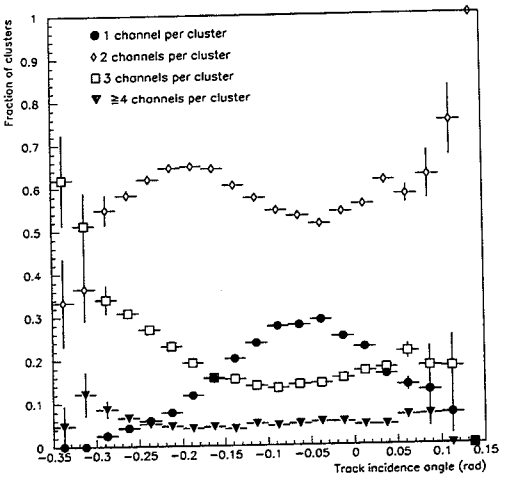

Fig. 19. The fraction of clusters with 1, 2, 3 and more than 3 channels per cluster as a function of the incidence angle of a track in the silicon.

8.2. Cluster characteristics

A channel is defined as belonging to a cluster if the ratio of its pulse height (PH) to its noise (N) is larger than a fraction f of the channel with the maximum PH/N in that cluster. A cluster is only accepted if the sum of the PH/N of the individual channels is larger than 6, and if there is at least one channel with a PH/N larger than 3. A value of 0.2 for the fraction f was found to give the best intrinsic precision. Notice that, as explained in section 3.1, no gain corrections are necessary to the data.

Fig. 19 shows the number of channels per cluster as a function of the incidence angle of the corresponding track with the detector in the $R\phi$ plane. As expected the fraction of 1-channel clusters decreases for increasing angle while more 3-channel clusters are found for non perpendicular tracks. Clusters with 4 or more channels are not expected for angles below 0.3 rad, and should be attributed to δ electrons, merging clusters and detector defects. Events with a hadronic decay of the Z^0 contained on average 65 clusters in the three layers of the detector. The clusters not associated with tracks have an average cluster width larger than the one for associated clusters. However they do not differ enough to distinguish them based on just the cluster size, nor does their number (3 per event) make it necessary to remove them.

The 1.23 T magnetic field in DELPHI is perpendicular to the electric field in the silicon and causes the holes in the silicon to drift with a Lorentz angle α_L relative to the electric field direction. Hence a minimal

cluster width will be obtained for tracks with an angle α_L relative to the normal of the detectors in the $R\phi$ plane. The minimal cluster size (see fig. 19) was found to correspond to $\alpha_L = 54$ mrad consistent for all detectors.

Due to the multiplexing of up to 1152 channels on one read-out line and the read-out speed, a cross-talk bias could be introduced in the clusters. To measure the size of this effect the difference in PH between the neighbouring channels of the channel with the largest PH in a cluster was determined normalized to the PH of the channel with the largest PH. This asymmetry in cluster shape is a function of the incidence angle of a track with the silicon, due to diffusion of the holes which drift to the implants. For tracks which traverse the silicon with the Lorentz angle there should be no asymmetry due to diffusion, and hence the remaining asymmetry is attributed to electronic cross-talk. The Inner and Outer modules (nine MX3-chips bussed together) showed a 4% forward cross-talk, because of the capacitive load on the output bus. For the Closer modules (six MX3-chips bussed together), groups of three chips were decoupled using diodes and no significant cross-talk was observed.

The full line in fig. 20 shows the PH distribution for typical detectors, normalized to the noise of one channel. The values have been also normalized to the minimal track length of a particle traversing the silicon, which is an average correction of 15%. The most probable value of the Landau distribution is 15. The dashed line in fig. 20 shows the PH/N distribution for

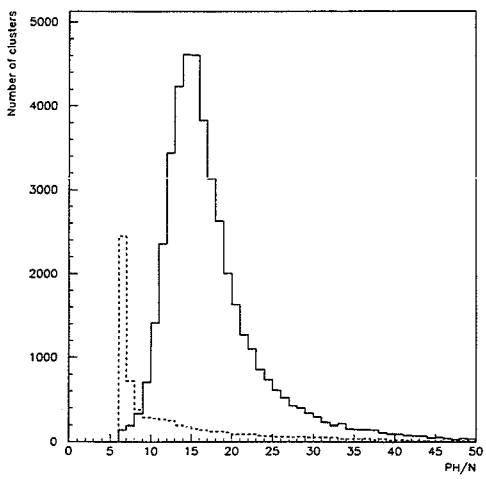

Fig. 20. PH/N for clusters with (full-line) and without (dashed-line) a track associated to them for the Inner layer modules. The PH/N has been normalized to the minimum track length in traversing the silicon.

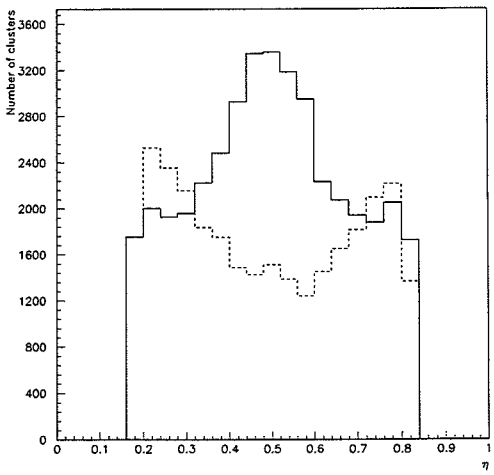

Fig. 21. The η distribution for tracks traversing the silicon with an angle relative to the Lorentz angle of 0.15–0.25 rad (full-line) and < 0.05 rad (dashed-line). Note that due to the definition of η (see text), η is restricted to $0.17 < \eta < 0.83$. All remaining clusters contain only one channel by definition and are not included in these distributions.

clusters which have not been associated to tracks, which clearly peaks towards small values. The position of a cluster is obtained by calculating $\eta = \mathrm{PH}(i+1)/(\mathrm{PH}(i) + \mathrm{PH}(i+1))$, where only the 2 channels with the largest PH are considered. Fig. 21 shows the η distribution for tracks which traverse the silicon at large angles (full-line), and tracks around the Lorentz angle (dashed-line). For the latter the function of the intermediate strip, which is not read-out, can clearly be observed. Note that due to the choice of 0.2 for f (see top of this section), η is restricted to $0.17 < \eta < 0.83$. All remaining clusters contain only one channel by definition. The true illumination of detectors is uniform in η, while the η distribution shows a clear non-uniform reconstruction of the hit position. Hence the reconstructed hit position should be corrected as a function of η. These corrections are obtained by comparing the found hit position with its predicted position using the other two layers, and are shown in fig. 22.

Due to smaller capacitance the charge loss in the intermediate strips is faster than in the read-out strips. This loss is furthermore a function of bias resistors, which vary from batch to batch, and of the integration time of the MX3 amplifier, which due to external requirements, notably to prevent pick-up of the clocking signals by the Inner detector of DELPHI, is twice the optimal value. Fig. 23 shows the relative PH in a cluster as a function of η for the three layers. Since the distributions are symmetric around 0.5, and the total

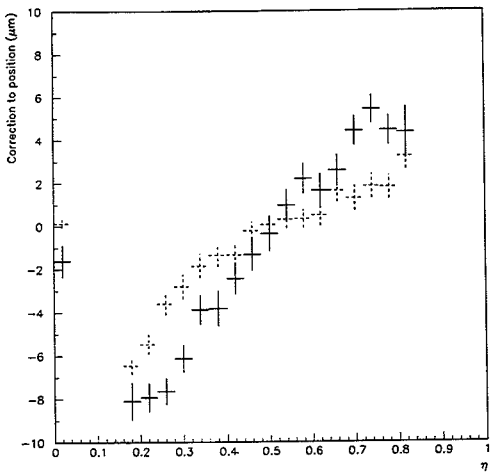

Fig. 22. Difference between hit position in the Inner layer and a track defined by Closer and Outer layers as a function of η for tracks traversing the silicon at large (full-line) and small (dashed-line) angles. Note that due to the definition of η (see text), η is restricted to $0.17 < \eta < 0.83$. All remaining clusters contain only one channel by definition and are included in these distributions at $\eta = 0$.

PH/N is sufficient no precision loss is expected due this PH loss.

8.3. Hit precision

The hit precision, independent of systematic alignment errors or time instabilities, has been found to be

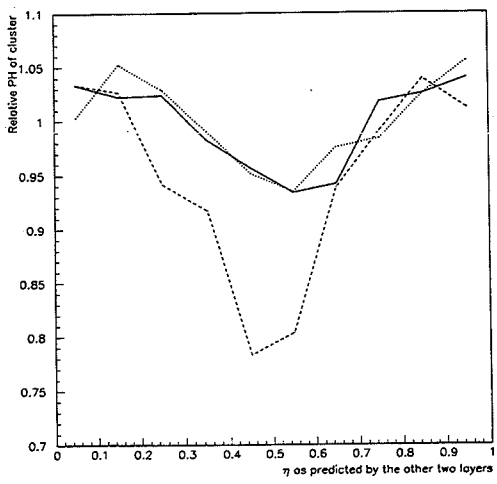

Fig. 23. Relative PH of a cluster as a function of η for Closer (full-line), Inner (dashed-line) and Outer (dotted-line) layers.

6 μm for tracks with an incidence angle in the silicon close to the Lorentz angle. This value is obtained by studying the overlaps between detectors in one layer, using as a pivot for the track one of the other layers. The residual distribution yields 6.1 μm for the Closer layer, where a track passes through both detectors in the overlap with an angle within 100 mrad relative to the Lorentz angle. For the Inner and Outer layers one of the two hits considered will always be produced by a track traversing the silicon at an angle close to 250 mrad, therefore giving rise to a larger residual. However the corresponding number for these layers is 7.4 μm, assuming that both hits have equal precision. As will be shown below, this precision can be interpreted as an average of the 6 μm for tracks close to the Lorentz angle and 9 μm for tracks at the largest incident angles.

To be able to assign proper errors to the hits, and study possible systematics effect, the precision of hits has been measured as a function of the following variables: incidence angle, cluster size, pulse height, η and noise. As measure for the precision the width of the residual distribution between a track defined by Closer and Outer layers and the corresponding hit in the Inner layer is used, the Inner layer being the layer under investigation. To this residual both the precision of the track and the hit in the Inner layer contribute, and if all layers would have identical errors the corresponding single hit precision equals 0.82 times the measured residual.

Fig. 24 shows the residual as a function of the incidence angle of a track at the Inner layer, showing that the best precision is obtained for tracks close to the Lorentz angle. For clusters which contain more than two channels, a cluster algorithm including only the two edge channels in the cluster has been studied. Fig. 25 shows a comparison between the precision of the η algorithm including only the two largest PH in the cluster (full-line), or ignoring the centre channel for clusters which contain three channels (dashed line). Only hits in the Inner layer with three channels per cluster are included, and the width of the residual distribution is plotted as a function of the incidence angle of the tracks at the Inner layer. Only if the angles with which the tracks traverse the silicon would have been larger would the present algorithm have to be modified to gain precision. Due to the 24-fold modularity in ϕ the algorithm which uses only the two largest PH gives the most precise positions.

Fig. 26 shows the residual as a function of the PH of the cluster in the Inner layer. The distribution shows that the best precision is obtained for tracks which deposit 20% more than the most probable amount of energy. The precision degrades for small pulse heights due to electronic noise. For large energy depositions a worse precision is caused by δ electrons or Landau

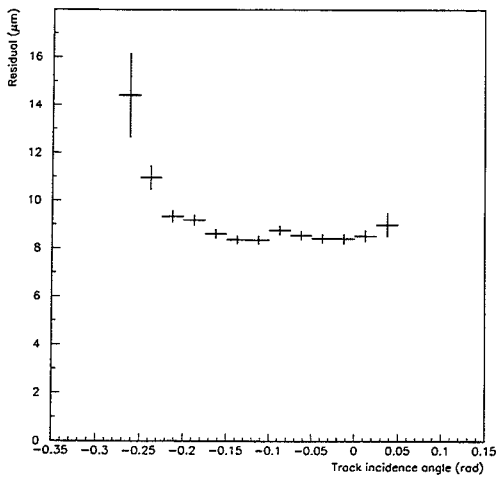

Fig. 24. The residual of a hit in the Inner layer relative to a track as defined by the Closer and Outer layers as a function of the incidence angle of a track for all clusters, using only the 2 largest PH in a cluster to determine η. To convert the residual to a hit precision multiply by 0.82 (see text).

fluctuations for non perpendicular tracks which both can pull the cluster centroid away from the track position.

Fig. 27 shows the residual as a function of η. As expected the best precision is obtained when the track

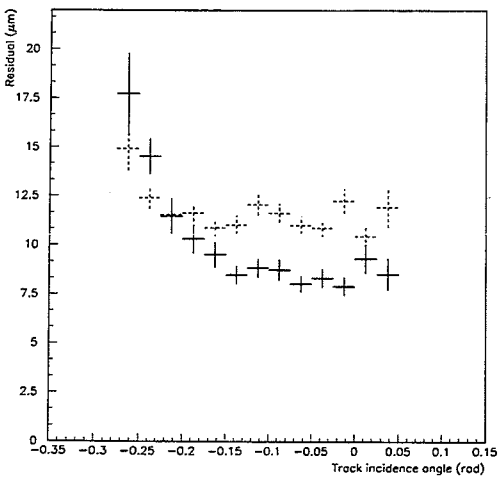

Fig. 25. The residual of a hit in the Inner layer relative to a track as defined by the Closer and Outer layers as a function of the incidence angle of a track. To convert the residual to a hit precision multiply by 0.82 (see text). Only clusters with 3 channels are included. The full and dashed lines refer to the two η algorithms as described in the text.

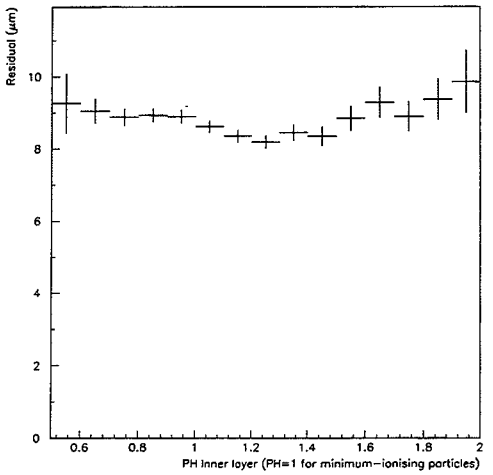

Fig. 26. The residual of a hit in the Inner layer relative to a track as defined by the Closer and Outer layers as a function of the PH of a cluster in the Inner layer. To convert the residual to a hit precision multiply by 0.82 (see text).

traverses the silicon in between the two channels which are read-out. Note that due to the cluster definition algorithm used, all η values less than 0.17 and above 0.83 produce only single channel clusters, which are put at $\eta = 0$.

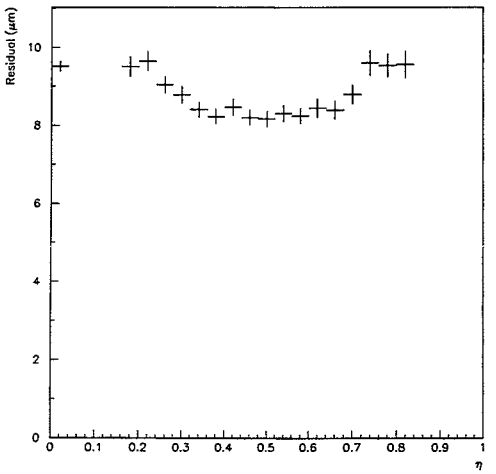

Fig. 27. The residual of a hit in the Inner layer relative to a track as defined by the Closer and Outer layers as a function off. To convert the residual to a hit precision multiply by 0.82 (see text). Note that due to the definition of η (see text), η is restricted to $0.17 < \eta < 0.83$. All remaining clusters contain only one channel by definition and are included in this distribution at $\eta = 0$.

A study was done to identify the hit precision based on the characteristics of clusters. Clusters are put into three categories which are defined by the PH and N values of the channels in and around the cluster. Fig. 28 shows the corresponding hit residual for the three categories, where it should be noted that the Closer and Outer layer hits have been selected to be of the best category. The precision ranges from 6.5 μm for 77% of the hits to 17 μm for the worst 6% of the hits.

8.4. Two-track resolution

Fig. 29 shows the probability that two tracks are each associated to two separate clusters as a function of the distance between the tracks. Fifty percent probability is reached at a track separation of 120 μm. For this study, only two of the three layers are used in the track fit. The tracks are then extrapolated to the third layer, where the separation between pairs of tracks is calculated. The non-zero values at very small track separations are usually caused by nearby clusters which are not related to either of the two tracks (and have been mistakenly associated to one of them).

The probability that at least one of the two tracks has an associated cluster is independent of the track separation, as is the total charge associated to the two tracks. In other words, if there is only one cluster associated to two close tracks, the charge of that cluster is twice the charge from a single track. A more sophisticated cluster algorithm would be able to split some of them and to give a better two-track resolution. However, with a readout pitch of 50 μm, one does not expect to be able to go much below 100 μm.

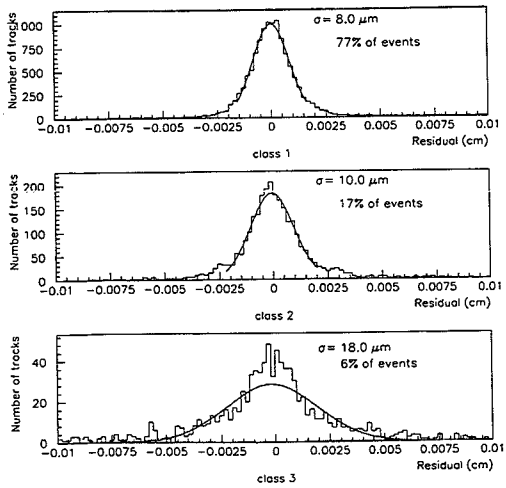

Fig. 28. The residual of a hit in the Inner layer relative to a track (with $p_t > 2$ GeV/c) as defined by the Closer and Outer layers as a function of the three categories of cluster types, which are defined in the text. To convert the residual to a hit precision multiply by 0.82 (see text).

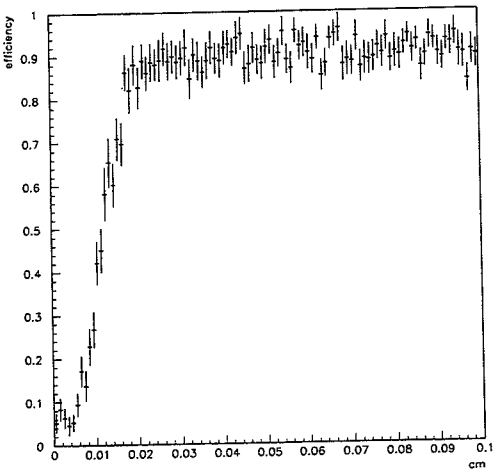

Fig. 29. Efficiency for two tracks to be associated to clusters in a silicon layer as a function of the track separation.

8.5. The impact parameter and its error

As has already been described in the section on alignment, the precision at the beamspot for tracks extrapolated from the Microvertex detector for di-muon events indicates an average error on the impact parameter, of 21 μm. This value is of course the asymptotic value, since for 45 GeV/c muons the multiple scattering contribution is negligible. The expected impact parameter error for hadronically produced tracks integrated over all angles as a function of the momentum of the tracks in the xy-plane can be described with $\sqrt{64^2/p_t^2 + 22^2}$ μm (p_t in GeV/c). A single hit precision of 8.4 μm derived from the alignment studies has been used. This value also gave a flat probability distribution for vertex fits in 3-prong tau decays. Due to the non uniform distribution of material, mainly in ϕ, and the possibility of having up to six hits in the Microvertex detector for a single track, this representation is only an approximation made to allow an easy comparison with the data.

To test the description of the errors in hadronic events an enriched light quark sample was selected using the following procedure. An event is split in two hemispheres according to its thrust axis ($T = \mathrm{Max}(\Sigma_i |\, \boldsymbol{p}_i \cdot \boldsymbol{n}\,| / \Sigma_i |\, \boldsymbol{p}_i\,|)$, where T is the thrust, $\boldsymbol{p}_i$ are the momentum vectors of the particles and $\boldsymbol{n}$ is a unit vector along the thrust axis). In each hemisphere a vertex is constructed by rejecting all tracks which miss

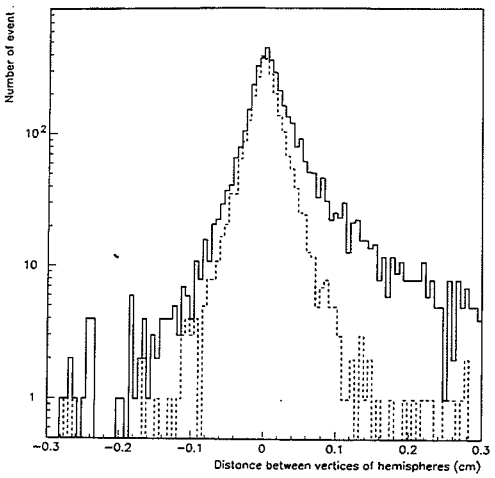

Fig. 30. The longitudinal distance between two vertices constructed in the two hemispheres of the events. The full-line is for vertices with a χ^2 probability less than 10%, the dashed-line for the other events.

the vertex by more than five standard deviations to reject obvious outliers. Fig. 30 shows the longitudinal distance between the vertices along the thrust axis for events where the combined χ^2 probability of the two

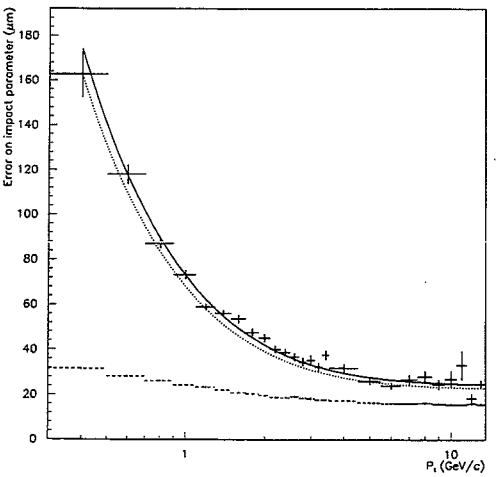

Fig. 31. The error on the impact parameter as measured as a function of p_t in real data. The dashed data gives the contribution from the error on the vertex, which has been subtracted quadratically from the error per track. The full line is a fit to $\sqrt{69^2/p_t^2+24^2}$ μm (p_t in GeV/c). The expected error transverse to tracks at the beamspot is represented with a dotted line.

vertices is smaller (full-line) and larger (dashed-line) than 10%. A clear asymmetric distribution is observed for the bad probability case, while for the complementary sample the distribution is symmetric, hence the life-time contribution to the impact parameter in this sample is suppressed. The events with the good probability are selected, and the impact parameter of each track in the event is plotted versus the vertex constructed from the remaining tracks, only accepting tracks in the vertex which lie within two standard deviations. Fig. 31 shows the measured error on the impact parameter as a function of p_t (full-line), with the contribution from the vertex taken out quadratically. This vertex contribution is calculated using the expected error per track for the tracks in the vertex, and is quite small as is shown by the dashed line in fig. 31. Parametrizing the error in the same way as for the expected distribution yields $\sqrt{69^2/p_t^2+24^2}$ μm (p_t in GeV/c). The dotted line gives the expected distribution as described above. This result is in agreement with the measurements from μμ and 3-prong tau decays. No systematics is observed for the ϕ and θ dependence of the impact parameter error.

9. Summary

The DELPHI Microvertex detector has been operated successfully since the beginning of the 1990 LEP running period. The two layered detector used in 1990 was upgraded with a third layer and a smaller beampipe in 1991. The same detector is currently used for the 1992 run. For the 1993 run, two of the layers will be replaced by double-sided silicon detectors.

The Microvertex detector uses 0.42 m^2 of silicon microstrip detectors with a diode pitch of 25 μm and a readout pitch of 50 μm. A characteristic feature of these detectors is the use of integrated coupling capacitors and polysilicon biasing resistors. With the requirements of a total leakage current less than 10 μA, biasing resistors with a resistance higher than 1 MΩ, a coupling capacitance greater than 7 pF/cm, and the number of defective strips less than 1%, the detector yield was 57% for the Inner and the Outer layer detectors and 75% for the Closer layer detectors.

The three layers of silicon detectors (average radii 6.3, 9.0 and 11.0 cm) cover polar angles from 43° to 137°. In this range the total amount of material traversed by a track is on average 1.5% of a radiation length. Each layer covers the full 2π of azimuthal angle, with a 10–15% overlap between neighbouring sectors. During the run, a few detector modules developed problems, but 93% (100%) of azimuthal angle remained covered by at least two (one) layers. For the remaining detector modules, the hit efficiency was 98%.

Charge sensitive amplifiers on the MX3 readout chips give a signal to noise ratio of 15:1 for minimum ionizing particles. The 73 728 readout channels are multiplexed on 72 analog differential lines, which are digitized in SIROCCO Fastbus units. These units use digital signal processors for zero suppression, which results in an average event size of 1.3 kbyte. For hadronic Z^0 decays, the average size is 4 kbyte.

Good mechanical stability is achieved by mounting the detector modules on aluminium end-rings and using water cooling to remove the 70 W generated by the readout electronics. The stability is monitored during runs by a system of light spots and a system of capacitive probes. The contribution to the precision from mechanical instabilities is estimated to be less than 3 μm from the analysis of tracks going through the overlaps between neighbouring sectors.

A survey of the Microvertex detector before installation determines the positions of all strips with a precision of 20 μm. Further alignment using tracks reduces this uncertainty to a level that is negligible compared to the precision of the clusters. This precision is a function of many variables, e.g. the track incidence angle and the cluster size, but is around 8 μm averaged over all 1991 data with 95% of clusters included.

The impact parameter uncertainty has been determined from hadronic Z^0 decays, and is well described by $\sqrt{(69/p_t)^2 + 24^2}$ μm, with p_t in GeV/c. This agrees with the value of 21 μm obtained for 45 GeV/c muons from $Z^0 \to \mu^+\mu^-$ decays.

The high precision of the Microvertex detector has been a key ingredient in the analysis of the more than 400 000 Z^0 events collected in 1990 and 1991. It has been crucial for the analyses of the tau lepton and the beauty and charm hadrons. Adding a third layer greatly improved our understanding of the detector alignment and the association of clusters with tracks. The resulting reduction of systematic uncertainties leads to a better spatial precision and shows the advantage of three layers over two.

The operation of the Microvertex detector has been straight forward. The detector stays on essentially for the whole year during all phases of LEP operation. The design makes it relatively insensitive to the machine background, and no damage of any kind has been observed.

Acknowledgements

The detector could only be constructed thanks to the dedicated effort of many technical collaborators in all laboratories participating in the project. We wish to express our appreciation to all of them, and in particular to M. Burns.

References

[1] P. Aarnio et al., DELPHI Collaboration, Nucl. Instr. and Meth. A303 (1991) 233.
[2] P. Abreu et al., DELPHI Collaboration, Phys. Lett. B267 (1991) 422.
[3] P. Abreu et al., DELPHI Collaboration, Z. Phys. C53 (1992) 567.
[4] P. Abreu et al., DELPHI Collaboration, Phys. Lett. B289 (1992) 199.
[5] P. Abreu et al., DELPHI Collaboration, CERN-PPE/92-174
[6] H. Dijkstra et al., Nucl. Instr. and Meth. A277 (1989) 160.
[7] M. Caccia et al., Nucl. Instr. and Meth. A260 (1987) 124.
[8] J.C. Stanton, IEEE Trans. Nucl. Sci. NS-36 (1989) 522.
[9] P. Astier, J.F. Genat and J. Pelletier, LPNHE Internal Report 92-120.
[10] G. Barichello and M. Pegoraro, DELPHI 90-19 TRACK 63, 12 June 1990.
[11] A. Andreazza, P. Biffi, C.Meroni and A. Stocchi, Nucl. Instr. and Meth. A312 (1992) 431; and
A. Andreazza, Thesis, Milano 1991.
[12] N. Bingefors and M. Burns, DELPHI 88-48 TRACK 48, 8 July 1988.
[13] DSP56000/DSP56001 Digital Signal Processor User's Manual, Motorola Inc., 1990.
[14] M. Battaglia et al., Nucl. Phys. B (Proc. Suppl.) 23A (1991) 448; and
M. Caccia et al., Nucl. Instr. and Meth. A315 (1992) 143.
[15] R. McNulty, DELPHI 92-40 TRACK 69, 27 March 1992.

Publication 5.

Nuclear Instruments and Methods in Physics Research A 339 (1994) 564–569
North-Holland

NUCLEAR
INSTRUMENTS
& METHODS
IN PHYSICS
RESEARCH
Section A

Design and performance of an analog delay and buffer chip for use with silicon strip detectors at LHC

The RD20 collaboration

R. Brenner [a], H. von der Lippe [b,1], J. Michel [c], E. Nygård [d,2], T. Ødegaard [d], N.A. Smith [e], P. Weilhammer *,[a], K. Yoshioka [a]

[a] *CERN, Geneva, Switzerland*
[b] *Senter for Industriforskning, Oslo, Norway*
[c] *LEPSI, Strasbourg, France*
[d] *Senter for Industriforskning, Oslo, Norway*
[e] *Liverpool University, Liverpool, UK*

(Received 12 August 1993)

An analog delay and buffer chip has been designed and built in 1.2 μm CMOS technology to be used in silicon detectors at LHC. Measurements on the performance of the prototype chip are presented. The storage cells variations are smaller than 0.65 rms mV, i.e. 1/100 of the signal in its input for a minimum ionizing particle.

1. Introduction

Silicon microstrip detectors have a number of features to make them promising candidates for use in proposed experiments at the future Large Hadron Colliders. They are fast, with signal collection speeds in the range 20 to 30 ns, relatively radiation hard and can be built with very high granularity well matched to the high particle density expected in TeV hadron collisions.

The requirements on the associated front-end electronics to read out minimum ionising particle signals from interactions at LHC are very demanding. The following parameters have been used as preliminary guidelines for the data handling capability required by the front-end electronics:

interval between each beam crossing:	15 ns;
first level trigger delay;	1 μs;
first level trigger frequency:	100 kHz;
second level trigger delay:	20–100 ms;
second level trigger frequency:	1 kHz.

Several approaches have been followed to implement front-end electronics which can fulfil all the requirements of future experiments at LHC and SSC, in particular for tracking devices very near the interaction region [1]. Within the RD20 collaboration [2] a novel front-end concept has been proposed [3]. In this approach, the emphasis is put on a full analog low noise and low power readout implemented throughout in CMOS.

A fast preamplifier circuit is combined with a moderately fast shaper circuit in order to achieve full charge collection with optimal noise performance and acceptable power consumption. That input stage is followed by an analog delay and buffer unit to preserve the information of a particular event until the arrival of a first level trigger signal.

Allowing a shaping time of signals long compared to the bunch crossing time requires a mean to retrieve exact timing information. This is achieved by deconvoluting the sampled pulse shape with a relatively simple analogue deconvoluting circuit (APSP) [4], which reconstructs the original time interval in which the charge pulse occupied at the detector.

In this paper a description of the design and the performance of the Analog Delay Buffer chip used in this architecture is presented.

[1] Now at Lawrence Berkeley Laboratory, Berkeley, CA, USA.
[2] Now at Oslo University, Oslo, Norway.
* Corresponding author.

SSDI 0168-9002(93)E0864-O

2. The RD20 front-end electronics concept

The basic design concept proposed by RD20 for the front-end electronics for a silicon tracker at the LHC is outlined in Fig. 1. The signal from the detector is amplified with a charge sensitive preamplifier followed by a CR–RC shaper with a peaking time of 45 ns. The shaped signal is continuously sampled in the Analog Delay and Buffer (ADB) with a sampling frequency of 67.7 MHz. Inside the ADB, the samples are delayed by 1 μs, which is the assumed time for the Level 1 Trigger decision to be taken. Whenever a positive Level 1 Trigger decision arrives, 4 samples associated with that trigger are tagged and protected from overwriting until they are transferred to the Analog Pulse Shape Processor (APSP). Storage cells containing samples having a delay of more than 1 μs and not having a tag are overwritten with new information.

In the APSP, a deconvolution filtering operation takes place by utilising 3 of the transferred samples to restore the original signal from the strip detector (the 4th sample is presently not being used). The deconvolution principle has been described in ref. [5].

The modules of the proposed system shown in Fig. 1, i.e. the amplifier and shaper, the ADB and the APSP have all been designed, produced and tested in prototype form. Presently they are physically located on three separate chips, but their integration into one single chip is under way. The object of this paper is to present the functionality of the ADB and the results from the evaluation of it.

3. The analog delay and buffer

The ADB consists of an analog section and one digital control-logic section. The analogue part consists of 4 identical, parallel channels each featuring an input amplifier followed by 84 storage cells and thereafter an output amplifier. In Fig. 2, these basic elements are outlined.

The control-logic controls the flow of data in the analogue section by, for instance, providing the sampling clock of the input signal, controlling the delay of the samples, the buffering of triggered samples prior to the APSP, and the delivery of the samples to the APSP at the right time. The control-logic is subdivided into a Control Unit and Registers which contains pointers; the main Registers are illustrated in Fig. 3.

The input signal is continuously sampled every 15 ns. Each sample is stored in the analogue cell which at a given moment is addressed by the write pointer. Once the write pointer reaches the last available position of the storage cell's array, it jumps back again to the first available position. The trigger 1 pointer is running behind the write pointer spaced by 1 μs which is the anticipated delay of the T1.

Whenever a positive T1 decision arrives, 4 cells associated with this event are turned into a temporary 4 cell buffer-zone which is protected from being overwritten until it has been read out and hence released. Three out of the 4 cells contain the necessary information for performing the deconvolution and the fourth cell holds the analogue value of the peak of the shaped pulse. Each of the individual cells in a buffer-zone are marked in the trigger-tag register, which stores every buffered cell regardless which buffer-zone it belongs to, and in one of the event registers, which stores only the group of 4 cells belonging to one buffer-zone. The cell which contains the first sample in a buffer-zone is marked in the first sample register.

The readout of the events (buffer-zones) is sequential, i.e. first event in becomes the first event out. This is organised in such a way that whenever a new read-

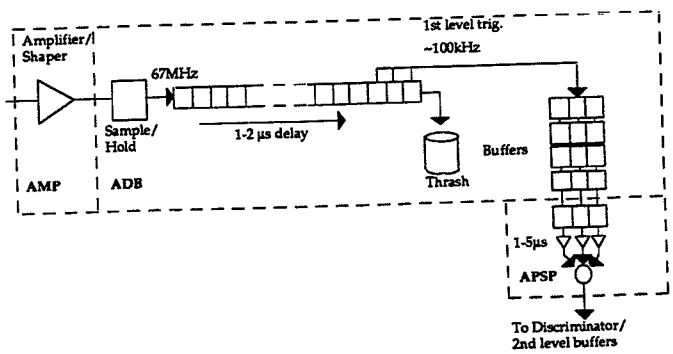

Fig. 1. RD20 Front-End Electronics. The Analog Delay and Buffer (ADB) is continuously sampling the output of the amplifier. When a positive Level 1 Trigger arrives, 4 samples are tagged. Eventually, the tagged samples are processed by the APSP.

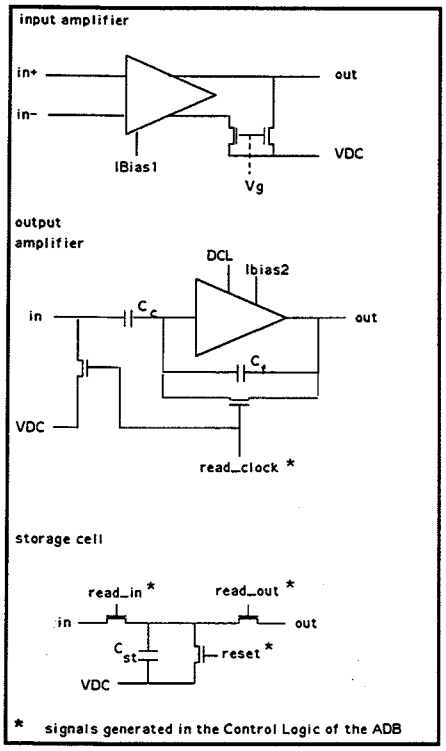

Fig. 2. Analog chain of the ADB. The input and output amplifiers are present only in the prototype chip to permit the stand-alone tests.

out cycle starts, the event register which contains the buffer-zone which now is the oldest will be found and selected. In order to find the first cell in the buffer-zone to be read out, the Control Unit looks in the first-sample register. In this register there will be one and only one tag which has a corresponding position to one of the 4 tags in this event register. The cell which corresponds to this coincidence will then be read out first and the other 3 will follow in sequence. After the readout, the buffer-zone will be released by removing the tags in the trigger-tag register.

The writing of new samples is unaffected by the readout and hence the circuit is able to write into a new cell every 15 ns. This means that the write pointer will frequently pass by cells which it cannot write into because the cell has turned into a buffer-zone cell which has not yet been read out. Whenever this situation occurs, a mechanism is implemented which will force the write pointer to skip all cells of this kind and jump until it finds a free cell. This mechanism is called "bypass". It utilises the trigger-tag register for this purpose, which as already described contains all the cells which are tagged. The "bypass" mechanism is illustrated in Fig. 4.

In the present design there is an upper limit of 4 dynamically located T1 buffer-zones in the ADB which can be used simultaneously (each buffer-zone represented by 4 samples). Since the readout of the ADB runs at approximately 4 μs/buffer-zone (the readout speed is determined by the processing time needed by the APSP) and a new buffer is released after each readout, the probability of an overflow is small [6] since the average Level 1 trigger rate is only 100 kHz.

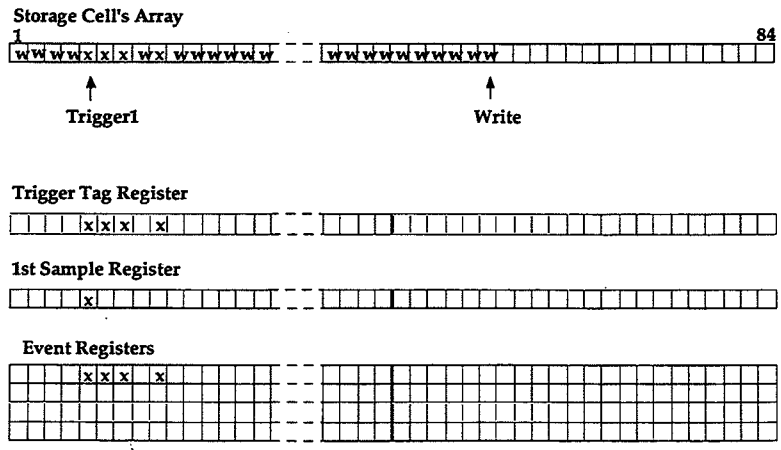

Fig. 3. Main registers and pointers. The Trigger 1 pointer is running behind the Write pointer by 1 μs. Whenever the Level 1 Trigger arrives, the storage cells pointed by the Trigger 1 are tagged in the Trigger Tag register creating one buffer-zone, and the first sample of that event are tagged in the 1st Sample register.

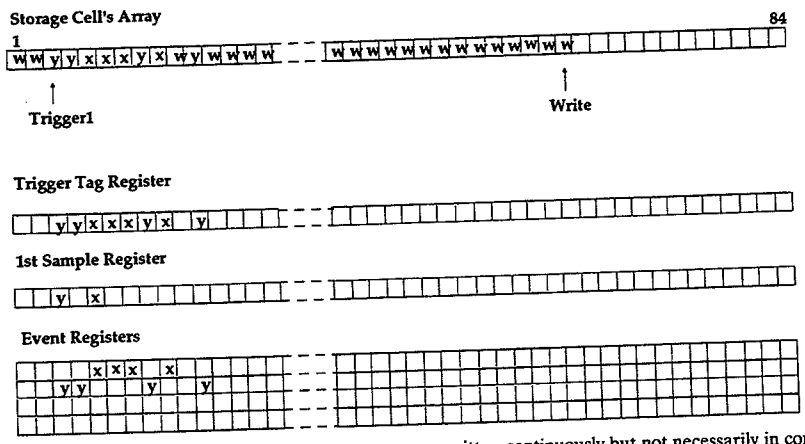

Fig. 4. Bypass mechanism. The samples from the amplifier output are written continuously but not necessarily in contiguous storage cells.

The ADB prototype circuit has been implemented in a 1.2 μm CMOS technology with a total power consumption of approximately 50 mW, which for a 128 channel full version chip would scale to approximately 0.4 mW/channel since the present 4 analogue channels can be extended to 128 without any other changes. The input amplifier and the output amplifier shown in Fig. 2 are not foreseen in a final integrated version of the system. They are incorporated in this prototype only in order to permit the stand-alone tests.

4. Measurements

4.1. Set-up

For bench test purpose, the electronic environment in which the ADB will operate at LHC was emulated by signals from pulse generators: BCO clock, READ clock, Level 1 Trigger (T1), IDLE. Fig. 5 shows the measurement set-up.

The Level 1 Trigger is used to tag samples read into the ADB 1 μs before. The T1-tagged samples are retrieved serially on the falling edge of the IDLE signal. The readout speed is determined by the READ clock, which in these tests ran at 1 MHz.

4.2. Signal transmission

In order to show that the ADB's delay function is correct, one period of a sine wave was put into the ADB and was retrieved delayed by 1 μs. Each sample can be retrieved in any of the four periods per event readout cycle. Then, one of those periods can be used to scan the delayed signal by keeping the sine wave fixed in relation to the reset (to make sure that the samples from the signal are stored in the same storage cells) and moving the T1 to get the samples on the desired period. Fig. 6 shows the signal applied to the input of the ADB and the corresponding signal on the 2nd, 3rd and 4th periods of the output.

The amplitude of the output voltage of the shaper corresponded to the charge created by 0.5 minimum ionizing particle at the input.

4.3. Storage cell variations

To verify the magnitude of the variation amongst storage cells due to the processing of the chip or due to pick ups from switching circuitry, three different DC levels were applied to the input of the ADB and, for each dc level, the output signal from all the 84 storage

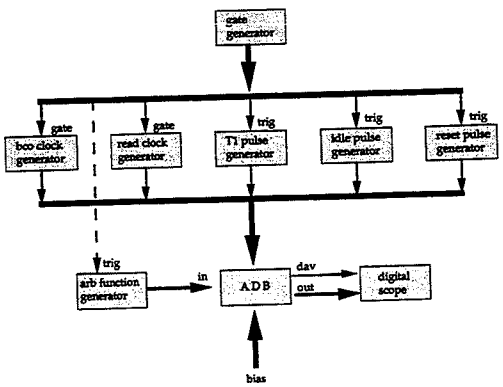

Fig. 5. Schematic of the set-up for testing the ADB.

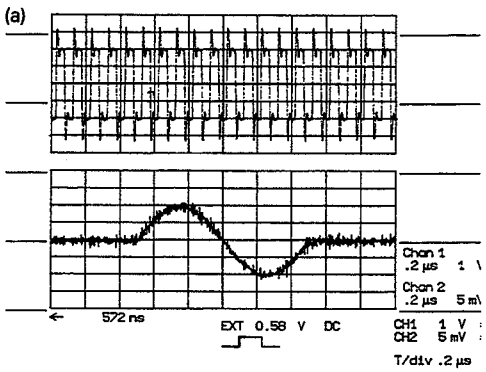

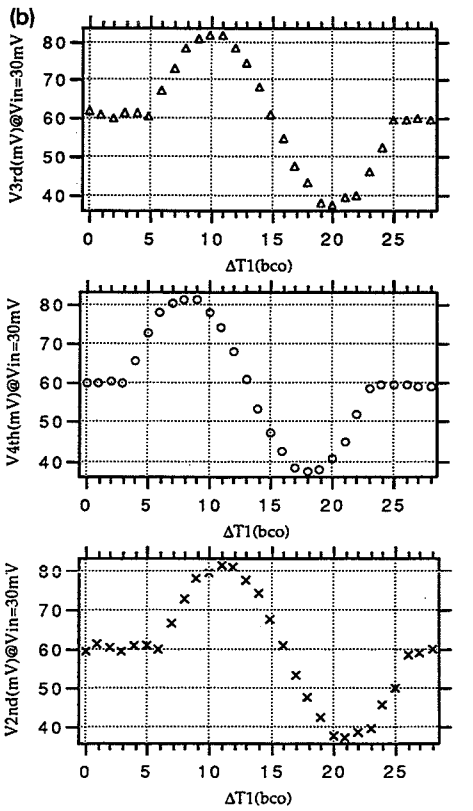

Fig. 6. Signal transmission: (a) Input. The amplitude of the sine wave corresponds to the peak value of the output of the amplifier for a 0.5 minimum ionizing particle. The sinus wave is continuously sampled by the BCO clock. (b) Output. The sampled values of the sinus wave are delayed and shifted out of the ADB by moving the Trigger Level 1 (T1).

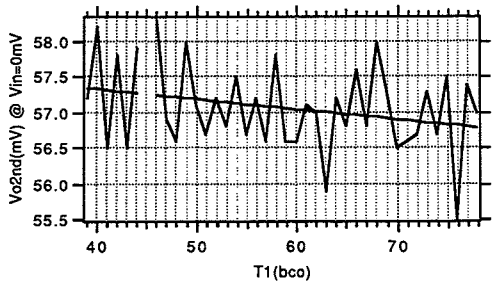

Fig. 7. Storage cell variation.

cells measured. The reason for this approach is that the signal is written onto the capacitor as a voltage but it is the corresponding charge which is read out again (although transformed into voltage once more before sent out from the chip). Hence, if there were variations in the capacitor values, the variations on the output depend on the input dc voltage level.

An example of those measurements is shown in Fig. 7, and it shows in addition to variations between cells that there is a small dc level shift between the 1st and the last cell. The variation of the dc output level along the storage cells is 0.75 mV but it is independent of the dc input level. A linear fit was done to the curve in Fig. 7 and the rms variations of the residues are listed in Table 1.

The results show that the non-uniformity among storage cells is not correlated with the input level and variations from cell to cell are in all cases smaller than 3 mV with rms values smaller than 0.65 mV. This indicates that the variations are not due to a spread in the capacitance of individual cells but probably caused by variations of charge injection from switches along the storage cell's array.

4.4. Bypass test

In order to test the bypass control circuitry, a sine wave and a triangular wave were fed into the ADB as shown in Fig. 8. The set-up was made such that the externally applied T1 pulses for the two different waveforms were displaced by 82 BCO clock-periods. In this way, the buffer-zone created due to the first T1 will force the buffer-zone created due to the second T1 to

Table 1
Measured storage cell voltage variations for 3 input dc voltage levels. The rms values are given for residuals w.r.t. a linear fit

V_{in} (mV)	σ (mV)
0.0	0.61
10.0	0.63
20.0	0.49

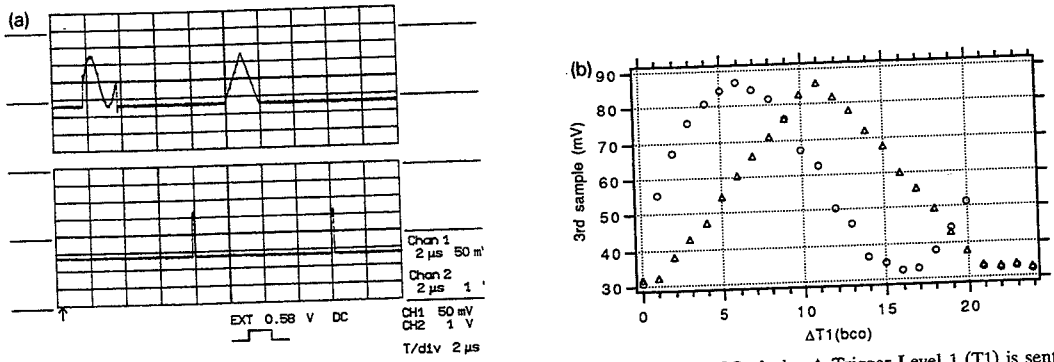

Fig. 8. Bypass: (a) Input. The sinus wave and the triangular wave are spaced by 82 BCO clocks. A Trigger Level 1 (T1) is sent creating a buffer-zone with samples from the sinus wave. Another Trigger Level 1 is sent creating another buffer-zone with samples from the triangular wave. The spacing of these waves ensures that the samples from the triangular wave are not written in contiguous storage cells. (b) Output. The 3rd sample from the 1st T1 and the 3rd sample from the 2nd T1 are in the same picture, showing that the bypass circuitry is working correctly.

be split in two halves, the first two cells in front of first buffer-zone and the last two following behind (overall buffer length is 84 cells).

Reading out these two events (8 cells in total), the sine and the triangular waves can be reconstructed by repeating the procedure used in section 4.2, now using the 1st and 5th readout periods (as well 2nd and 6th, 3rd and 7th or 4th and 8th periods) for scanning the delayed signals. This is shown in Fig. 8. It shows that the cell-skipping mechanism works correctly.

5. Conclusions

From the tests of the Analog Delay and Buffer circuit described in this paper, one can conclude that the basic functionality of the device is correct. Signals are transmitted with small distortion in comparison with the overall noise in the system, and the variations between storage cells are less than 1 mV rms, which is well below the foreseen noise performance of the circuit.

Acknowledgements

This work has been funded by CERN and several national agencies: IN2P3 (France), NAVF (Norway), SERC (UK). We should like to thank them all for their support.

References

[1] SDC Silicon Tracker Conceptual Design Report (1992).
[2] H. Borner et al., CERN/DRDC 91-10 (1991).
[3] RD20 Status Report, CERN/DRDC 92-28 (1992).
[4] N. Bingefors et al., Nucl. Instr. and Meth. A 326 (1993) 112.
[5] S. Gadomski et al., Nucl. Instr. and Meth. A 320 (1992) 217.
[6] G. Hall, RD20/TN/12 (1993).

Publication 6.

Nuclear Instruments and Methods in Physics Research A 339 (1994) 477–484
North-Holland

NUCLEAR INSTRUMENTS & METHODS IN PHYSICS RESEARCH Section A

Performance of a LHC front-end running at 67 MHz

RD20 Collaboration

R. Brenner [a], J. Kaplon [b], H. von der Lippe [c,1], E. Nygård [c,2], S. Roe [a], P. Weilhammer [a,*], K. Yoshioka [a]

[a] *CERN, Geneva, Switzerland*
[b] *Institute of Nuclear Physics, Cracow, Poland*
[c] *Senter for Industriforskning, Oslo, Norway*

(Received 12 August 1993)

The prototype version of a novel front-end system, designed for the readout of silicon microstrip detectors at the LHC, has been tested using 100 GeV pions incident on a microstrip detector in the X5 beam line at CERN. The prototype consisted of preamplifier and shaping amplifier with 45 ns time constant, an 84 cell analogue pipeline and analogue pulse shape processor, with the individual elements of the system implemented as separate electronics chips. The timing conditions in the test were set up to simulate those in hadron collider experiments and a clock speed of 67 MHz was used. Deconvolution of particle signals from a silicon detector was successfully demonstrated for the first time in LHC-like experimental conditions.

1. Introduction

The RD20 collaboration has proposed a novel front-end electronic architecture for reading out silicon detectors in a LHC experiment. A low power consumption with good signal to noise ratio will be obtained with a slow shaping preamplifier. The time resolution needed will later be extracted by deconvolution of the slow pulse. A prototype front-end chain in separate elements was tested in a 100 GeV pion beam at the X5 beam line at CERN. The purpose of this beam test was principally to demonstrate the operation for the first time of this signal processing scheme under semi-realistic conditions but some studies of pulse height observations in the test were also possible. The data obtained in the testbeam were also used later as a reference for minimum ionizing particles for tests in laboratory environment.

The elements of the electronic system were a preamplifier and shaping amplifier [1], an analogue delay and buffer (ADB) [2] and an analogue pulse shape processor (APSP) [3]. The electronics was connected to a p^+-implanted ac-coupled detector [4] which had been irradiated with electrons to a dose of 50 kGy (5 Mrad). The strip length was 4 cm and the strip pitch 50 μm. The width of the p^+-implant was 10 μm. The prototype front-end chips were four channels wide but data was stored from only two of them because of the limited number of ADC channels available.

2. The RD20 front-end architecture

The principle of the RD20 front-end system can be found elsewhere [3]. The basic concept is to obtain low noise at low power consumption by using a 45 ns CR–RC shaping of the preamplifier pulse. With the assumption that the time between beam crossings at the LHC will be 15 ns, the 45 ns shaped pulse does not unequivocally identify the interval in which a track measured in a detector originated. The time and charge information of the signal have therefore to be recovered by a deconvolution algorithm implemented as purpose-built integrated circuit, the APSP. The shaped pulse cannot be continuously deconvoluted because the very high speed needed would consume excessive power. The preamplifier signal is instead delayed by 1–3 μs, which is the estimated time between first level triggers at LHC, in a pipeline buffer, the ADB, before entering the APSP. In the present prototype version of the pipeline a 1 μs delay is implemented. The length of

[1] Now at Lawrence Berkeley Laboratory, Berkeley CA, USA.
[2] Now at Oslo University, Oslo, Norway.
* Corresponding author.

SSDI 0168-9002(93)E0865-P

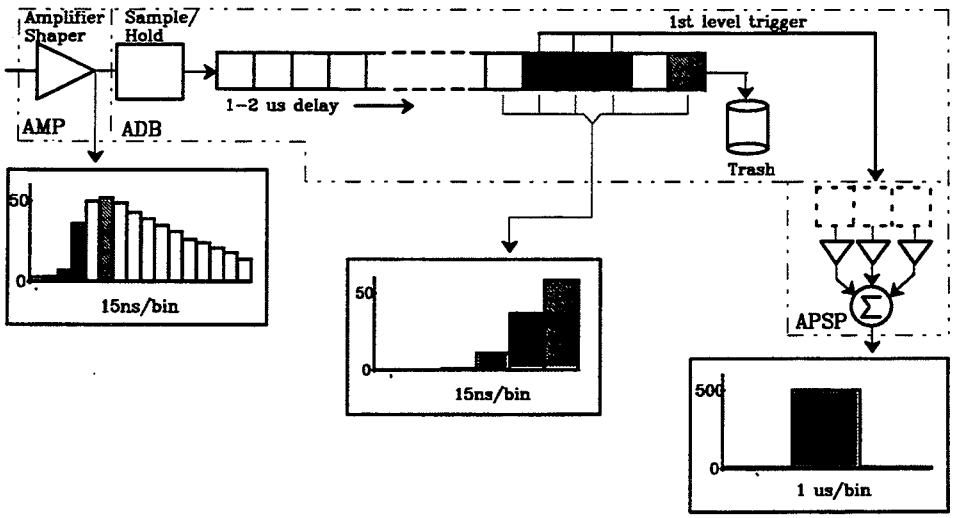

Fig. 1. A schematic of the front-end electronic system proposed for LHC. The amplifier is followed by an analogue pipeline which delays the signal. At a positive first level trigger decision the data is serially transferred into an analogue processor to resolve the time information. Below the schematics a pulse is followed through the system. The cross-hatched bins are the samples used for the deconvolution. The single-hatched bin is the peak value used for the pulse height measurements.

the delay is the estimated time for obtaining the first level trigger decision, T1, in a LHC experiment. If the first level trigger comes, four delayed samples associated with the event indicated by first level trigger are marked and later transferred to the APSP. If there is no trigger the samples are overwritten after 1 μs. The amount of data reaching the APSP is now reduced by a factor of about 1000 assuming an average trigger rate

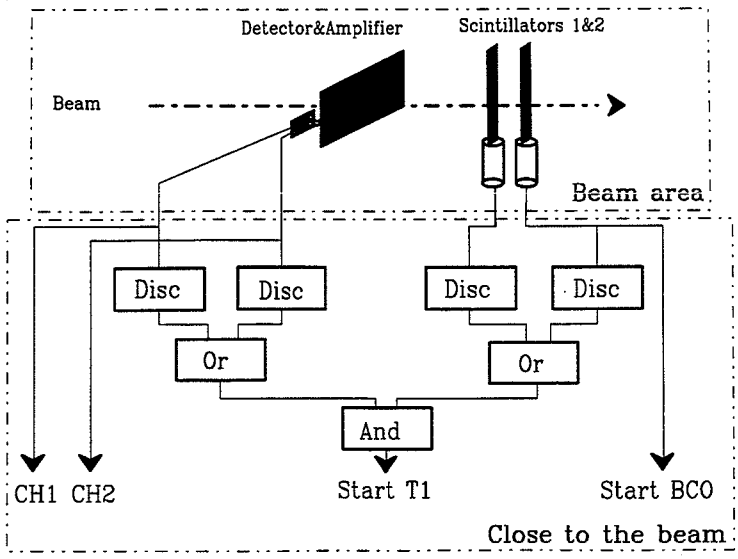

Fig. 2. The testbeam setup with hodoscope and triggering logic.

of 100 kHz. A schematic of the circuit is shown in Fig. 1.

3. Testbeam

3.1. The setup

Pulse generators and hodoscopes were used to emulate the LHC timing conditions in which the proposed tracking system could be embedded. The setup was divided into two parts shown in Figs. 2 and 3. One part, placed at the beam, consisted of a detector connected to the preamplifier shaper, scintillators and electronics to form coincidences between discriminated signals from the preamplifier shaper and hodoscopes. The second part, placed outside the beam area, consisted of the ADB- and APSP circuits with pulse generators for external clocking and digital oscilloscopes connected via GPIB interfaces to a personal computer.

The setup was run with a pulsed BCO clock generator instead of a continuous running BCO clock. The second option would have been preferable but in the short time available for this beam test the pulsed BCO clock was easier to tune to the right timing. By using the pulsed BCO clock the data collected was always stored in the same cells in the ADB. On the other hand it has been shown [5] that the effect of variations between the storage cells in ADB is much less than 1 mV rms, which is negligible compared to the noise from the front-end amplifier.

A Start-T1 signal was recorded in any of the readout channels of the detector in coincidence with both scintillators. Because of the delay in starting the pulse generators the start-BCO signal had to be given as early as possible. This was done using the signal from one of the scintillators before any delaying logic. The signal from the preamplifier shaper was delayed by 400 ns with a thick BNC cable in order to have the rest of the chain ready for the data. When the BCO clock was started a RESET pulse was immediately generated to clear the circuits. The TRIGGER 1 pulse was delayed to match the analogue pulse arriving from the preamplifier shaper. Finally the Read Clock was started transferring data from the ADB to the APSP. The Read Clock in this test was chosen to run at 1 MHz asynchronously with the BCO clock.

The pulse shapes were sampled at three nodes of the system and stored for off-line analysis; after the preamplifier shaper, after the ADB and at the output of the APSP. The digitisation of oscilloscope reading the amplifier shaper signal was clocked externally by the BCO clock and the signals coming from the ADB and the APSP were externally clocked by the readout clock. The oscilloscopes were externally triggered by the Start-T1 signal.

3.2. Results

In the short duration of time of this testbeam about 3000 events were recorded. However, because of problems ensuring that the two digital oscilloscopes, using separate time bases, should trigger simultaneously for data acquisition, some of the data were lost. This had a small impact on the detailed analysis of the signal to noise in the system and did not prevent the demonstration of its functionality.

The histograms shown in Fig. 1 show the averaged pulse shape of all the data recorded in the testbeam. The three cross-hatched bins in the amplifier shaper data and in the ADB data are the bins transferred through the system to the APSP. The single-hatched bin is stored for accurate pulse height determination in low luminosity conditions when no pileup of events is

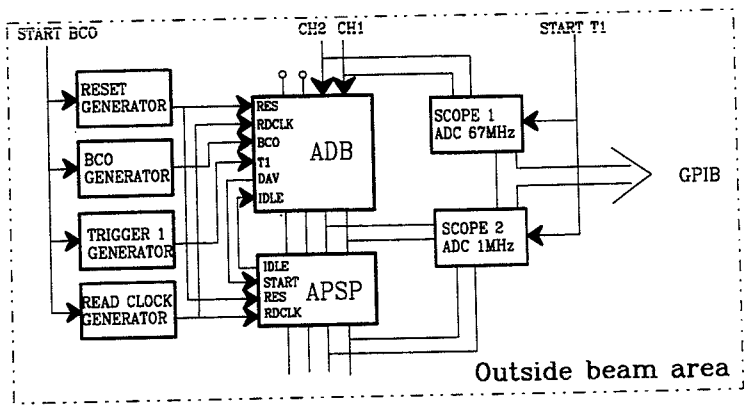

Fig. 3. The ADB and APSP clocking schematics.

likely. Fig. 4 shows the pulse heights in two neighbouring channels of a typical single event observed at different parts of the system showing clearly the observation of an in-time event which was successfully deconvoluted. The event is shown as seen after the amplifier shaper, ADB and the APSP. The pulse height after the APSP is higher than the pulse height of the pulse in the amplifier shaper and the ADB. This is due to the gain in the APSP being about ten times higher than the rest of the chain.

The pulse height information from the system was studied off-line in more detail to make a more quantitative assessment of the performance of the electronic chain. Since no absolute timing was recorded in the test, some assumptions had to be made to select events with the correct timing with respect to the BCO. To achieve this the samples at the output of the ADB were used. The selection of useful events made use of the known signal pulse shape by requiring the third sample given to the APSP to be between 50 and 85% of the maximum recorded pulse height. By this assumption about 50% of the noncorrupted data was used for the analysis. Because of a bad groundplane on the printed circuit board for the APSP the single channel data was spoiled by pickup from the beam. The effect of the pickup was correlated in the two readout channels. Some quantitative results could still be saved by subtracting the two APSP channels. In this case the total pulse height decreases because some charge information from the neighbouring strip is subtracted. Fig. 5 shows the pulse height of the channel with the bigger pulse when the pulse height from one

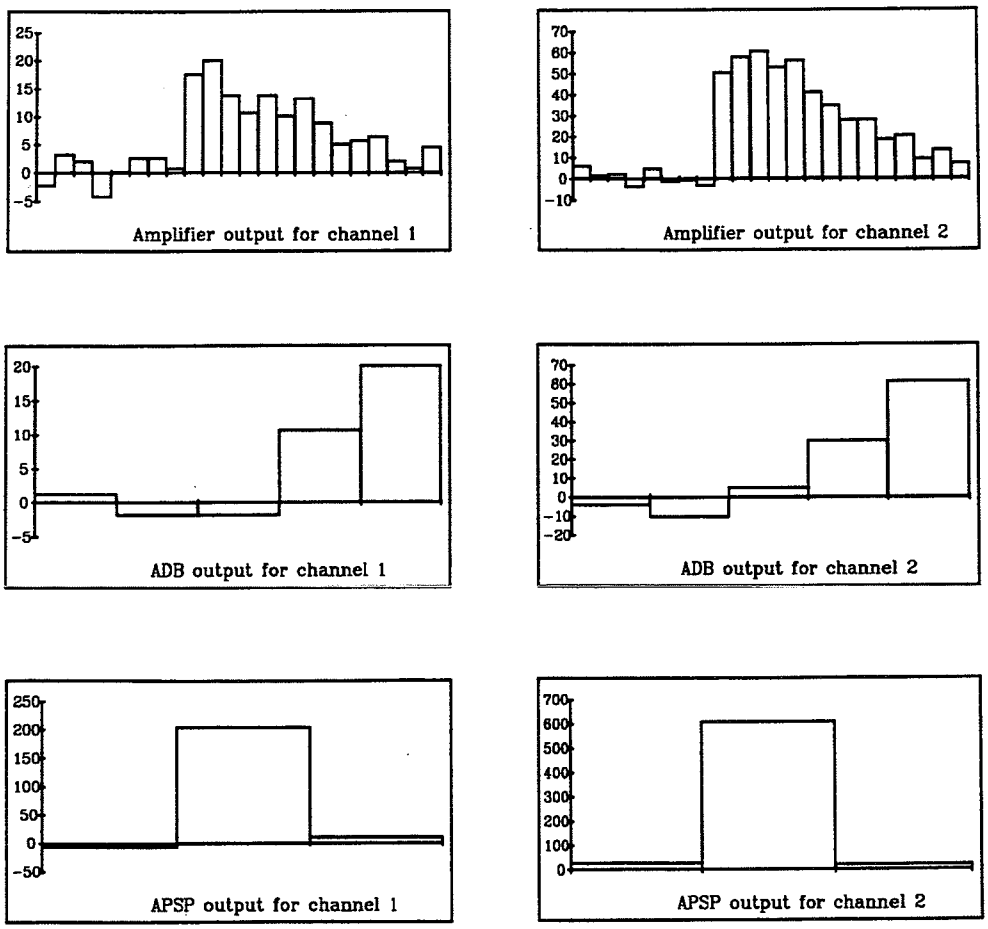

Fig. 4. A typical single event for two neighbouring channels seen after the amplifier, ADB and APSP. The vertical scale is given in mV.

neighbouring strip is subtracted for the amplifier shaper, the ADB and the APSP samples.

Finally the functionality of the APSP circuit in this testbeam can be demonstrated by comparing the calculated response from the APSP with the measured response. The pulse height of the APSP is calculated using the pulse height of the three samples given to the APSP. In the calculations the same deconvolution algorithm implemented in the APSP circuit is used. The correlation plot is shown in Fig. 6.

4. Laboratory tests

4.1. The laboratory setup

The setup in the testbeam was tested with a ^{104}Ru β-source in the laboratory. In order to obtain straight tracks the source was collimated. Two scintillators were used in this setup, one thin and one thick scintillator, in coincidence with the readout channels of the detector to generate a trigger. The noise for the preamplifier-shaper, the ADB and the APSP was measured without source triggered randomly. The setup was unchanged from the testbeam although the setup had been rebuilt in the laboratory and the gain settings of the ADB and the APSP were changed due to different biasing. The electron irradiated detector from the testbeam and a new nonirradiated detector were tested in the laboratory. The geometry of the two detectors were identical with total leakage current going to the backplane for the electron irradiated detector 1.2 μA and for the nonirradiated detector 1.8 μA at 100 V.

4.2. Laboratory results

The data obtained with source is comparable with the data from the testbeam, Fig. 7. More care had been put into setting up the timing of the system giving a narrower trigger window than in the testbeam. The data was analysed using the same cuts as the testbeam data, which with the improved timing condition re-

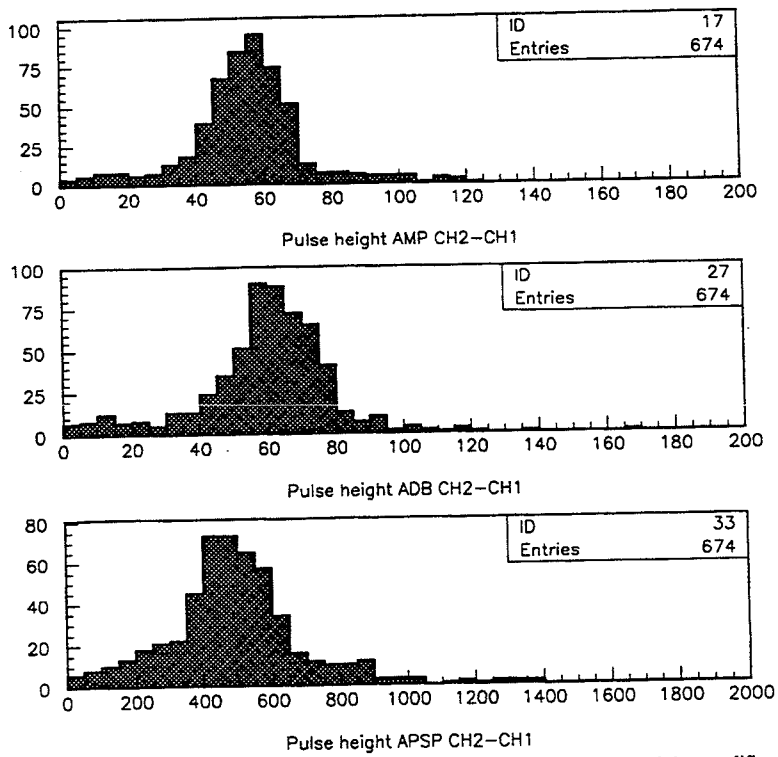

Fig. 5. Pulse heights for the difference of two neighbouring channels recorded from the output of the amplifier shaper, ADB and APSP.

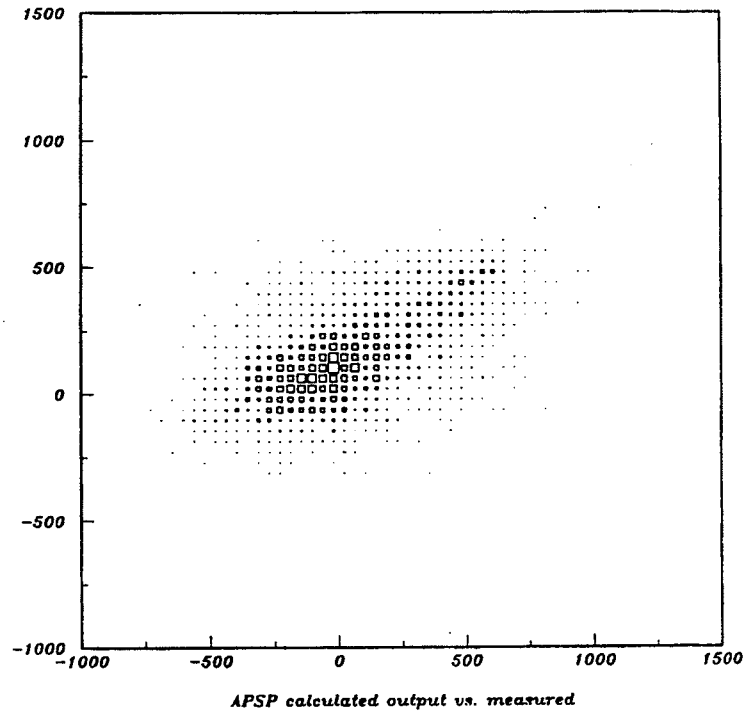

Fig. 6. The calculated pulse height plotted versus the measured one in the APSP circuit.

sulted to 80% of the recorded data being used for the analysis. The pickup in the APSP was reduced and a full study of four channels was made.

The pulse height distribution, for the sum of two strips, at the three nodes in the system for the nonirradiated detector can be compared in Fig. 8. Shown in the same figure is the expected response from the APSP calculated using the information in the ADB using the appropriate weights. The distributions are fitted with a Landau function describing the charge loss for minimum ionizing particles transversing the detector. The noise throughout the chain is presented in Fig. 9. The noise presented for the measured APSP noise is not common mode corrected. The correction is 54 mV rms.

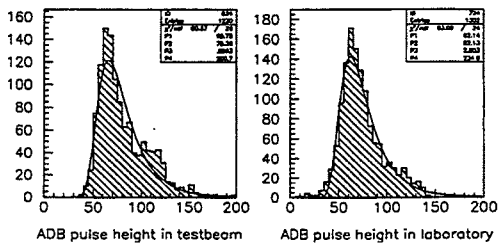

Fig. 7. Pulse height distribution from the ADB in the testbeam (left) and the laboratory (right).

The performance in signal to noise in the system for the two detectors measured are shown in Tables 1 and 2. In this test 20% of the charge was lost by the deconvolution. This is some more than expected but the level is acceptable considering the generous acceptance in timing and perhaps the not optimal pulse shape. The noise in the ADB compared with the preamplifier shaper is within errors the same 22/1. A noise increase in the APSP was calculated to 30% which degraded the S/N in the APSP to about 12/1.

Finally the response from the APSP was studied by scanning the 45 ns RC–CR shaped signal. This study is important when trying to estimate the performance of a discriminator connected to the APSP. By moving the T1 in steps of 15 ns around the right time bin the response from the APSP was studied. In an ideal case the pulse height in bins outside the right one should be zero. On real data some contamination is expected because of the charge signal not being a clean delta pulse [6]. The APSP response was recorded at −15, 15 and 30 ns delay compared with the right time bin. The

Table 1
The performance of the front-end connected to a nonirradiated detector

Nonirradiated	Signal	Noise	S/N
Amplifier shaper	53	2.4	22
ADB	58	2.6	22
APSP	472	38	12
APSP calculated	47	31	15

Table 2
The performance of the front-end connected to an electron irradiated detector

Electron irradiated	Signal	Noise	S/N
ADB	62	3.0	21
APSP	498	45	11

data was analysed using the same cuts as described but shifting the data with the corresponding delay to the T1 trigger. The result obtained in this exercise is shown in Fig. 10. The source for the contamination of the signal in the neighbouring bins is mainly due to timing shifts and non optimal pulse shapes.

5. Conclusions

The functionality of a front-end design using a 45 ns preamplifier-shaper circuit, an analogue delay buffer and with a deconvolution filter has been tested in a 100 GeV pion beam. Except for some problems with gain mismatch and pickup the functionality has been proven to work as designed. Further detailed studies were performed in the laboratory. The conditions in the laboratory were comparable with the testbeam. The final response from the deconvolution in the APSP was

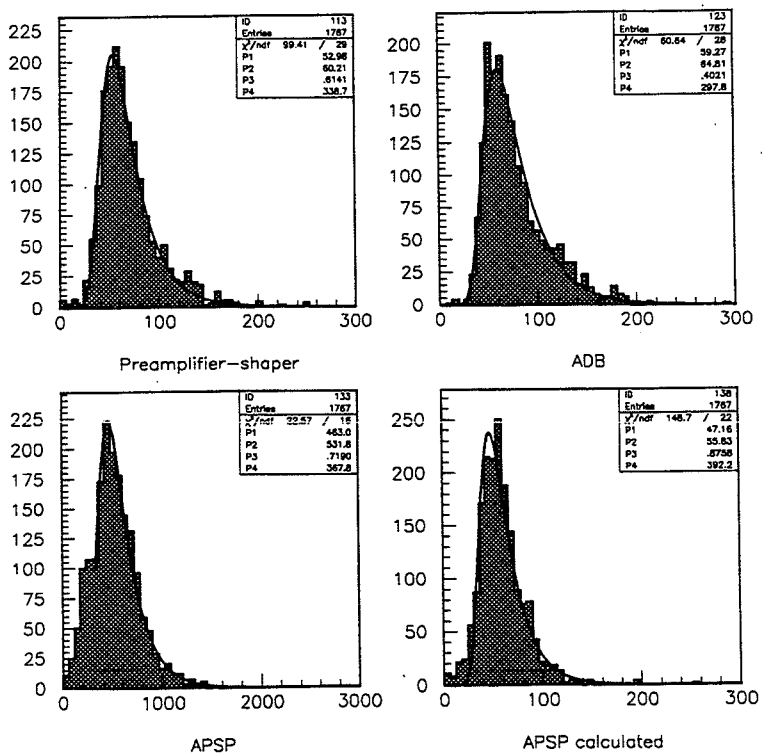

Fig. 8. The pulse heights for the sum of two channels for the three nodes in the chain. The fourth distribution is the expected response for the APSP. The pulse height distributions are fitted with a Landau function. The most probable peak given by P1 in the fit.

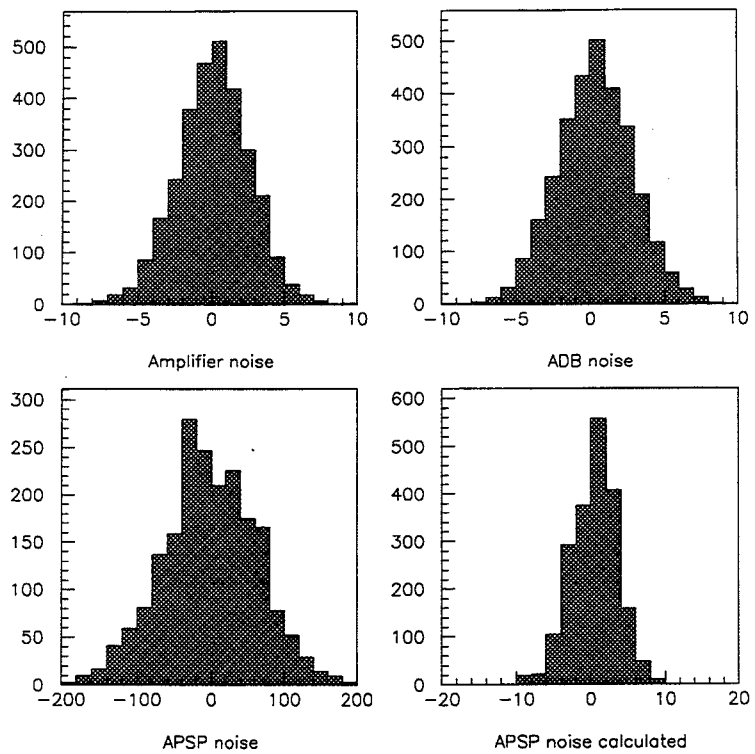

Fig. 9. The noise distribution for the amplifier shaper, the ADB and the APSP. The measured APSP noise has to be corrected for common mode.

both calculated and measured giving a signal to noise ratio before the deconvolution 22/1 and after the deconvolution 12/1 for two channel clusters to a single channel noise. A scan of the APSP was performed giving the contamination of the signal into the neighbouring time bin to less than 20%.

The results in this paper are obtained with the first prototypes of the front-end chain. The performance will improve when the full chain will be integrated to a full chip with each part matched to the other.

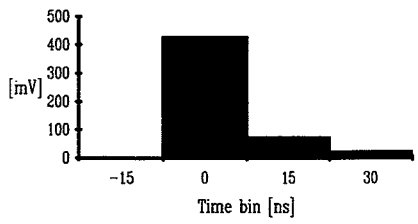

Fig. 10. The APSP response for the T1 trigger delayed by −15, 0, 15 and 30 ns.

Acknowledgements

This work has been funded by CERN and several national agencies: NAVF (Norway), KBN, the Polish State Committee for Scientific Research (Poland). We should like to thank them all for their support.

References

[1] T. Høgh et al., A low noise low power CMOS charge sensitive amplifier for silicon detectors at LHC, contribution to Poster Session, 6th Europ. Symp. on Semiconductor Detectors, Milan, 1992.
[2] R. Brenner et al., CERN-PPE/93-138.
[3] N. Bingefors et al., Nucl. Instr. and Meth. A 326 (1992) 112.
[4] R. Wheadon, RD20 P-Side Test Structures (IC/SI), CERN RD20/TN3.
[5] H. Borner et al., CERN R&D Proposal CERN/DRDC 91-10.
[6] W. Dabrowski and M. Idzik, Second-Order Effects in Front-End Electronics, CERN, RD20/TN/15 (1993).